國立交通大學

電子工程學系　電子研究所

博 士 論 文

n型反置層精準量子計算：
應變、次能帶、遷移率及三維結構

Sophisticated Quantum Computation on n-type Inversion Layers: Strain, Subband, Mobility, and 3-D Structure

研究生：　李韋漢

指導教授：　陳明哲 博士

中華民國 一０一年 十一 月

n 型反置層精準量子計算：
應變、次能帶、遷移率及三維結構

Sophisticated Quantum Computation on n-type Inversion Layers: Strain, Subband, Mobility, and 3-D Structure

研 究 生：李韋漢　　Wei-Han Lee

指導教授：陳明哲 博士　　Dr. Ming-Jer Chen

國立交通大學

電子工程學系　電子研究所

博士論文

A Dissertation

Submitted to Department of Electronics Engineering &

Institute of Electronics

College of Electrical and Computer Engineering

National Chiao Tung University

in Partial Fulfillment of the Requirements

for the Degree of

Doctor of Philosophy

in

Electronics Engineering

November 2012

Hsinchu, Taiwan, Republic of China

中華民國 一０一 年 十一 月

n型反置層精準量子計算：應變、次能帶、遷移率及三維結構

研究生：李韋漢　　　　指導教授：陳明哲 博士

國立交通大學

電子工程學系 電子研究所博士班

摘要

根據莫爾定律法則，我們正走向22/20奈米的科技世代，而且會不停地繼續開發更新更有效率的元件。然而在前進的路上會遇到許多問題，其中一個值得注意的問題是應力效應，它會影響到元件的一些電性和製程上的問題。這些物理特性我們可以從對漏電流和電子遷移率的實驗及模擬上觀察到。此外閘極穿隧電流跟次能階高度和位能障等能帶結構有強烈的相關性。所以閘極穿隧電流是個找次能階和應力效應的好工具。要建立一個正確的n型轉置層模擬計算，我們從對閘極穿隧電流的數據去做匹配的動作，接著是遷移率的計算，最後完成一個全面性的計算工作。

能帶結構計算和遷移率量測在最近被用來評估在場效電晶體中等效質量隨著應變之下的變化係數。在此論文中，我們提出一個新的實驗方法，乃藉由對<110>方向上的壓縮應變改變（001）n型金氧半場效電晶體的閘極直穿隧電流做匹配動作。這個方法的重點是直穿隧的機制對在等效質量隨著應變之下的變化係數非常敏感，因為變化係數可以影響到次能階的位置。在此，我們使用了一個以

三角位能近似的架構的模擬器。為了達到更精確的成果，我們提出了一個修正係數的演算法去補償使用三角位能近似法解出次能階計算上的誤差。接著用已知的形變位能常數和單向壓縮應力作為輸入的條件，帶有應力效應的量子模擬器就完成了。模擬器計算出的閘極直穿隧電流被用來與實驗比較，因此帶出兩谷和四谷的等效質量隨應變下變化係數的值。其值也跟被發表在文獻的值作比較。

在我們以實驗的方法，透過應力誘發閘極穿隧電流增益，去萃取二維電子氣的等效質量隨應變的變化係數，結果指出導帶中垂直平面方向上(量子侷限)四谷的等效質量隨應變的變化係數是存在的。為了更確定這個事情，在此我們提供了另一個證據。首先，我們針對幾種不同的等效質量隨應變的變化係數的值作為明確的方針。接著，我們採用一個可計算應力和量子效應的自洽的模擬器去執行同時對文獻上在單向拉伸應力的實驗情形下遷移率增加和閘極電流減少作個匹配。發現在能帶計算上忽略了垂直平面方向上四谷的等效質量隨應變的變化係數只會做出很差的匹配結果。

在模擬器結構被建立且可信之下，可使我們的工作延伸到其他情況。除了之前的(001）平面,（110）和（111）的平面場效電晶體中次能階和遷移率的計算也可以用以估計在應力工程下的傳輸特性。穿隧效應在元件微縮下顯得越重要。為了要對三維結構，像是鰭狀場效電晶體的電性做些實驗，雙閘極場效電晶體結構的次能階計算可以直接的達成。計算結果也顯示出在薄基板厚度下特別易有穿隧效應。同樣地，在不同平面不同通道方向的元件時，應力影響遷移率的變化也可以被估計出來。

Sophisticated Quantum Computation on n-type Inversion Layers: Strain, Subband, Mobility, and 3-D Structure

Student: Wei-Han Lee Advisor: Dr. Ming-Jer Chen

Department of Electronics Engineering and Institute of Electronics
National Chiao Tung University

Abstract

Following Moore's law, we are currently entering into the technology generation of 22/20 nm and will keep developing newer and more efficient devices. We will encounter many problems in this long road. Stress engineering is one of the noticeable candidates due to significant changes in electrical performance and process issues. By fitting to the data of leakage current and electron mobility, some physical mechanisms can be brought out. On the other hand, the gate direct tunneling correlates strongly with the band structure, such as the subband energy level and barrier height. Thus, the gate direct tunneling could be a good tool to detect the subband level and hence the effect of stress. To build a correct computation of n-inversion layer in our simulator, this work starts with the fitting to gate direct tunneling data, followed by the mobility calculation brought out in the next step and finally the comprehensive computational work.

Currently, both the band-structure calculation and the mobility measurement are used to assess the electron piezo-effective-mass coefficients in strained nMOSFETs. In this work, we present a new experimental method through a fitting of the

strain-altered electron gate direct tunneling current of (001) n-channel metal–oxide–semiconductor field effect transistors under <110> uniaxial compressive stress. The core of this method lies in the sensitivity of the direct tunneling to the position of the subband level in the presence of the electron piezo-effective-mass coefficients. Here, a simulator based on triangular potential approximation is utilized. To make more accurate calculation, we proposed a new algorithm that a correction-coefficient generating expression is systematically constructed to compensate for the error in the subband levels due to the use of a triangular potential approximation. Then, with the known deformation potential constants and uniaxially compressive stress in the channel as inputs, a strain quantum simulator is carried out. The resulting gate direct tunneling current is used to fit experimental data, thus leading to the values of the piezo-effective-mass coefficients associated with the twofold and fourfold valleys. The comparison of the extracted piezo-effective-mass coefficients with those published in the literature is made.

After we have experimentally extracted the piezo-effective-mass coefficients of 2-D electrons via the stress-induced gate tunneling current enhancement, the results pointed to the existence of a piezo-effective-mass coefficient around the fourfold conduction-band valley in the out-of-plane (quantum confinement) direction. To strengthen this further, here, we provide extra evidence. First, explicit guidelines are drawn to distinguish all the piezo-effective-mass coefficients. Then, a self-consistent strain quantum simulation is executed to fit literature data of both the mobility enhancement and gate current suppression in the uniaxial tensile stress situation. It is found that neglecting the fourfold-valley out-of-plane piezo-effective-mass coefficient, as in existing band structure calculations, only leads to a poor fitting.

As the structure of our simulator is built and valid, our work could extend to other cases. In addition to (001) case, the subband and mobility calculation in (110) and (111) planar MOSFETs can accountable the transport characteristics under strain. The effect of wave-function penetration is significant as the device is scaled. To examine the electrical characteristics in 3-D structures device such as FinFETs, the subband calculation in double-gate structures can be straightforwardly achieved. The results exhibit the penetration effect especially in thin silicon films. Again, the stress-induced mobility variations can be estimated for devices with different channel directions and different surface orientations.

Acknowledgements

首先，我要感謝我的指導老師，陳明哲教授。他以身作則的教導我做學問的精神。”求真”、”勇往直前”這些話會永遠的迴盪在我的腦海中。陳教授不但在學問上，在做人處事方面也有很多讓我仰望學習的地方，遇到很多事情他都是哈哈大笑地去面對，而且教導我們要與人為善，更不用說多次的容忍我的粗心和愚笨。我真的是非常的幸運可以接受陳教授的薰陶。

再來，我要感謝所有的朋友，不管是相處很久的學校同學，還是短短相聚的營隊朋友，每個人在一路上都扮演了重要的腳色，沒有他們就沒有今天的我。

最後我要感謝我的父母親，他們無怨無悔無私的將歲月奉獻給我，與我分享他們所有的一切，他們對我的愛雖無言語明講，卻可以默默的從他們的行為感受到一切。他們只求我變得成熟穩重。如今，我終於有能力去回報這份幸福的羈絆了。

Contents

Table Captions

Chapter 3

Chapter 4

Chapter 6

Figure Captions

Chapter 2

Chapter 3

Chapter 4

Chapter 5

Chapter 6

Chapter 1

Introduction

1.1 Motivation

During the period of increasing device density in silicon integrated circuits, many problems are encountered and needed to be solved, such as the degradation of mobility, increasing of the leakage current, enhancement of the DIBL effect, and the existence of process-induced mechanical stress. Many researchers tried replacement materials of silicon while other researchers pointed out that the applied stress as well as non-planar structures can be utilized to improve the electrical properties.

The planar MOSFET with its single gate is the general structure of device. The control ability of its single gate is designed with the scaling down. Other novel structures, such as double-gate MOSFET, FinFET, and nanowire, could help increase the control of the gate and decrease the parasitic capacitance. Those could improve the annoying short channel effect. As the particle is confined strongly, some physical effects emerge. The particle penetration into the gate barrier is getting easier. Thus, we should take more care about the resulting tunneling current across the gate dielectrics. Furthermore, the particle is easily confined by space barrier instead of interior electric field, the case of “volume inversion”.

Strain has one main effect in term of the energy band shift and warp is (especially for hole), which in turn affects the electrical performance such as mobility [1.1]-[1.3], threshold voltage [1.4], and gate direct tunneling current [1.5]-[1.7]. These are due to the strain-induced band distortion that changes the energy level, population, effective mass and scattering time in each valley. To take the merits of the strain effect, many of the processes used in silicon IC fabrication individually and cooperatively contribute to the development of favorable stress as in the silicon active region.

Some researches also mentioned that the process induced stress has influence on the gate oxide, such as integrity and growth rate. This can induce more leakage current across the gate. In the IC industry nowadays, tunneling is a terrible phenomenon such as standby power consumption, leakage current in C-V measurement, etc. [1.8]-[1.9]. Thus, a computationally efficient and reasonable physical model for characterizing the gate direct tunneling current of strained silicon device is essential. Besides, the more efficient and faster device is needed in each generation, especially for high mobility. Applied stress is one of the methods that can boost mobility. Thus, physical model that can estimate mobility under stress is needed.

From the gate direct tunneling current and mobility of the strained nMOSFETs, two important physical phenomena are brought out and provided. One is the growth rate of silicon dioxide effects by process stress; another is that effective mass varies with stress as that can be quantified by piezo-effective-mass coefficients. By fitting to the experimental data, both of them can be extracted.

To understand the physics of these situations, we have built a sophisticated calculation tool to simulate the electrical properties of nMOSFET. Although the existing programs are popular in the field, the code is not available and difficult to modify. On the other hand, our simulator built on *MATLAB* is a good tool to provide enough information for our research. In this thesis, we show the applicability and validity of our simulator in deal with the gate direct tunneling current and mobility.

1.2 Dissertation Organization

In Chapter 2, a simulator based on a triangular potential approximation, named "*TRP*", is introduced. However, a huge error is accompanied with this method. New algorithm with a corrected coefficient "η_i" embedded in original *TRP*, is proposed to eliminate this error.

In Chapter 3, the strain and stress are introduced. The band shift caused by strain is considered in *TRP*. From the fitting of experimental gate direct tunneling current data by *TRP*, the importance and values of the piezo-effective-mass coefficients are brought out. We also compare those extracted piezo-effective-mass coefficients with those published in the literature.

In Chapter 4, a powerful simulator of fully Schrődinger and Poisson self-consistent solver for n-channel MOSFETs, named "*NEP*", is presented. With the outputs such as subband energy level, inversion charge density, wave-function, etc., we can estimate mobility with key scattering mechanisms included. Gate direct tunneling can be gotten form *NEP*. Once again, stress effect is considered inside *NEP*.

In Chapter 5, from the fitting of experimental gate direct tunneling current and mobility at the same time, we provide another evidence for the existence and importance of the piezo-effective-mass coefficients.

In Chapter 6, each of (001), (110), and (111) nMOSFETs are discussed under longitudinal, transverse, vertical, and biaxial stress conditions. The double-gate version of the simulator is introduced.

Finally, conclusions of the research work and made in Chapter 7.

References

[1.1] J. Welser, J. L. Hoyt, and J. F. Gibbons, “NMOS and PMOS transistors fabricated in strained silicon/relaxed silicon-germanium structures,” in *IEDM Tech. Dig.*, 1992, pp. 1000-1002.

[1.2] C. H. Ge, C. C. Lin, C. H. Ko, C.C. Huang, Y. C. Huang, B. W. Chan, B. C. Perng, C. C. Sheu, P. Y. Tsai, L. G. Yao, C. L. Wu, T. L. Lee, C. J. Chen, C. T. Wnag, S. C. Lin, Y. C. Yeo, and C. Hu, “Process-strained Si (PSS) CMOS technology featuring 3D strain engineering,” in *IEDM Tech. Dig.*, 2003, pp. 73-76.

[1.3] S. E. Thompson, M. Armstrong, C. Auth, M. Alavi, M. Buehler, R. Chau, S. Cea, T. Ghani, G. Glass, T. Hoffman, C. H. Jan, C. Kenyon, J. Klaus, K. Kuhn, Z. Ma, B. Mcintyre, K. Mistry, A. Murthy, B. Obradovic, R. Nagisetty, P. Nguyen, S. Sivakumar, R. Shaheed, L. Shifren, B. Tufts, S. Tyagi, M. Bohr, and Y. El-Mansy, “A 90-nm logic technology featuring strained-silicon,” *IEEE Trans. Electron Devices*, vol. 51, no. 11, pp. 1790-1797, Nov. 2004.

[1.4] J. S. Lim, S. E. Thompson, and J. G. Fossum, “Comparison of threshold-voltage shifts for uniaxial and biaxial tensile-stressed n-MOSFETs,” *IEEE Electron Device Lett.*, vol. 25, no. 11, pp. 731-733, Nov. 2004.

[1.5] A. Hamada, T. Furusawa, N. Saito, and E. Takeda, “A new aspect of mechanical stress effects in scaled MOS devices,” *IEEE Trans. Electron Devices*, vol. 38, no. 4, pp. 895-900, Apr. 1991.

[1.6] W. Zhao, A. Seabaugh, V. Adams, D. Jovanovic, and B. Winstead, “Opposing dependence of the electron and hole gate currents in SOI MOSFETs under uniaxial strain,” *IEEE Electron Device Lett.*, vol. 26, no. 6, pp. 410-412, Jun. 2005.

[1.7] X. Yang, J. Lim, G. Sun, K. Wu, T. Nishida, and S. E. Thompson, "Strain-induced changes in the gate tunneling currents in p-channel metal-oxide-semiconductor field-effect transistors," *Appl. Phys. Lett.*, vol. 88, no. 5, pp. 052108-1-052108-3, Jan. 2006

[1.8] S. H. Lo, D. A. Buchanan, Y. Taur, and W. Wang, "Quantum-mechanical modeling of electron tunneling current from the inversion layer of ultra-thin-oxide nMOSFETs," *IEEE Electron Device Lett.*, vol. 18, no. 5, pp. 209-211, May 1997.

[1.9] K. N. Yang, H. T. Huang, M. C. Chang, C. M. Chu, Y. S. Chen, M. J. Chen, Y. M. Lin M. C. Yu, M. Jang, C. H. Yu, and M. S. Liang, "A physical model for hole direct tunneling current in p+ poly-gate pMOSFETs with ultrathin gate oxides," *IEEE Trans. Electron Devices*, vol. 47, no. 11, pp. 2161-2166, Nov. 2000.

[1.10] Y. T. Hou, M. F. Li, Y. Jin, and W. H. Lai, "Direct tunneling hole currents through ultrathin gate oxides in metal-oxide-semiconductor devices," *J. Appl. Phys.*, vol. 91, no. 1, pp. 258-264, Jan. 2002.

Chapter 2

Triangular Potential based Simulator

2.1 Introduction

A simulator based on a triangular potential approximation, named *TRP*, is presented in this chapter. Some electrical properties of nMOSFET are calculated by *TRP*. However, when comparing with the self-consistent Schrődinger and Poisson's equations solver, *Schred* [2.1], unacceptable error appears. Thus, a new algorithm is proposed and incorporated to correct the error.

2.2 Triangular Potential Approximation

2.2.1 Physical Model

The description below is dedicated to the case of (100) nMOSFET. The energy band diagram of poly-gate MOSFET is given in Fig. 2.1, where V_s, V_{ox}, and V_{poly} are the potential drop in the Si substrate, silicon dioxide, and poly gate region, respectively, E_f is the electron Fermi level, and F_s is the surface electric field. This band diagram is characterized by F_s. As we give a value of F_s, the V_{ox} is calculated via continuous electric displacement (i.e., no charge) at the interface:

$$V_{ox} = F_s \frac{\varepsilon_{si}}{\varepsilon_{ox}} t_{ox} \tag{2.1}$$

where ε_{si} and ε_{ox} are the permittivity of silicon and silicon dioxide, respectively. V_{poly}

in the poly depletion region can be calculated:

$$V_{poly} = \frac{\varepsilon_{si} F_s^2}{2qN_{poly}} \tag{2.2}$$

where q is the elementary charge of an electron and N_{poly} is the doping concentration of poly gate. V_s can be expressed as a function of the gate bias Vg:

$$V_s = V_g - V_{ox} - V_{poly} + V_{fb} \tag{2.3}$$

where the flat band voltage V_{fb} is calculated as:

$$V_{fb} = -k_B T \ln\left(\frac{N_{poly} N_{sub}}{n_i^2}\right) \tag{2.4}$$

where N_{sub} is the doping concentration of substrate, n_i is the intrinsic carrier density in substrate, k_B is the Boltzmann's constant, and T is the absolute temperature. The solving of the Schrődinger equation in the quantum-confined direction normal to the SiO_2/Si surface yields the $\varDelta_2$ subband level i in the absence of the stress [2.2]:

$$E_{\Delta 2,i} = \left(\frac{\hbar^2}{2m_{z,\Delta 2}}\right)^{\frac{1}{3}} \left(\frac{3}{2}\pi q F_s \left(i - \frac{1}{4}\right)\right)^{\frac{2}{3}} \tag{2.5}$$

The average depth of the 2DEG is:

$$Z_{\Delta 2,i} = 2E_{\Delta 2,i} / 3qF_s \tag{2.6}$$

where $m_{z,\varDelta 2}$ is the $\varDelta_2$ quantization effective mass, $\hbar$ is the Planck's constant divided by 2π. Eq. (2.5) can apply to 4-fold case by replacing $\varDelta_2$ with $\varDelta_4$. From Fig. 2.1, the Fermi level is related to the surface potential:

$$E_f = V_s - E_g - k_B T \ln(\frac{N_{sub}}{N_v}) \tag{2.7}$$

where Eg is the energy gap of silicon, N_v is the effective density of states in valence band. With Eq. (2.5) and (2.7), we can get the charge density for each subband [2.3]:

$$N_{\Delta 2/4,i} = g_{\Delta 2/4}(\frac{m_{d,\Delta 2/4} k_B T}{\pi \hbar^2}) \ln(1 + \exp(\frac{E_f - E_{\Delta 2/4,i}}{k_B T})) \tag{2.8}$$

where $g_{\Delta 2/4}$ is the Δ_2 / Δ_4 valley degeneracy; and $m_{d,\Delta 2/4}$ is the 2-D density-of-states (DOS) effective mass of the Δ_2 / Δ_4 valley.

The surface drop due to bulk depletion V_{dep} and 2D depletion charge density N_{dep} are [2.2]:

$$V_{dep} = V_s - \frac{qN_{inv} Z_{qm}}{\varepsilon_{si}} - \frac{k_B T}{q} \tag{2.9}$$

$$N_{dep} = \sqrt{\frac{2\varepsilon_{si} V_{dep} N_{sub}}{q}} \tag{2.10}$$

where N_{inv} is 2D inversion charge density which is equal to the summation of $N_{\Delta 2/4,i}$, and Z_{qm} is the average penetration of the inversion-layer charge from the surface. As we give a gate voltage V_g as input, initial F_s is guessed until it is consistently equal to $q(N_{inv} + N_{dep}) / \varepsilon_{si}$ according to *Gauss* law. The flow chart is presented in Fig. 2.2. On the other hand, if the device is manufactured by metal gate, the potential drop of metal gate is equal to zero and the flat band voltage relates to work function.

2.2.2 Outcome of *TRP*

In Fig. 2.3, the resulting conduction potential profile is shown, along with five lowest subband levels for (100) nMOSFETs in terms of three of Δ_2 subband and two of Δ_4 subbnad. We show both cases of poly silicon and metal gate. To examine the validity of the triangular potential approximation, a self-consistent Poisson-Schrödinger equations solver, *Schred* [2.1], was used and the resulting subband levels are shown in Fig. 2.3. In the figure, the drawback of the conventional triangular potential approximation is clear, especially in the higher energy levels where the corresponding electric field deviates from the surface field F_s, as shown in Fig. 2.1.

2.3 Correction Coefficient Generator

To address this issue, different methods have been proposed previously: (i) the variation approach dedicated to the correction of the lowest subband [2.2], [2.4]; and (ii) the effective field F_{eff} to replace F_s in Eq. (2.5) [2.5]-[2.10]:

$$F_{eff} = \frac{q(\eta N_{inv} + N_{dep})}{\varepsilon_{si}} \qquad (2.11)$$

The correction coefficient η in Eq. (2.11) is constant with a spanned range from 0.5 to 1.0: $\eta = 0.75$ for Δ_2 and 1.0 for Δ_4 [2.5], [2.6]; $\eta = 0.5$ for all subbands [2.7]; and $\eta =$ 0.75 for all subbands [2.8]-[2.10]. However, the previous improvements that led to Eq. (2.11) are not enough from the aspect of the direct tunneling: each of the subbands involved in the tunneling should have its own correction coefficient such as to ensure the proper direct tunneling calculation. Obviously, due to different electric fields encountered from level to level as revealed in Fig. 2.1, different correction coefficient values should correspond to different subbands. To take this into account, we suggest the individual correction coefficient $\eta_{\Delta 2,i}$ for the Δ_2 level i and the corresponding effective electric field can be written as:

$$F_{\Delta 2,i} = \frac{q(\eta_{\Delta 2,i} N_{inv} + N_{dep})}{\varepsilon_{si}} \tag{2.12}$$

The same procedure can apply to Δ_4 case: $F_{\Delta 4,i}$ corresponds to $\eta_{\Delta 4,i}$. Again, to quantify the correction coefficient values, the solver *Schred* [2.1] was conducted in a MOS system on (001) silicon surface. A wide range of the key process parameters was included: the substrate doping concentration N_{sub}= 10^{15}, 10^{16}, 10^{17}, and 10^{18} cm^{-3}; the gate oxide thickness t_{ox} = 1, 3, and 6 nm; and the different gate stacks in terms of a polysilicon and a metal electrode. By matching the subband levels produced by *Schred* with those from Eq. (2.5) (with F_s replaced by $F_{\Delta 2,i}$ for 2-fold valley and $F_{\Delta 4,i}$ for 4-fold valley), the values of the $\eta_{\Delta 2,i}$ and $\eta_{\Delta 4,i}$ result. A scatter plot between the correction coefficient values and the corresponding subband levels is given in Fig. 2.4, which is made with the surface field F_s as a parameter. Strikingly, the figure points to two relevant relationships. First, under fixed F_s, all data points fall on or around a straight line, indicating that the correction coefficient depends linearly on the subband level. Second, the straight line appears to shift with F_s. This specific behavior can be modeled by the intercept, designated as η_o, of the extrapolated line at zero subband level. In the inset of the figure, η_o is plotted against F_s, clearly showing another linear relationship, regardless of the N_{sub}, t_{ox}, or gate stack material. This is expected from the aspect of the MOS electrostatics. The combination of these two linear relationships therefore leads to a subband-level correction-coefficient generating expression suitable for both Δ_2 and Δ_4 [2.11]:

$$\eta_{\Delta 2/4,i} = -0.003E_{\Delta 2/4,i} + (1.01 + 0.308F_s) \tag{2.13}$$

The units of $E_{\Delta 2/4i}$ and F_s in Eq. (2.13) are meV and MV/cm, respectively. Eq. (2.13) can provide a transparent understanding of the effect of the subband level and surface field on the calculated correction coefficient. Interestingly, Eq. (2.13) is also self-consistent: for those of the subband levels close to the reference point (that is, the classical conduction band edge at the surface), the correction coefficients lie in close proximity of unity and hence the effective electric field approaches the surface one. To testify to the validity of Eq. (2.13) in the subband level calculation, the results are compared with those from *Schred* [2.1], as given in Fig. 2.5 for two different gate stacks. Excellent agreements are evident, obtained without adjusting any parameters. Note that the expression Eq. (2.13) is valid only for (001) substrate. Further study is needed concerning the underlying physical origins as well as its applicability to other substrate orientations. We think that the two linear relationships in Fig. 2.4 may be helpful in this direction.

References

[2.1] Schred. [Online]. Available: http://nanohub.org/resources/schred.

[2.2] F. Stern, “Self-consistent results for n-type Si inversion layers,” *Phys. Rev. B*, vol. 5, no.12, pp.4891-4899, Jun. 1972.

[2.3] F. Stern and W. E. Howard, “Properties of semiconductor surface inversion layers in the electric quantum limit,” *Phys. Rev.*, vol. 163, no. 3, pp. 816–835, Oct. 1967.

[2.4] N. Yang, W. K. Henson, J. R. Hauser, and J. J. Wortman, “Modeling study of ultrathin gate oxides using direct tunneling current and capacitance-voltage measurements in MOS devices,” *IEEE Trans. Electron Devices*, vol. 46, no. 7, pp. 1464–1471, Jul. 1999.

[2.5] J. S. Lim, X. Yang, T. Nishida, and S. E. Thompson, “Measurement of conduction band deformation potential constants using gate direct tunneling current in *n*-type metal oxide semiconductor field effect transistors under mechanical stress,” *Appl. Phys. Lett.*, vol. 89, no. 7, pp. 073509-1-073509-3, Aug. 2006.

[2.6] C. Y. Hsieh and M. J. Chen, “Measurement of channel stress using gate direct tunneling current in uniaxially stressed nMOSFETs,” *IEEE Electron Device Lett.*, vol. 28, no. 9, pp. 818-820, Sept. 2007.

[2.7] C. K. Park, C. Y. Lee, B. J. Moon, Y. H. Byun, and M. Shur, “A unified current-voltage model for long-channel nMOSFET’s,” *IEEE Trans. Electron Devices*, vol. 38, no. 2, pp. 399-406, Feb. 1991.

[2.8] Y. Ma, L. Liu, Z. Yu, and Z. Li, “Validity and applicability of triangular potential well approximation in modeling of MOS structure inversion and accumulation layer,” *IEEE Trans. Electron Devices*, vol. 47, no. 9, pp. 1764-1767, Sept. 2000.

[2.9] Y. T. Hou, M. F. Li, Y. Jin, and W. H. Lai, “Direct tunneling hole currents through ultrathin gate oxides in metal-oxide-semiconductor devices," *J. Appl. Phys.*, vol. 91, no. 1, pp. 258–264, Jan. 2002.

[2.10] H. Abebe, E. Cumberbatch, H. Morris, and V. Tyree, "Compact models of the quantized sub-band energy levels for MOSFET device application," in *IEEE UGIM Proceedings*, 2008, pp. 58-60.

[2.11] W. H. Lee and M. J. Chen, "Gate direct tunneling current in uniaxially compressive strained nMOSFETs: a sensitive measure of electron piezo effective mass," *IEEE Trans. Electron Devices*, vol. 58, no. 1, pp. 39-45, Jan. 2011.

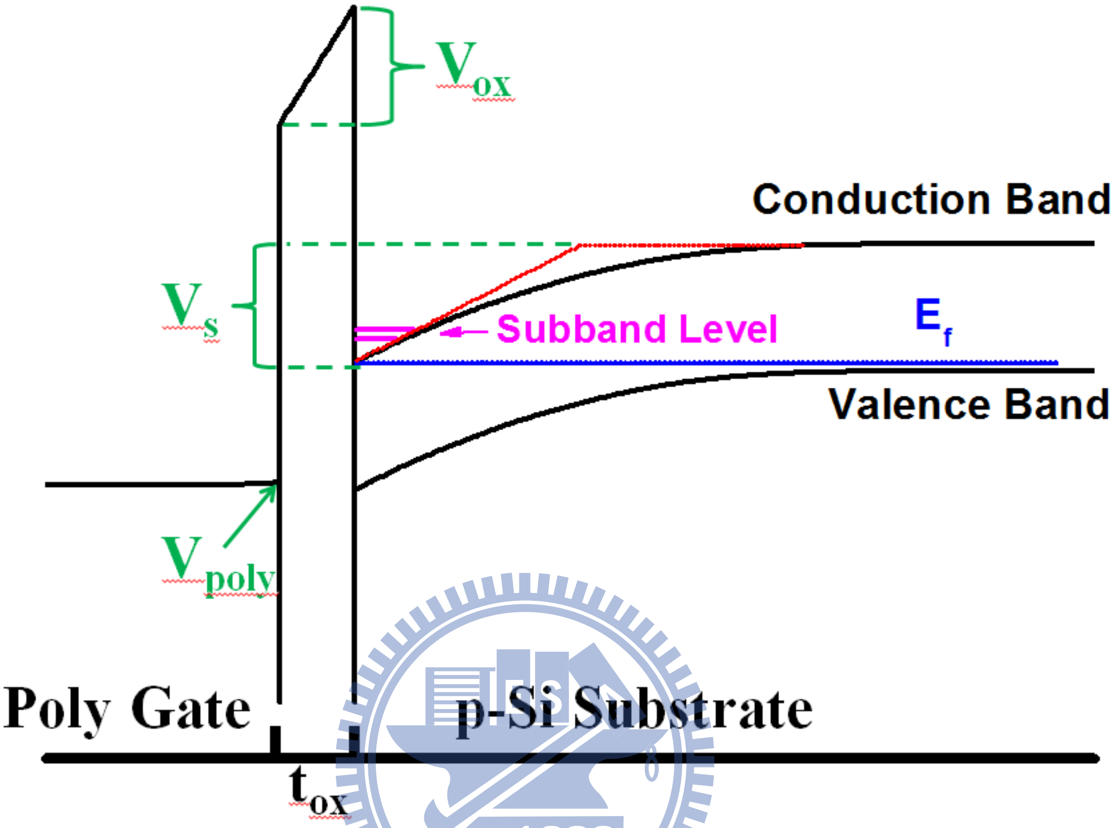

Fig. 2.1 Silicon energy-band diagram produced by *Schred* [2.1] (black lines), two calculated subband energy level (pink lines), and the Fermi level (blue line), as well as the red line for the triangular potential approximation under the same surface field.

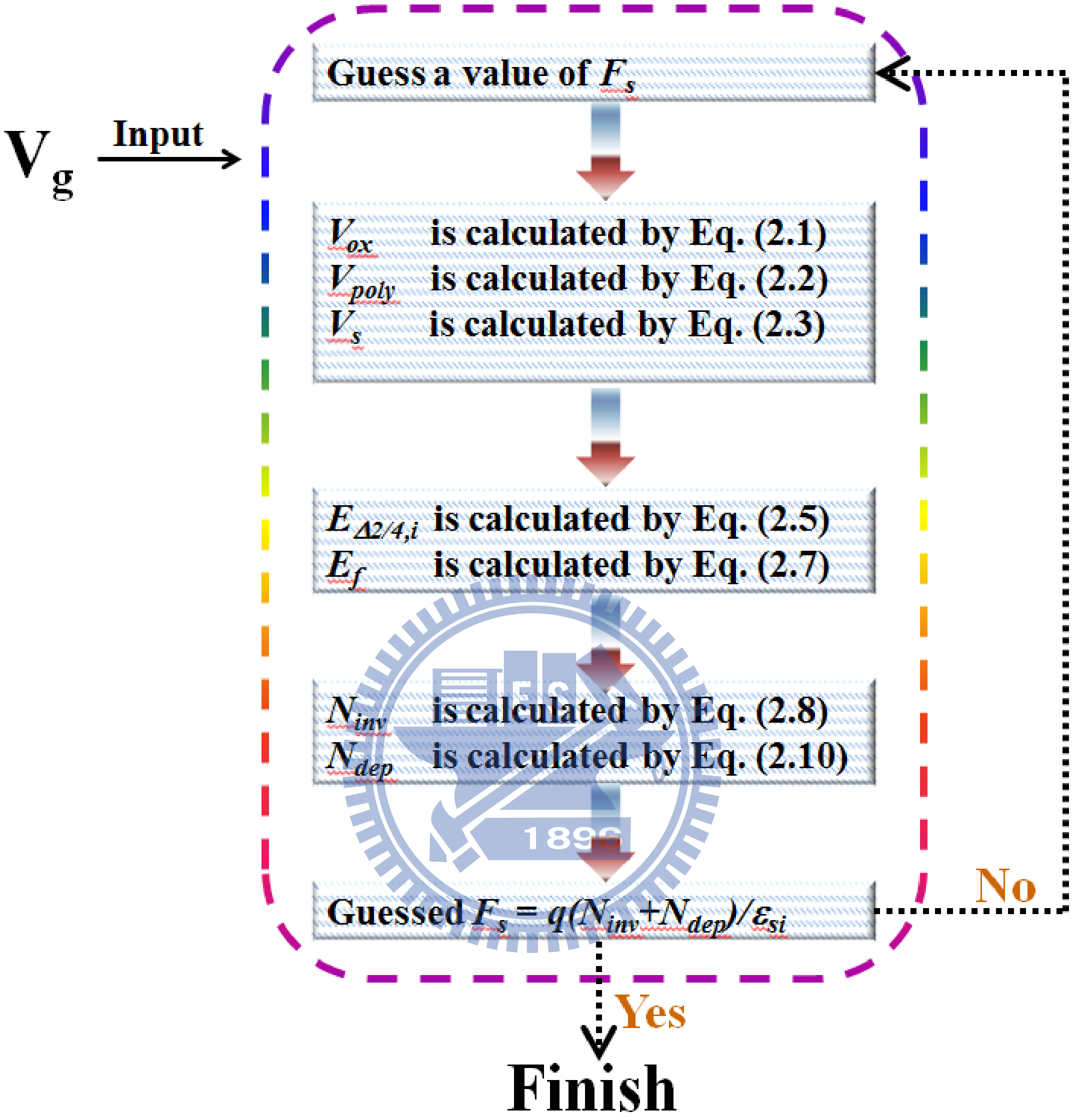

Fig. 2.2 The flow chart of the calculation process inside the *TRP*.

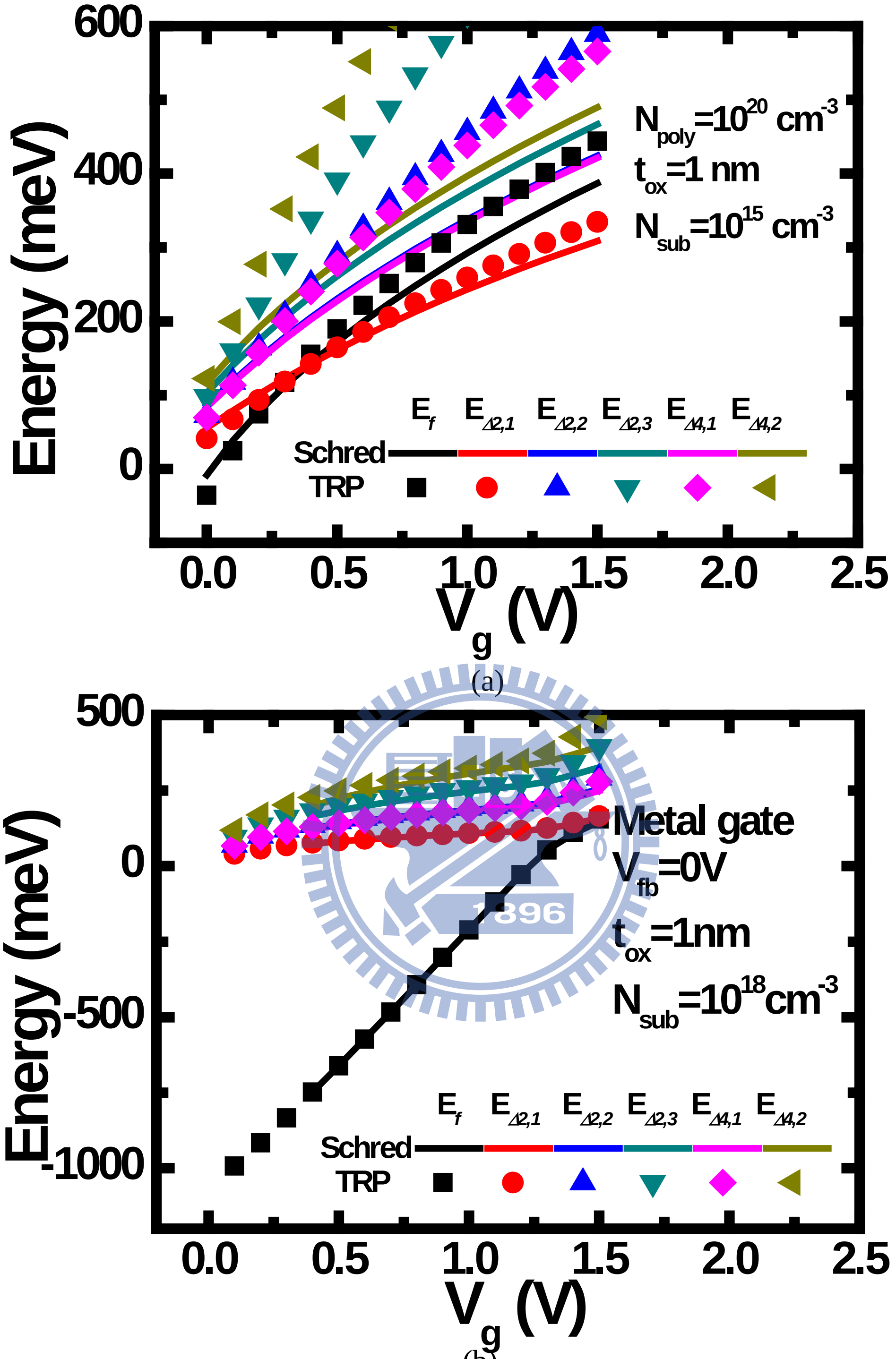

(b)

Fig. 2.3 Subband levels calculated by the triangular potential approximation (solid dots) and by *Schred* (lines) for two cases: (a) n+ poly silicon doping $N_{poly} = 10^{20}$ cm^{-3}, $t_{ox} = 1$ nm, and $N_{sub} = 10^{15}$ cm^{-3}; and (b) metal gate with zero flat-band voltage, $t_{ox} = 1$nm, and $N_{sub} = 10^{18}$ cm^{-3}.

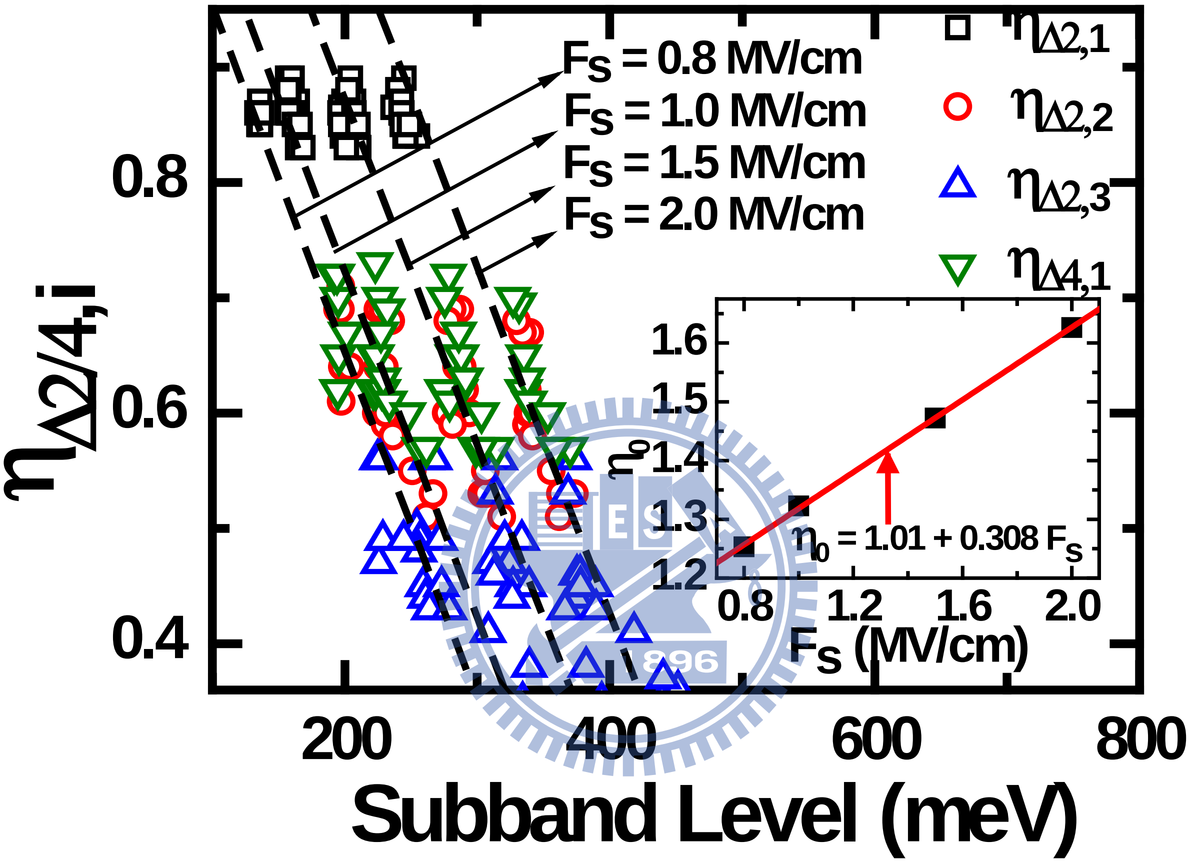

Fig. 2.4 The extracted correction coefficient versus the corresponding subband level with the surface field as a parameter. The fitting lines are drawn. The intercept, η_o, of the extrapolated line at the zero subband level is inserted and plotted versus the surface field. A fitting line is also shown in the inset.

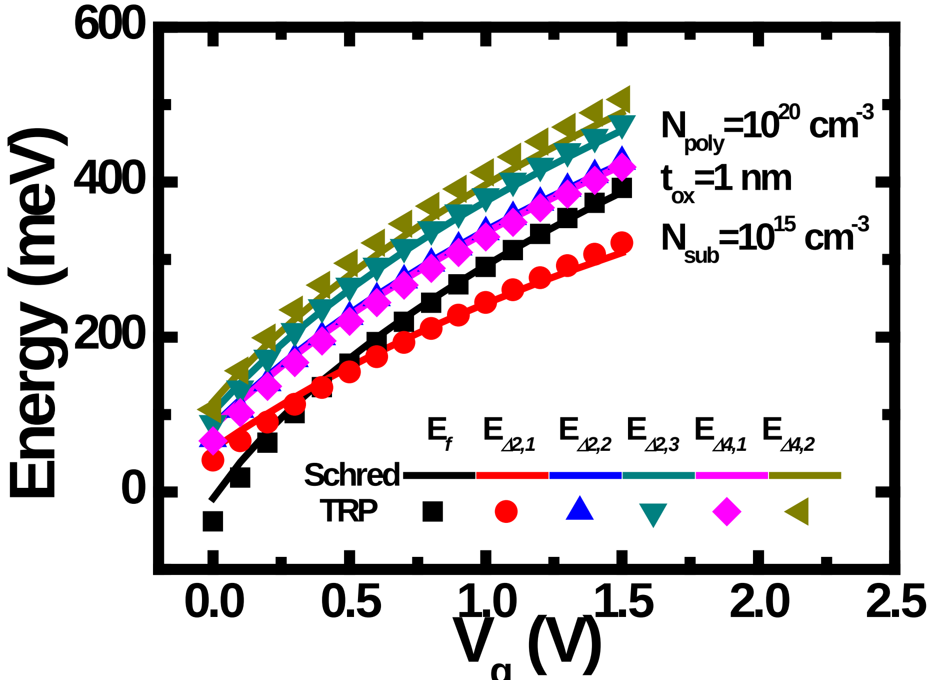

(a)

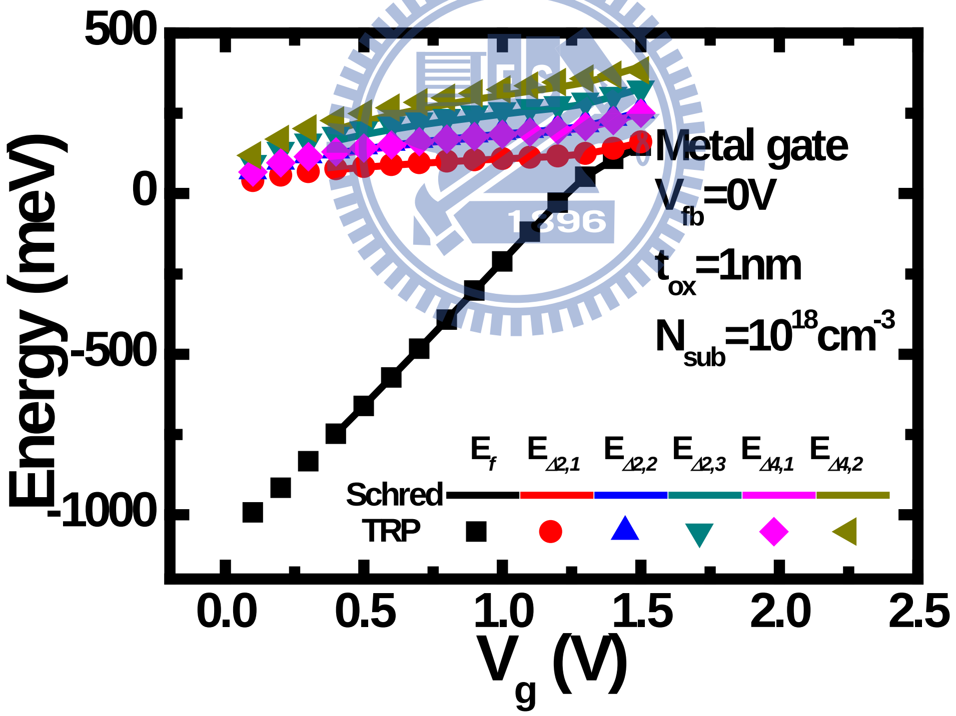

(b)

Fig. 2.5 Repeating the calculation work by the triangular potential approximation based on the new η correction generator.

Chapter 3
Strain Altered Electron Gate Direct Tunneling Current

3.1 Introduction

In this chapter, we discuss about the model of conduction band electron direct tunneling (EDT) current. For the silicon nMOSFETs formed on (001) substrate, the quantum confinement effect [3.1] around the inversion layer makes the bulk conduction band split into two distinctive components: 2-fold (Δ_2) and 4-fold (Δ_4) valleys. The longitudinal effective mass (m_l) and transverse effective mass (m_t) associated with those subband valleys essentially remain intact [3.1]. The energetic difference between Δ_2 and Δ_4 levels can be further changed via the applied mechanical stress as in the state-of-the-art strain engineering. The stress induced subband shift has been thoroughly studied theoretically [3.2] in terms of the deformation potential constants [3.3]-[3.5]. Thus, the change ratio of EDT current under strain can be estimated.

Comparing with the experimental data of EDT current [3.6], [3.7], one important physical phenomenon can be brought out: the effective mass of electron varies with applied stress. Recently, the sophisticated band-structure calculation [3.8]-[3.10] on (001) silicon surface has pointed out that only with the strain dependence of m_l and m_t taken into account can the strain induced mobility change be elucidated. The significance of the strain dependent electron effective masses in (110) case has also been mentioned [3.11]. Thus, in addition to the deformation potential counterparts, the strain dependence of m_l and m_t or equivalently the electron piezo-effective-mass coefficient, π_m, should not be absent in the strain altered conduction-band structure.

The mobility measurement method has been constructed to experimentally determine the π_m of electrons [3.12]. On the other hand, the effect of the mechanical stress on the electron gate direct tunneling current has been experimentally observed [3.6], [3.7], [3.13]-[3.17]. In the citations [3.6], [3.7], [3.13]-[3.17], however, the impact of the π_m on the strained electron gate direct tunneling current has not been noticed. According to the quantum confinement picture [3.1], a change in the electron quantization effective mass due to the stress will produce a change in the subband level and therefore change the transmission probability dramatically. Thus, through the inverse modeling technique, the electron gate direct tunneling current in strained device may serve as a sensitive detector of π_m. However, few studies on this subject were done to date..

3.2 Strain-Altered Band Structures

In this section, we make a connection between the strain and the stress. Notice that the temperature-induced strain does not be considered here. Stress is the average force over the area on which the force acts. Thus, the intensity of stress is expressed as function of applied force per area. The force applied on an area can be separated into two directions: out-of-plane direction (normal force) and in-plane direction (shear force). The stress caused by normal/shear force is called normal/shear stress.

For a force F applied on an infinitesimal area A which is normal to the z direction, as show as in Fig. 3.1, the projected quantity of the force along x, y, and z are F_x, F_y, and F_z, respectively. Then the normal stress σ_{zz} and shear stress τ_{zx} and τ_{zy} are defined:

$$\sigma_{zz} = \lim_{A\to 0}\frac{F_z}{A} \tag{3.1a}$$

$$\tau_{zx} = \lim_{A\to 0}\frac{F_x}{A} \tag{3.1b}$$

$$\tau_{zy} = \lim_{A\to 0}\frac{F_y}{A} \tag{3.1c}$$

The notation σ_{ii} refers to the normal stress acting on the plane perpendicular to i-direction, and τ_{ij} refers to the shear stress component along j-direction acting on the plane perpendicular to i-direction.

Furthermore, we consider the case of an infinitesimal cube whose six surfaces face to ±x, ±y, and ±z. There should be 18 stress components by Eq. (3.1). However, two conditions are observed: (1) F_x and F_{-x} are reaction force of each other; (2) $\tau_{xy}= \tau_{yx}$, $\tau_{yz}= \tau_{zy}$, and $\tau_{zx}= \tau_{xz}$ can be derived because of the total applied force and torque on the cube are zero. Thus, stress tensor is simplified to the only 6 terms [3.18]:

$$\sigma = \begin{bmatrix} \sigma_{xx} \\ \sigma_{yy} \\ \sigma_{zz} \\ \tau_{yz} \\ \tau_{zx} \\ \tau_{xy} \end{bmatrix} \tag{3.2}$$

It is notable that the tensile stress is shown as positive value. On the other hand, the compressive stress is the negative value. With external stress, a deformable body changes its size and shape. In Fig. 3.2(a), a normal tensile force along x-direction σ_{xx} is applied on deformable body and the length along x-direction is increased. The normal strain is defined:

$$\varepsilon_{xx} = \frac{\Delta L_x}{L_x} \tag{3.3}$$

Again, positive ε means the length elongates, a situation called tensile strain. Negative ε means that the length is contracted, the case compressive strain.

In Fig. 3.2(b), a shear stress τ_{zy} is applied on a planar body that causes the change of its shape. The angle varies from π/2 to 0. Besides, the lengths of four side lines are unchanged. The shear strain γ_{zy} is defined as the change in the angle between two neighbor sidelines of the square on y-z surface [3.18]:

$$\gamma_{zy} = 2\varepsilon_{zy} = \frac{\partial u_z}{\partial y} + \frac{\partial u_y}{\partial z} \tag{3.4}$$

where u_z and u_y mean the displacements along z- and y-direction respectively. γ_{zy} presents the shear strain, and ε_{zy} is the average shear strain equal to the half of γ_{zy} [3.18]-[3.20].

Similar to stress tensor, the strain tensor is also composed of six independent components:

$$\varepsilon = \begin{bmatrix} \varepsilon_{xx} \\ \varepsilon_{yy} \\ \varepsilon_{zz} \\ \gamma_{yz} \\ \gamma_{zx} \\ \gamma_{xy} \end{bmatrix} \tag{3.5}$$

When a stress is applied to a homogeneous and isotropic material, the normal strain has a linear relationship with normal stress, which is the well-known Hooke's Law [3.18]-[3.20]:

$$\sigma = E\varepsilon \tag{3.6}$$

where the constant of proportionality E is the Young's modulus. Furthermore, while the normal stress is applied on elastic material, the strain transversal to stress usually accompanies. The relationship between normal strain and transverse strain is [3.18]-[3.20]:

$$\varepsilon_{tran} = -v\varepsilon_{long} \tag{3.7}$$

where the constant of proportionality v is the Poisson's ratio. Finally, the Hooke's law still holds for shear strain [3.18]-[3.20]:

$$\tau = G\gamma \tag{3.8}$$

where the constant of proportionality G is the shear modulus.

With Eq. (3.6)-(3.8), the relation between strain and stress is:

$$\varepsilon_{xx} = \frac{1}{E}[\sigma_{xx} - v(\sigma_{yy} + \sigma_{zz})] \tag{3.9a}$$

$$\varepsilon_{yy} = \frac{1}{E}[\sigma_{yy} - v(\sigma_{xx} + \sigma_{zz})] \tag{3.9b}$$

$$\varepsilon_{zz} = \frac{1}{E}[\sigma_{zz} - v(\sigma_{xx} + \sigma_{yy})] \tag{3.9c}$$

$$\gamma_{xy} = \frac{1}{G}\tau_{xy} \tag{3.9d}$$

$$\gamma_{yz} = \frac{1}{G}\tau_{yz} \tag{3.9e}$$

$$\gamma_{xz} = \frac{1}{G}\tau_{xz} \tag{3.9f}$$

For simplicity, we usually transfer the strain and stress relationships to the matrix form. With Eq. (3.2), (3.5), and (3.9), the elastic relationship between strain and stress is established [3.18]-[3.22]:

$$\begin{bmatrix} \varepsilon_{xx} \\ \varepsilon_{yy} \\ \varepsilon_{zz} \\ 2\varepsilon_{yz} \\ 2\varepsilon_{zx} \\ 2\varepsilon_{xy} \end{bmatrix} = \begin{bmatrix} S_{11} & S_{12} & S_{12} & 0 & 0 & 0 \\ S_{12} & S_{11} & S_{12} & 0 & 0 & 0 \\ S_{12} & S_{12} & S_{11} & 0 & 0 & 0 \\ 0 & 0 & 0 & S_{44} & 0 & 0 \\ 0 & 0 & 0 & 0 & S_{44} & 0 \\ 0 & 0 & 0 & 0 & 0 & S_{44} \end{bmatrix} \begin{bmatrix} \sigma_{xx} \\ \sigma_{yy} \\ \sigma_{zz} \\ \tau_{yz} \\ \tau_{zx} \\ \tau_{xy} \end{bmatrix} \tag{3.10}$$

where S is the compliance coefficient. S_{11} is equal to $1/E$, S_{12} is equal to $-v/E$, and S_{44} is equal to $1/G$. For the silicon case, the experimental values are: $S_{11} = 7.68\text{x}10^{-12}$ m^2/N, $S_{12} = -2.14\text{x}10^{-12}$ m^2/N, and $S_{44} = 12.6\text{x}10^{-12}$ m^2/N [3.23]-[3.26].

In deformation potential theory, the total Hamiltonian for each energy valleys of silicon conduction band is [3.27]:

$$H = (\frac{\hbar^2(k_l - k_0)^2}{2m_l} + \frac{\hbar^2 k_t^{\ 2}}{2m_l} + E_c) + (\Xi_d Tr(\varepsilon_{ij}) + \Xi_u \varepsilon_l) \tag{3.11}$$

where k_l and k_t are the wavevectors parallel and perpendicular to the axis where the valleys are located, respectively, Ξ_d and Ξ_u are the hydrostatic and shear deformation potential constants, respectively, $Tr(\varepsilon_{ij})$ is the trace of the strain tensor. And Ξ_d = 1.13 eV and Ξ_u = 9.16 eV are given in silicon case [3.26], ε_l is the longitudinal strain component. Appling Eq. (3.11), the band edge shift for the minima of the six conduction band valleys along the <100> direction is:

$$\Delta E_{c,x} = \Xi_d(\varepsilon_{xx} + \varepsilon_{yy} + \varepsilon_{zz}) + \Xi_u \varepsilon_{xx} \tag{3.12a}$$

$$\Delta E_{c,y} = \Xi_d(\varepsilon_{xx} + \varepsilon_{yy} + \varepsilon_{zz}) + \Xi_u \varepsilon_{yy} \tag{3.12b}$$

$$\Delta E_{c,z} = \Xi_d(\varepsilon_{xx} + \varepsilon_{yy} + \varepsilon_{zz}) + \Xi_u \varepsilon_{zz} \tag{3.12c}$$

Actually, the applied stress is not always along [100], it may be in the direction of [110], [111], and [112], etc. Fortunately, the stress is easily transformed between different coordinates [3.18]. The stress tensors in some cases are listed in Table 3.1.

3.3 Gate Direct Tunneling Current Model

Using both quantum mechanical simulator *TRP* and a modified *WKB* [3.28]-[3.30] approximation for transmission probability, the model for calculating the gate direct tunneling currents across ultra-thin gate oxides of MOS structures is discuss here.

The correction coefficient generator via Eq. (2.5) and (2.12) were incorporated into existing strain quantum simulator in our previous works [3.29]-[3.31]. The resulting subband level in the presence of the uniaxial channel stress σ in the <110> direction can be written with respect to the non-stress conduction-band edge at the

Si/SiO_2 interface [3.3]-[3.6]

$$E'_{\Delta 2,i} = E_{\Delta 2,i} + (\Xi_d + \frac{\Xi_u}{3})(S_{11} + 2S_{12})\sigma + (\frac{\Xi_u}{3})(S_{12} - S_{11})\sigma \tag{3.13a}$$

$$E'_{\Delta 4,i} = E_{\Delta 4,i} + (\Xi_d + \frac{\Xi_u}{3})(S_{11} + 2S_{12})\sigma - (\frac{\Xi_u}{6})(S_{12} - S_{11})\sigma \tag{3.13b}$$

The carrier repopulation under stress can be calculated accordingly:

$$N_{\Delta 2/4,i} = g_{\Delta 2/4}(\frac{m_{d,\Delta 2/4} k_B T}{\pi \hbar^2}) \ln(1 + \exp(\frac{E_F - E'_{\Delta 2/4,i}}{k_B T})) \tag{3.14}$$

Finally, the triangular potential based electron gate direct tunneling current density can be computed:

$$J_e = \sum_i q f_{\Delta 2,i} N_{\Delta 2,i} P_t(E'_{\Delta 2,i}) + \sum_i q f_{\Delta 4,i} N_{\Delta 4,i} P_t(E'_{\Delta 4,i}) \tag{3.15}$$

where f represents the electron impact frequency on the Si/SiO_2 interface and is equal to $(qF_{\Delta 2/4,i}/2)(2m_{z,\Delta 2/4}E_{\Delta 2/4,i})^{-1/2}$; and $P_t(E'_{\Delta 2/4,i})$ is the electron transmission probability across the SiO_2 film. In Fig. 3.3, the energy band diagram of the MOS system under study is schematically shown, where the electron direct tunneling process from the subband level is highlighted. Throughout the work, only five lowest subbands (3 of Δ_2 and 2 of Δ_4) will be adopted to calculate the gate current.

Here, the electron effective mass in the oxide for the parabolic type dispersion relationship was used with $m_{ox} = 0.50\ m_o$, which is equivalent to $m_{ox} = 0.61\ m_o$ for the tunneling electrons in the oxide using the Franz type dispersion relationship [3.32]. The SiO_2/Si interface barrier height in the absence of stress is 3.15 eV. Given the situations that the deformation potential constants are known and the channel stress can be determined by other means, there are four variables in using (3.15) to quantify the gate direct tunneling current: (i) the 2-fold quantization effective mass $m_{z,\Delta 2}$; (ii) the 2-fold 2-D DOS effective mass $m_{d,\Delta 2}$; (iii) the 4-fold quantization effective mass $m_{z,\Delta 4}$; and (iv) the 4-fold 2-D DOS effective mass $m_{d,\Delta 4}$. The DOS effective mass can relate to the mentioned m_l and m_t of the valley: $m_{d,\Delta 2} = (m_{t,\Delta 2//} m_{t,\Delta 2\perp})^{1/2}$ and $\mathrm{m}_{\mathrm{d},\Delta 4} = (m_{l,\Delta 4}\, m_{t,\Delta 4})^{1/2}$, where $m_{t,\Delta 2//}$ and $m_{t,\Delta 2\perp}$ are the in-plane transverse effective mass of Δ_2 in the direction parallel and perpendicular to the stress direction, respectively; and $m_{l,\Delta 4}$ and $m_{t,\Delta 4}$ are the in-plane longitudinal and transverse effective mass of Δ_4, respectively. All the effective masses involved in this work are depicted in Fig. 3.4 in terms of the conduction-band structure in the Brillouin zone. The corresponding nominal values (i.e., in the absence of the stress) are listed in Table 3.2.

3.4 Data Fitting

In Fig. 3.5, the gate current density calculated by *TRP* and that from experiment [3.6] for different gate voltages are shown. Unlike the results from original TRP, our modified TRP provides deviating with the experimental one. Even if we tried other different nominal values for the effective masses in silicon, the deformation potential constants, the effective mass in the oxide, the doping concentration, the gate oxide thickness, etc., a poor fitting like that in Fig. 3.5 still remained.

Obviously, for a general effective mass m, the piezo-effective-mass coefficient π_m must be added:

$$m_z(\sigma) = m_z(0) + \pi_{m,z}\sigma \tag{3.16a}$$

$$m_d(\sigma) = m_d(0) + \pi_{m,d}\sigma \tag{3.16b}$$

Here, a small stress is imposed to make possible the linear approximation that ensures the validity of (3.16). To assess the underlying π_m ($\pi_{m,z\Delta2}$, $\pi_{m,d\Delta2}$, $\pi_{m,z\Delta4}$, and $\pi_{m,d\Delta4}$), the sensitivity analysis was performed during the data fitting. First of all, one of these four π_m factors were alternately selected in applying (3.16), with the remaining three kept at zero. Strikingly, we found that the $\pi_{m,z\Delta4}$ is the primary factor because it can have a strongest effect on the calculated gate current change, as illustrated in Fig. 3.6 for $\pi_{m,z\Delta4}$ of 0.03, 0.05, and 0.07 m_o/GPa. It can be seen from the figure that the fitting can be somewhat improved by simply increasing $\pi_{m,z\Delta4}$. Next, we also found that the $\pi_{m,d\Delta2}$ can serve as the secondary factor in refining the calculated gate current change. This means that both $\pi_{m,z\Delta4}$ and $\pi_{m,d\Delta2}$ are enough in producing the reasonable fitting. Thus, in the subsequent work, we set $\pi_{m,z\Delta2}$ and $\pi_{m,d\Delta4}$ to zero. A set of the $\pi_{m,z\Delta4}$ and $\pi_{m,d\Delta2}$ values was hence extracted from the best fitting, as displayed in Fig. 3.6: (i) $\pi_{m,z\Delta4} = 0.03$ m_o/GPa and $\pi_{m,d\Delta2} = -0.03$ m_o/GPa; (ii) $\pi_{m,z\Delta4} = 0.05$ m_o/GPa and $\pi_{m,d\Delta2} = -0.02$ m_o/GPa; and (iii) $\pi_{m,z\Delta4} = 0.07$ m_o/GPa and $\pi_{m,d\Delta2} = -0.017$ m_o/GPa. Obviously, the increasing $\pi_{m,z\Delta4}$ is accompanied with the less negative $\pi_{m,d\Delta2}$. The piezo-effective-mass coefficient values obtained in the data fitting are listed in Table 3.3.

Here, we give plausible explanations for the assessed $\pi_{m,z\Delta4}$ and $\pi_{m,d\Delta2}$ and particularly the difference in the polarity between the two. Firstly, a positively increased $\pi_{m,z\Delta4}$ will decrease the Δ_4 quantization effective mass (see Eq. (3.16a)) under uniaxial compressive stress, which will in turn increase the Δ_4 level. As a result, due to the repopulation of the valley, more electrons are transferred down to the Δ_2 subband and hence the direct tunneling is reduced. Secondly, a less negative $\pi_{m,d\Delta2}$ will increase the *effective* DOS in Δ_2 (see Eq. (3.16b)) under uniaxial compressive stress. Thus, the increased population in Δ_2 dictates that the gate direct tunneling is reduced. To corroborate this, the additional work was done by decoupling the gate current change into different components according to Eq. (3.15). The results are depicted in Fig. 3.7. From Fig. 3.7, the repopulation is the main factor in affecting the calculated gate current change. Again, here we want to stress that even with only *three* lowest subbands (2 of Δ_2 and 1 of Δ_4) used in the gate current calculation, little change in the listed π_m in Table 3.3 can occur. In this sense, the total number of five lowest subbands remains valid.

3.5 Comparison and Discussion

The published formalisms and/or graphical data in the citations [3.8]-[3.10], [3.12] can furnish the quantified π_m of the longitudinal effective mass m_l and the transverse effective mass m_t for 2- and 4-fold valleys, except the 4-fold quantization one. Then, it is a straightforward task to compute the corresponding DOS π_m:

$$\pi_{md,\Delta 2} = \frac{1}{2}\left(\frac{\pi_{mt,\Delta 2\parallel}}{m_{t,\Delta 2\parallel}} + \frac{\pi_{mt,\Delta 2\perp}}{m_{t,\Delta 2\perp}}\right)\sqrt{m_{t,\Delta 2\parallel} m_{t,\Delta 2\perp}} \tag{3.17a}$$

$$\pi_{md,\Delta 4} = \frac{1}{2}\left(\frac{\pi_{ml,\Delta 4}}{m_{l,\Delta 4}} + \frac{\pi_{mt,\Delta 4}}{m_{t,\Delta 4}}\right)\sqrt{m_{l,\Delta 4} m_{t,\Delta 4}} \tag{3.17b}$$

The results are added to Table 3.3. Although the strain dependence of the 4-fold quantization effective mass was not provided in the studies [3.8]-[3.10], [3.12] and hence it is impossible to directly examine the validity of the extracted $\pi_{m,z\Delta 4}$ in this work, some comparisons can be made by means of Table 3.3. Firstly, the published values of $\pi_{m,z\Delta 2}$ and $\pi_{m,d\Delta 4}$ [3.8]-[3.10], [3.12] are very small in magnitude, which support the use of approximately zero $\pi_{m,z\Delta 2}$ and $\pi_{m,d\Delta 4}$ in the above data fitting.

Indeed, we found that little change in the assessed $\pi_{m,z\Delta4}$ and $\pi_{m,d\Delta2}$ can be observed if the literature values of $\pi_{m,z\Delta2}$ and $\pi_{m,d\Delta4}$ [3.8]-[3.10], [3.12] are instead used. Secondly, the assessed $\pi_{m,d\Delta2}$ is negative, quite close to that (-0.0095 m_o/GPa) obtained from the mobility measurement [3.12]. Finally, Table 3.3 provides the maximum π_m in magnitude available to date: 0.048 m_o/GPa [3.12]. In comparison, the assessed $\pi_{m,z\Delta4}$ ranging from 0.03 to 0.07 m_o/GPa in this work is quantitatively reasonable.

To strengthen the applicability of the assessed π_m, we further cite the previous work [3.7] in terms of the measured electron gate direct tunneling current change due to the process induced uniaxial compressive channel stress as shown in Fig. 3.8. In addition, Fig. 3.8 depicted the calculated results using the assessed π_m, exhibiting a large deviation from the data points. This condition is expected, because in the manufacturing process with the build-in stressors, the devices may encounter additional effects such as stress-induced dopant redistribution [3.33] and the thermal oxidation change [3.31], which essentially are not present in case of the external stress [3.6]. Here, we attribute this significant difference to the decrease in the gate oxide thickness of the device undergoing the process-induced uniaxial compressive stress. The physical interpretations are that the oxide growth rate will be retarded under the influence of the compressive stress in the manufacturing process. In this sense, one can define a piezo-oxide-thickness coefficient π_{tox}:

$$t_{ox}(\sigma) = t_{ox}(0) + \pi_{tox}\sigma \qquad (3.18)$$

The data were again fitted, leading to π_{ox} of 0.012 nm/GPa. The quality of the fitting, as demonstrated in Fig. 3.9, is fairly good. In addition, the extracted value is reasonable compared to that (~0.02 nm/GPa) of the p-channel counterparts on the same test wafer [3.31].

Therefore, it is claimed that owing to the presence of the strong evidence in terms of the literature π_m values [3.8]-[3.10], [3.12] and the oxide thickness retardation [3.31], the electron gate direct tunneling current in uniaxially compressive strained device is judged to be the sensitive detector of π_m. Finally, we want to stress that the fit to process-induced data [3.7] works well [see Fig. 3.9], whereas there is quite a large discrepancy in the fit to external stress data [3.6] (Fig. 3.6), particularly at lower gate voltage. To address this issue, we suggest that the stress distribution in the quoted device under the external stress [3.6] is nonuniform. This argument can be drawn from the calculated results in Fig. 3.6, which clearly point out that the stress effect of the gate current change is enhanced with decreasing gate voltage. Oppositely, this effect becomes weak for larger gate voltage. Thus, the gate current change due to a local stress variation may be amplified if the gate voltage applied is as low as 0.5 V. Relatively, for higher gate voltage at 1 V, the local stress variation accordingly produces little change in gate current. Fairly good agreement over the stress in Fig. 3.6 for gate voltage of 1 V supports this approach. In a sense, the gate voltage factor in the proposed gate current method can be helpful in clarifying the responsible mechanisms.

3.6 Conclusion

A new correction-coefficient generator has systematically been created to compensate for the subband levels for the use of the triangular potential approximation. Then, with the known deformation potential constants and uniaxial compressive channel stress as inputs, the strain quantum simulation dedicated to the gate direct tunneling current has rigorously been performed. Reasonable reproduction of the measured gate direct tunneling current has been achieved, leading to the underlying electron piezo-effective-mass coefficients. The confirmative evidence has been presented in terms of the published piezo-effective-mass coefficient and oxide thickness retardation values. The ability of the electron gate direct tunneling current in uniaxially compressive strained device as a sensitive detector of the electron piezo-effective-mass has been verified.

References

[3.1] F. Stern, “Self-consistent results for n-type Si inversion layers,” *Phys. Rev. B*, vol. 5, no.12, pp.4891-4899, Jun. 1972.

[3.2] M. V. Fischetti and S. E. Laux, “Band structure, deformation potentials, and carrier mobility in strained Si, Ge, and SiGe alloys,” *J. Appl. Phys.*, vol. 80, no. 4, pp. 2234–2252, Aug. 1996.

[3.3] C. Herring and E. Vogt, “Transport and deformation-potential theory for many-valley semiconductors with anisotropic scattering,” *Phys. Rev.*, vol. 101, no. 3, pp. 944–961, Feb. 1956.

[3.4] I. Balslev, “Influence of uniaxial stress on the indirect absorption edge in silicon and germanium,” *Phys. Rev.*, vol. 143, no. 2, pp. 636–647, Mar. 1966.

[3.5] C. G. Van de Walle and R. M. Martin, “Theoretical calculations of heterojunction discontinuities in the Si/Ge system,” *Phys. Rev. B, Condens. Matter*, vol. 34, no. 8, pp. 5621–5634, Oct. 1986.

[3.6] J. S. Lim, X. Yang, T. Nishida, and S. E. Thompson, “Measurement of conduction band deformation potential constants using gate direct tunneling current in *n*-type metal oxide semiconductor field effect transistors under mechanical stress,” *Appl. Phys. Lett.*, vol. 89, no. 7, pp. 073509-1-073509-3, Aug. 2006.

[3.7] C. Y. Hsieh and M. J. Chen, “Measurement of channel stress using gate direct tunneling current in uniaxially stressed nMOSFETs,” *IEEE Electron Device Lett.*, vol. 28, no. 9, pp. 818-820, Sept. 2007.

[3.8] K. Uchida, T. Krishnamohan, K. C. Saraswat, and Y. Nishi, “Physical mechanisms of electron mobility enhancement in uniaxial stressed MOSFETs and impact of uniaxial stress engineering in ballistic regime,” in *IEDM Tech.*

Dig., 2005, pp. 129–132.

[3.9] S. Dhar, E. Ungersböck, H. Kosina, T. Grasser, and S. Selberherr, “Electron mobility model for <110> stressed silicon including strain-dependent mass,” *IEEE Trans. Nanotechnology*, vol. 6, no. 1, pp. 97-100, Jan. 2007.

[3.10] E. Ungersböeck, S. Dhar, G. Karlowatz, V. Sverdlov, H. Kosina, and S. Selberherr, “The effects of general strain on the band structure and electron mobility of silicon,” *IEEE Trans. Electron Devices*, vol. 54, no. 9, pp. 2183-2190, Sep. 2007.

[3.11] K. Uchida, A. Kinoshita, and M. Saitoh, “Carrier transport in (110) nMOSFETs: subband structure, non-parabolicity, mobility characteristics, and uniaxial stress engineering,” in *IEDM Tech. Dig.*, 2006, pp. 1019–1021.

[3.12] F. Rochette, M. Cassē, M. Mouis, G. Reimbold, D. Blachier, C. Leroux, B. Guillaumot, and F. Boulanger, “Experimental evidence and extraction of the electron mass variation in [110] uniaxially strained MOSFETs,” *Solid State Electronics*, vol. 51, no. 11-12, pp. 1458-1465, Nov.-Dec. 2007.

[3.13] S. Takagi, T. Mizuno, T. Tezuka, N. Sugiyama, T. Numata, K. Usuda, Y. Moriyama, S. Nakaharai, J. Koga, A. Tanabe, N. Hirashita, and T. Maeda, “Channel structure design, fabrication and carrier transport properties of strained-Si/SiGe-on-insulator (strained-SOI) MOSFETs,” in *IEDM Tech .Dig.*, 2003, pp. 57-60.

[3.14] W. Zhao, A. Seabaugh, V. Adams, D. Jovanovic, and B. Winstead, “Opposing dependence of the electron and hole gate currents in SOI MOSFETs under uniaxial strain,” *IEEE Electron Device Lett.*, vol. 26, no. 6, pp. 410-412, Jun. 2005.

[3.15] S. E. Thompson, G. Sun, Y. S. Choi, and T. Nishida, “Uniaxial-process-induced strained-Si: extending the CMOS roadmap," *IEEE Trans. Electron Devices*, vol. 53, no. 5, pp. 1010–1020, May 2006.

[3.16] T. Hoshii, S. Sugahara, and S. Takagi, "Effect of tensile strain on gate current of strained-Si n-channel metal-oxide-semiconductor field-effect transistors," *Jap. J. Appl. Phys.*, vol. 46, no. 4B, pp. 2122–2126, Apr. 2007.

[3.17] M. Saitoh, A. Kaneko, K. Okano, T. Kinoshita, S. Inaba, Y. Toyoshima, and K. Uchida, "Three-dimensional stress engineering in FinFETs for mobility/on-current enhancement and gate current reduction," in *VLSI Symp. Tech. Dig.*, Jun. 2008, pp. 18-19.

[3.18] Y. Huang, "Material mechanics know why," *Tingmao Publish Company*, 2004.

[3.19] H. A. Rueda, "Modeling of mechanical stress in silicon isolation technology and its influence on device characteristics," dissertation of degree of doctor of philosophy, university of *Florida*,1999.

[3.20] Fusahito Yoshida, "Fundamentals of elastic plastic mechanics," *KYORITSU SHUPPAN Co., Ltd.*, 1997.

[3.21] Y. Kanda, "A graphical representation of the piezoresistance coefficients in silicon," *IEEE Trans. Electron Devices*, vol. 29, no. 1, pp. 64–70, Jan. 1982.

[3.22] Y. Kanda, "Effect of stress on germanium and silicon p-n junctions," *Jap. J. Appl. Phys.*, vol. 6, no. 4, pp. 475–486, Apr. 1967.

[3.23] MEMS & Nanotechnology Exchange (http://www.memsnet.org/material/)

[3.24] Almaz Optics, Inc. (http://www.almazoptics.com/material.htm)

[3.25] Korth Kristalle Gmbh (http://www.korth.de)

[3.26] J. S. Lim, S. E. Thompson, and J. G. Fossum, "Comparison of threshold-voltage shifts for uniaxial and biaxial tensile-stressed n-MOSFETs," *IEEE Electron Device Lett.*, vol. 25, pp. 731-733, Nov. 2004.

[3.27] Y. Sun, S. E. Thompson, and T. Nishida, “Physics of strain effects in semiconductors and metal-oxide-semiconductor field-effect transistors,” *J. Appl. Phys.*, vol. 101, no. 10, pp. 104503-1-104503-22, May 2007.

[3.28] N. Yang, W. K. Henson, J. R. Hauser, and J. J. Wortman, “Modeling study of ultrathin gate oxides using direct tunneling current and capacitance-voltage measurements in MOS devices,” *IEEE Trans. Electron Devices*, vol. 46, no. 7, pp. 1464–1471, Jul. 1999.

[3.29] K. N. Yang, H. T. Huang, M. C. Chang, C. M. Chu, Y. S. Chen, M. J. Chen, Y. M. Lin, M. C. Yu, S. M. Jang, D. C. H. Yu, and M. S. Liang, “A physical model for hole direct tunneling current in p^+ poly-gate pMOSFETs with ultrathin gate oxides,” *IEEE Trans. Electron Devices*, vol. 47, no. 11, pp. 2161–2166, Nov. 2000.

[3.30] Y. T. Hou, M. F. Li, Y. Jin, and W. H. Lai, “Direct tunneling hole currents through ultrathin gate oxides in metal-oxide-semiconductor devices,” *J. Appl. Phys.*, vol. 91, no. 1, pp. 258–264, Jan. 2002.

[3.31] C. Y. Hsu, C. C. Lee, Y. T. Lin, C. Y. Hsieh, and M. J. Chen,” Enhanced hole gate direct tunneling current in process-induced uniaxial compressive stress p-MOSFETs,” *IEEE Trans. on Electron Devices*, vol. 56, no. 8, pp. 1667-1673, Aug. 2009.

[3.32] Z. A. Weinberg, “On tunneling in metal-oxide-silicon structures,” *J. Appl. Phys.*, vol. 53, no. 7, pp. 5052–5056, Jul. 1982.

[3.33] Y. M. Sheu, S. J. Yang, C. C. Wang, C. S. Chang, L. P. Huang, T. Y. Huang, M. J. Chen, and C. H. Diaz, “Modeling mechanical stress effect on dopant diffusion in scaled MOSFETs,” *IEEE Trans. on Electron Devices*, vol. 52, no. 1, pp. 30-38, Jan. 2005.

Table 3.1 The stress tensor for uniaxial stress along [110], [1-10], [001], [111], and [11-2] direction.

	[110]	[1-10]	[001]	[111]	[11-2]
Stress tensor[a] (x σ[b])	$\begin{bmatrix} \frac{1}{2} \\ \frac{1}{2} \\ 0 \\ 0 \\ 0 \\ \frac{1}{2} \end{bmatrix}$	$\begin{bmatrix} \frac{1}{2} \\ \frac{1}{2} \\ 0 \\ 0 \\ 0 \\ -\frac{1}{2} \end{bmatrix}$	$\begin{bmatrix} 0 \\ 0 \\ 1 \\ 0 \\ 0 \\ 0 \end{bmatrix}$	$\begin{bmatrix} \frac{1}{3} \\ \frac{1}{3} \\ \frac{1}{3} \\ \frac{1}{3} \\ \frac{1}{3} \\ \frac{1}{3} \end{bmatrix}$	$\begin{bmatrix} \frac{1}{6} \\ \frac{1}{6} \\ \frac{2}{3} \\ -\frac{1}{3} \\ -\frac{1}{3} \\ \frac{1}{6} \end{bmatrix}$

a: The form of stress tensor is defined by Eq. (3.2).

b: σ indicates the stress applied along each direction.

Table 3.2 The nominal values of the electron effective masses in the absence of the mechanical stress in [3.8]-[3.10], [3.12].

	[3.8]	[3.9]	[3.10]	[3.12]	This work
$\mathbf{m}_{z,\Delta 2}$		**0.918**	**0.916**		**0.916**
$\mathbf{m}_{t,\Delta 2 /\!/}$	**0.2**	**0.196**	**0.194**		**0.19**
$\mathbf{m}_{t,\Delta 2 \perp}$	**0.2**	**0.196**	**0.194**		**0.19**
$\mathbf{m}_{d,\Delta 2}$	**0.2**	**0.196**	**0.194**		**0.19**
$\mathbf{m}_{z,\Delta 4}$					**0.19**
$\mathbf{m}_{l,\Delta 4}$	**0.89**				**0. 916**
$\mathbf{m}_{t,\Delta 4}$	**0.2**				**0.19**
$\mathbf{m}_{d,\Delta 4}$	**0.42**				**0.417**

Units: m_0/GPa.

Deleted grid: No mentioned.

Table 3.3 Comparison of the electron piezo-effective-mass coefficients from the band-structure calculation and mobility measurement [3.8]-[3.10], [3.12] with those obtained in this work. The mechanical stress is applied along the <110> direction on (001) silicon surface.

	[3.8] [compressive]	**[3.8] [tensile]**	**[3.9] [tensile]**	**[3.10] [tensile]**	**[3.12] [tensile]**	**This Work [compressive]**
$\pi_{m,t\Delta 2 /\!/}$	**$-0.014^{\#}$**	**$-0.012^{\#}$**	**-0.016**	**$-0.012^{\#}$**	**-0.048**	
$\pi_{m,t\Delta 2 \perp}$	**$0.013^{\#}$**	**$0.014^{\#}$**	**0.029**	**$0.013^{\#}$**	**0.029**	
$\pi_{m,z\Delta 2}$			**$0.0071^{\#}$**	**$0.002^{\#}$**		**~ 0**
$\pi_{m,d\Delta 2}$	**0.0005**	**0.001**	**0.0065**	**0.0005**	**-0.0095**	**-0.03 ~ -0.017**
$\pi_{m,l\Delta 4}$	**0.0026**	**0.0024**				
$\pi_{m,t\Delta 4}$	**0.001**	**0.001**				
$\pi_{m,z\Delta 4}$						**0.03 ~ 0.07**
$\pi_{m,d\Delta 4}$	**0.0017**	**0.0016**				**~ 0**

#: Linear approximation over a range of <110> uniaxial stress σ on (001) substrate from 0 to 300 or -300 MPa.

Units: m_0/GPa.

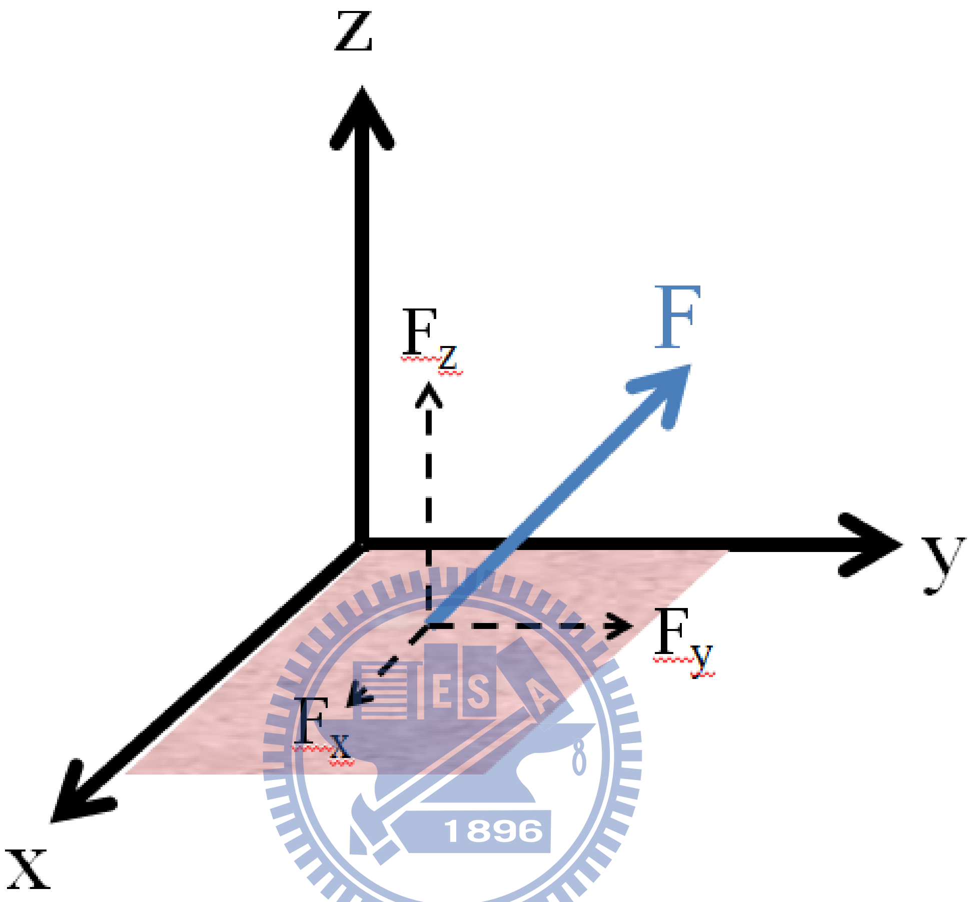

Fig. 3.1 Schematic of an arbitrary force *F* acting on a surface, along with the resolved components: F_x and F_y, which are the source of shear stress, and F_z, which is the source of normal stress.

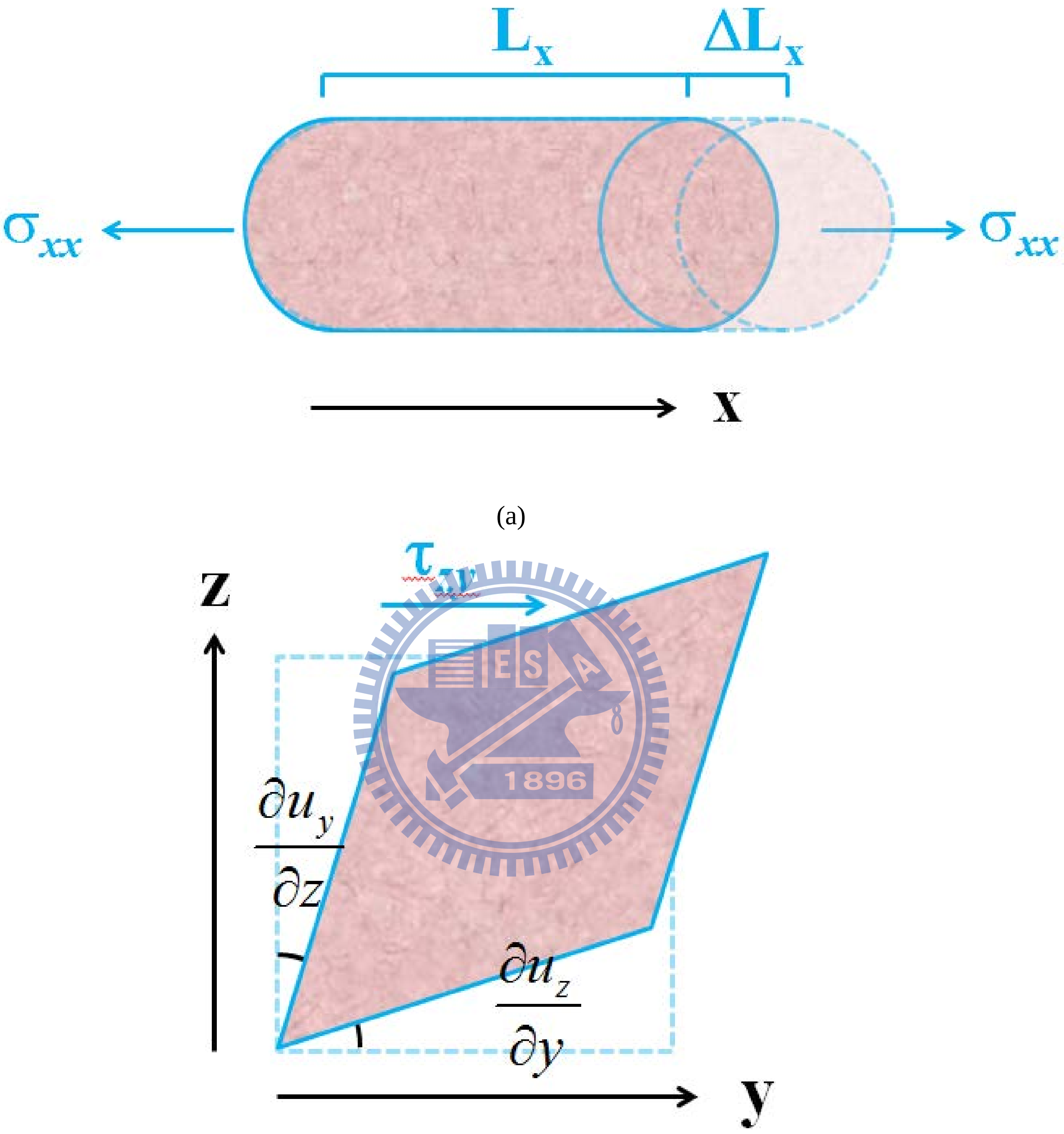

(a)

(b)

Fig. 3.2 (a) Schematic of deformation of a body applied to normal stress along x-axis; (b) Schematic of deformation of a body applied to pure shear stress along x-axis.

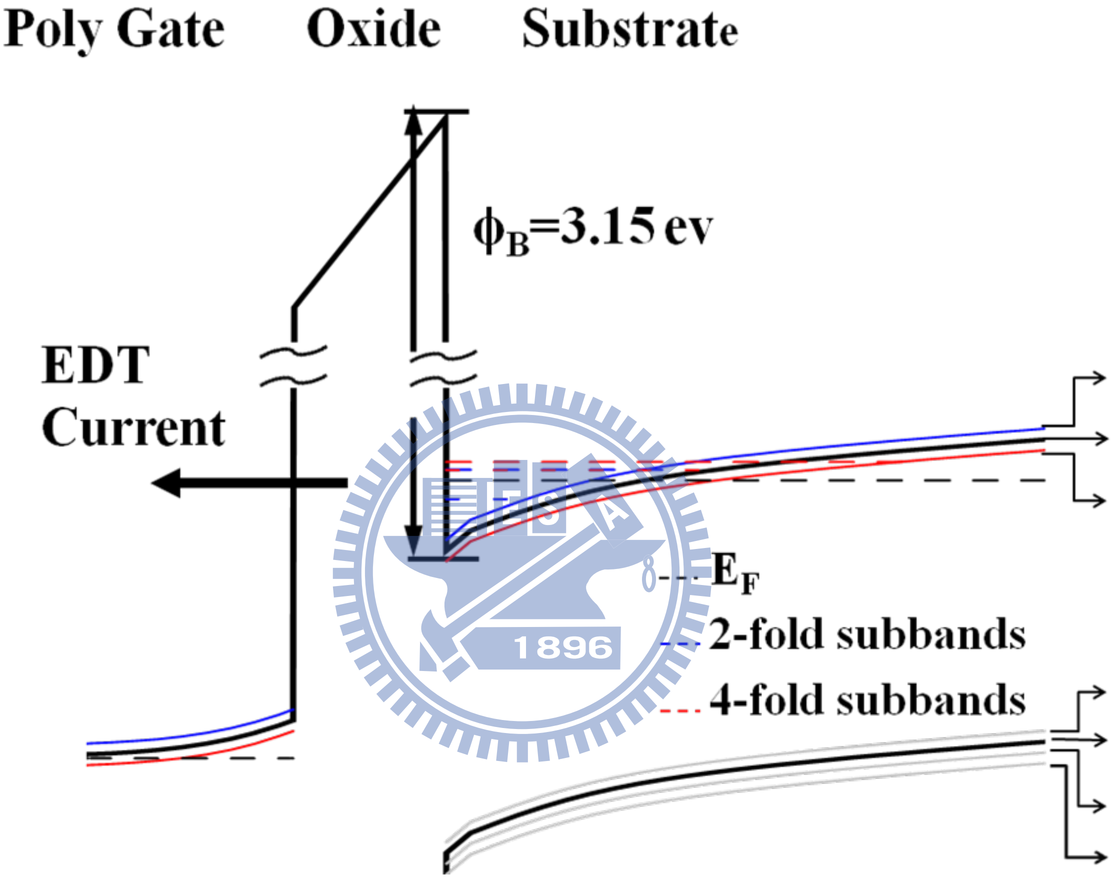

Fig. 3.3 The schematic energy-band diagram of the n+ polysilicon/SiO_2/p-Si MOS system under uniaxial compressive stress along <110> on (001) substrate. The black-solid lines represent the conduction and valence band edge without the stress. The blue- and green-solid lines represent the stress induced conduction band splits. The electron direct tunneling current (EDT) from the subband levels is also shown.

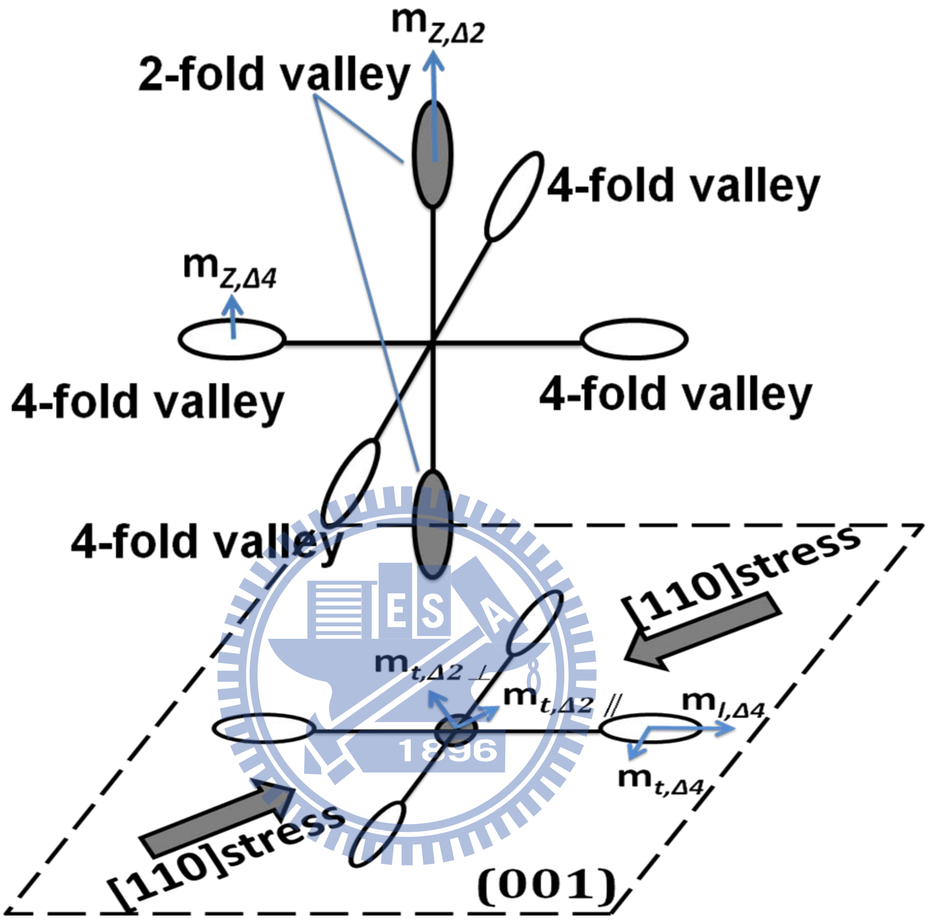

Fig. 3.4 The schematic silicon conduction-band structure in terms of six constant-energy surfaces in the Brillouin zone. The electron effective masses in the presence of a uniaxial compressive stress are also labeled.

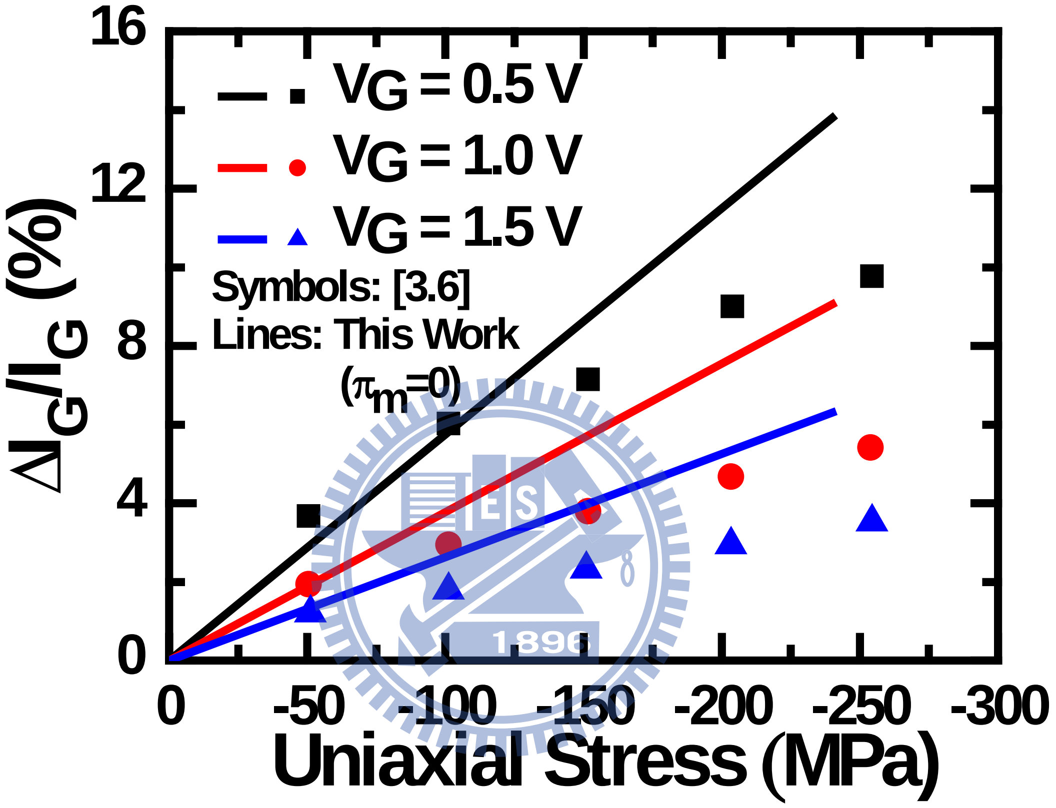

Fig. 3.5 Comparisons of the measured (symbols) gate current change due to the external uniaxially compressive stress [3.6] with the calculated (lines) ones obtained using the nominal values in Table 3.2 for the electron effective masses. The process parameters used are $N_{sub} = 10^{17}$ cm^{-3}, tox = 1.3 nm, and $N_{ploy} = 10^{20}$ cm^{-3}. Poor fitting is encountered if the piezo-effective-mass coefficients are not included.

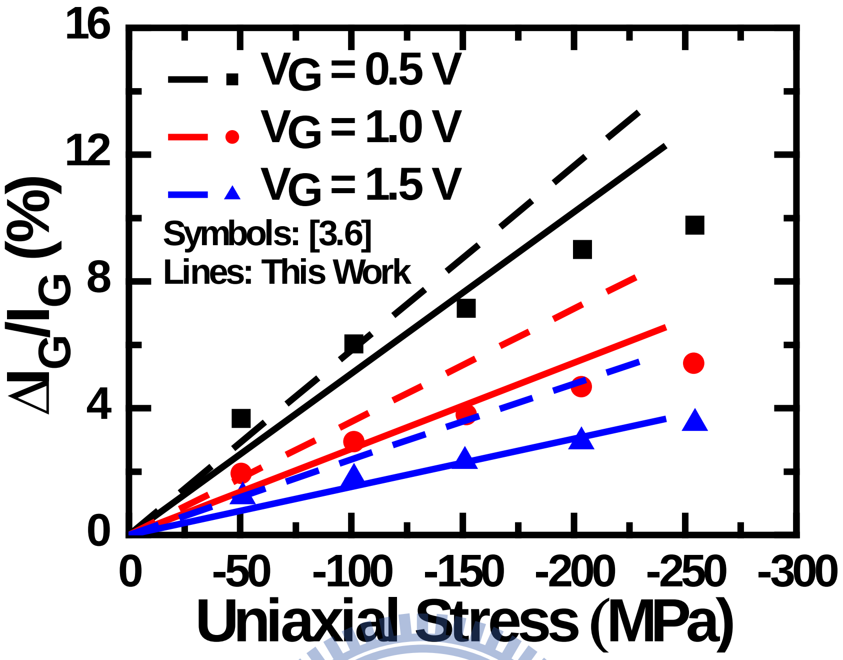

16
12
8
4
0
$\Delta I_G/I_G$ (%)
V_G = 0.5 V
V_G = 1.0 V
V_G = 1.5 V
Symbols: [3.6]
Lines: This Work
0
-50
-100
-150
-200
-250
-300
Uniaxial Stress (MPa)

(a)

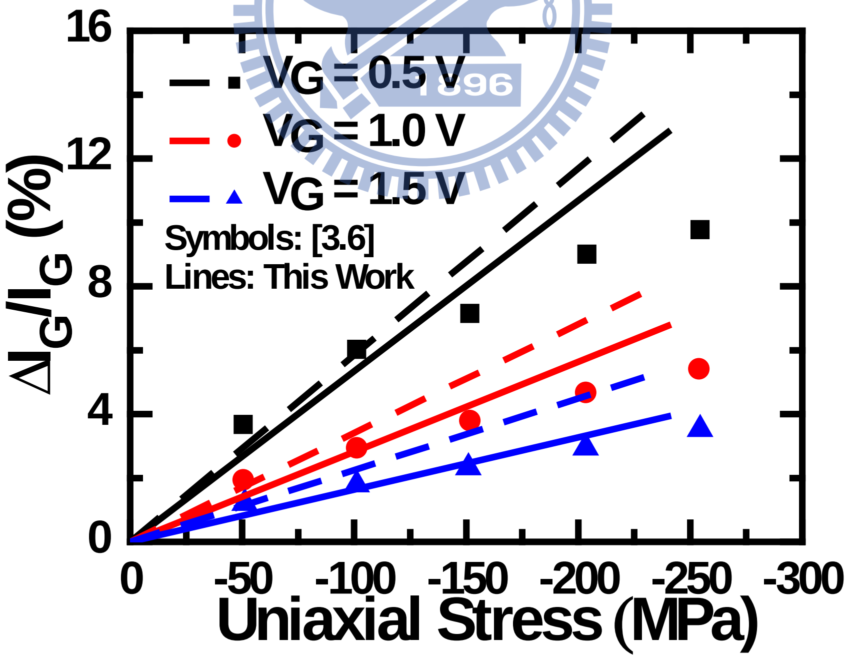

16
12
8
4
0
$\Delta I_G/I_G$ (%)
V_G = 0.5 V
V_G = 1.0 V
V_G = 1.5 V
Symbols: [3.6]
Lines: This Work
0
-50
-100
-150
-200
-250
-300
Uniaxial Stress (MPa)

(b)

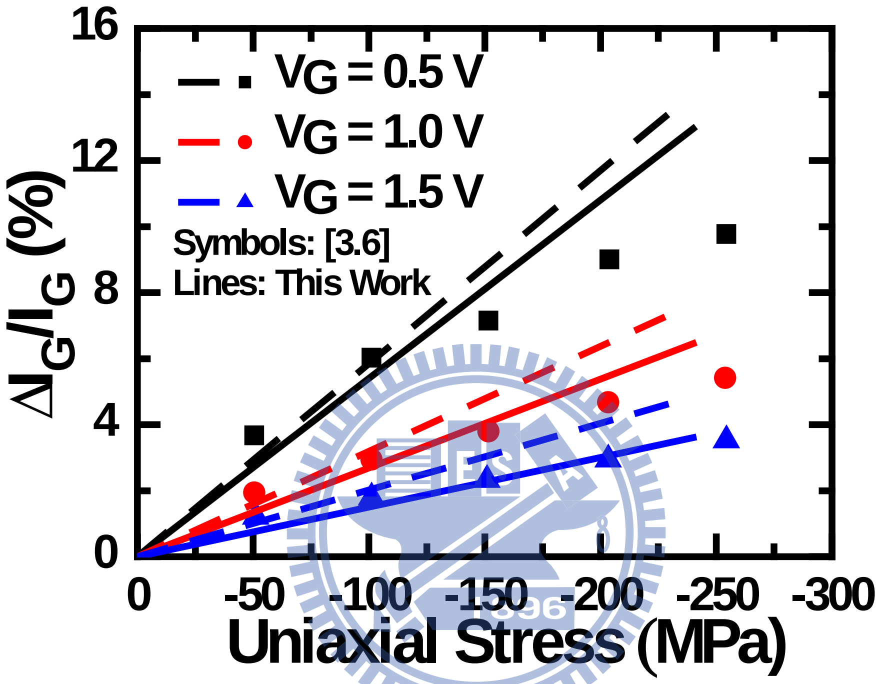

(c)

Fig. 3.6 Comparison of the data (symbols) [3.6] with the calculated results (lines) for (a) $\pi_{m,z\Delta4}$ = 0.03 m_0/GPa (dash lines); and $\pi_{m,z\Delta4}$ = 0.03 m_0/GPa and $\pi_{m,d\Delta2}$ = -0.03 m_0/GPa (solid lines); (b) $\pi_{m,z\Delta4}$ = 0.05 m_0/GPa (dash lines); and $\pi_{m,d\Delta4}$ = 0.05 m_0/GPa and $\pi_{m,d\Delta2}$ = -0.02 m_0/GPa (solid lines); and (c) $\pi_{m,z\Delta4}$ = 0.07 m_0/GPa (dash lines); and $\pi_{m,d\Delta4}$ = 0.07 m_0/GPa and $\pi_{m,d\Delta2}$ = -0.017 m_0/GPa (solid lines). $\pi_{m,z\Delta2}$ and $\pi_{m,d\Delta4}$ both are zero.

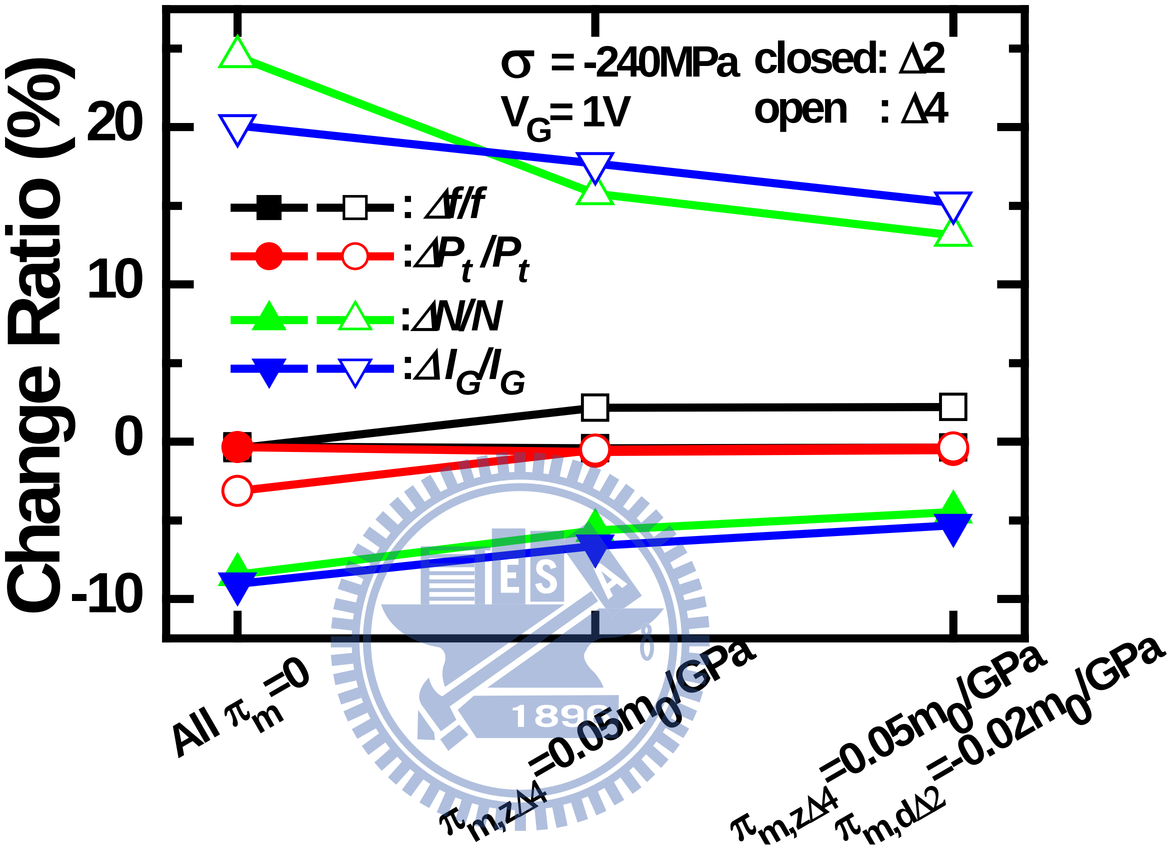

Fig. 3.7 The calculated gate current change ratio and its decoupling into different components: the impact frequency $f_{\Delta 2/4}$, the transmission probability $P_{t,\Delta 2/4}$, and the electron density $N_{\Delta 2/4}$. One can see that the repopulation of the valley is the main factor responsible for the gate current change.

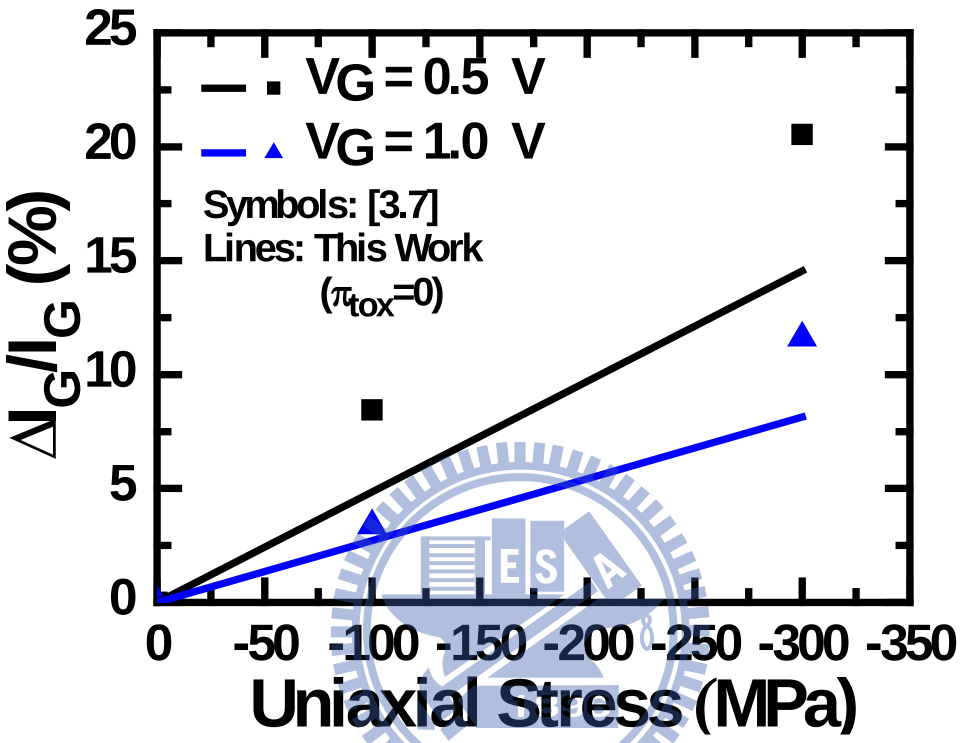

Fig. 3.8 Comparisons of the measured (symbols) [3.7] and calculated (lines) gate current change due to the process induced compressive stress in the <110> direction. Except the piezo-effective-mass coefficients used correspond to Fig. 3.6(c): $\pi_{m,z\Delta 4}$ = 0.07 m_0/GPa, $\pi_{m,d\Delta 2}$ = -0.017 m_0/GPa, $\pi_{m,z\Delta 2}$ = 0, and $\pi_{m,d\Delta 4}$ = 0.

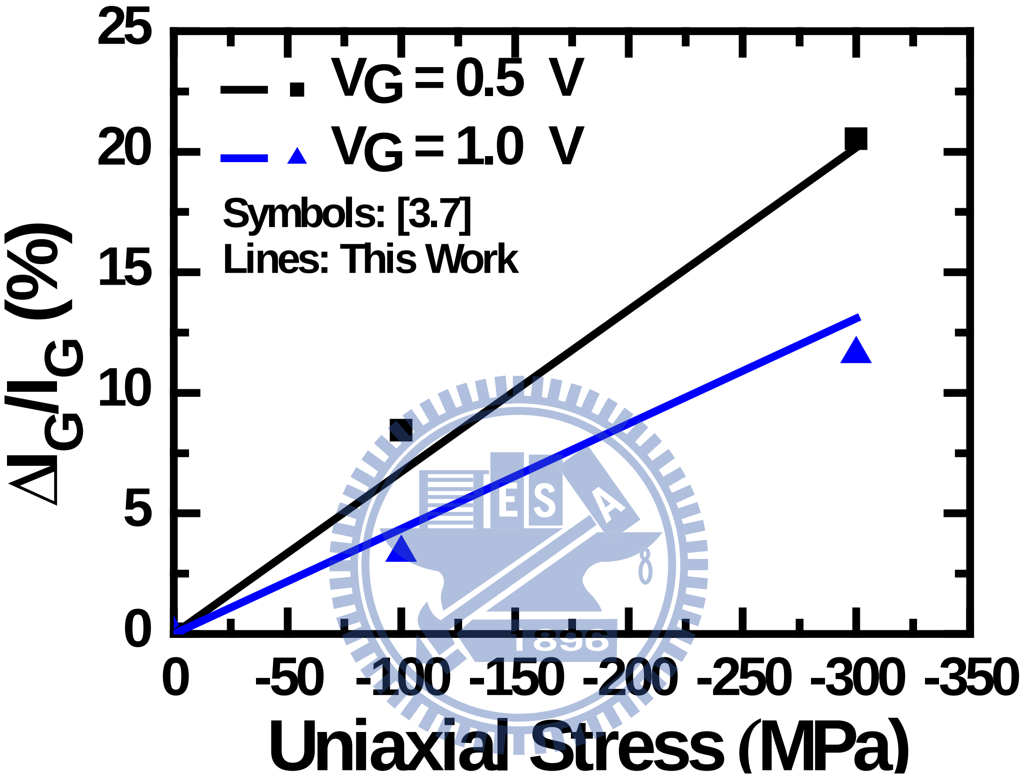

Fig. 3.9 Comparisons of the measured (symbols) [3.7] and calculated (lines) gate current change due to the process induced compressive stress in the <110> direction. Except the piezo-effective-mass coefficients used correspond to Fig. 3.6(c): $\pi_{m,z\Delta 4}$ = 0.07 m_0/GPa, $\pi_{m,d\Delta 2}$ = -0.017 m_0/GPa, $\pi_{m,z\Delta 2}$ = 0, and $\pi_{m,d\Delta 4}$ = 0. π_{tox} = 0.012 nm/GPa is used here.

Chapter 4
Electron Mobility Model

4.1 Introduction

As mentioned before, the valley shift in energy [4.1]-[4.4] in terms of the deformation potential can change gate direct tunneling current. Mobility is other device parameter which is sensitive to strain. Furthermore, the change in effective mass in band structure warping under strain can alter the mobility. To address the mobility mechanisms, a mobility is needed. To make it possible, a fully self-consistent Schrődinger and Poisson equations solver for n-channel MOSFETs, named "*NEP*" is presented. With the aid of *NEP*, the 2-D electron mobility can straightforwardly be calculated [4.5]-[4.6].

4.2 Introduction of *NEP*

The structure of fully Schrődinger and Poisson self-consistent solver, named *NEP*, is introduced in this section. The energy band diagram is shown in Fig. 4.1. We separated the band diagram of silicon substrate along out-of-plane z direction into two parts: one is the width of the surface quantum confinement region $W_{quantum}$ and another is the width of the classical region $W_{classical}$:

$$W_{quantum} = \frac{1}{2}\sqrt{\frac{2\varepsilon_{si}V_s}{qN_{sub}}} \tag{4.1a}$$

$$W_{classical} = \sqrt{\frac{2\varepsilon_{si} V_s}{qN_{sub}}} \tag{4.1b}$$

In the quantum region, the carriers are confined in this thin region, 300 meshes are used to ensure simulation accuracy.

Fig. 4.2 illustrates the flow chart in *NEP*. At the beginning, we give a V_s as the input, an initial potential profile seen by electron *V(z)* evolves from Poisson equation with two boundary condition: $V_{(z=0)} = -V_s$ and $V_{(z=\mathrm{bulk})} = 0$. Within the quantum region, energy levels *E* and corresponding wave-function ψ are carried out by 1D Schrődinger equation along with *V*(*z*). The corresponding formula is written as

$$H\psi(z) = -\frac{\hbar^2}{2m}\nabla^2\psi(z) + qV(z)\psi(z) = E\psi(z) \tag{4.2}$$

According to Eq. (4.2), the Schrödinger equation can be rewritten as a general differential equation by the finite element method:

$$-\frac{\hbar^2}{2m}\left[\frac{\psi(z_{i-1}) - 2\psi(z_i) + \psi(z_{i+1})}{\Delta z^2}\right] + qV(z_i)\psi(z_i) = E\psi(z_i) \tag{4.3}$$

H can be transferred to a square matrix with Eq. (4.3). Three hundreds of eigenvalues (*E* in Eq. (4.2)) and eigenvectors (ψ in Eq. (4.2)) are solved. With Eq. (2.8), carrier repopulation for each subband can be calculated. Now the distribution of three-dimensional carriers (both electrons and holes) density is also known:

$$n(z) = \sum_{j,i} g_j \left(\frac{m_{d,j} k_B T}{\pi\hbar^2}\right) \ln\left(1 + \mathrm{e}^{\frac{E_F - E_{j,i}}{k_B T}}\right) \times \left|\psi_{j,i}\right|^2 \tag{4.4a}$$

$$p(z)=\sum_{k,i} g_k\left(\frac{m_{d,k}k_BT}{\pi\hbar^2}\right)\ln\left(1+\mathrm{e}^{\frac{E_{k,i}-E_F}{k_BT}}\right)\times\left|\psi_{k,i}\right|^2 \tag{4.4b}$$

where j includes each of 2-fold valley and 4-fold valley, k is including heavy hole, light hole and spilt-off hole, and $E_{j,i}$ and $E_{k,i}$ are the i^{th} electron and hole energy levels respectively. The corresponding wave-functions $\psi_{j,i}$ and $\psi_{k,i}$ are all normalized. In the classical region, the carrier density is given by:

$$n(z)=n_0\exp\left(\frac{-q(V(bulk)-V(z))}{k_BT}\right) \tag{4.5a}$$

$$p(z)=p_0\exp\left(\frac{q(V(bulk)-V(z))}{k_BT}\right) \tag{4.5b}$$

where p_0 and n_0 are the carrier concentration under the thermal equilibrium. Substituting the above concentration into the 1D Poisson equations, the formula is given by:

$$\frac{d^2V(z)}{dz}=\frac{-q[-N_a^+-n(z)+p(z)]}{\varepsilon_{si}} \tag{4.6}$$

where $N_a^+(z)$ is the ionized accepter density. Eventually, we can obtain a new potential $V(z)$ to satisfy Eq. (4.6) by Newton's method. Now, Eq. (4.2) and Eq. (4.6) are used iteratively until the new potential changes little.

Total 2-D charge density in inversion layer N_{inv}, the average inversion layer thickness Z_{av}, the flat band voltage V_{fb}, the poly/metal gate voltage V_{poly} / V_{metal}, oxide voltage V_{ox} can all be produced out:

$$N_{inv}=\sum_{j,i}N_{j,i} \tag{4.7}$$

$$Z_{av} = \sum_{j,i} [\frac{N_{j,i}}{N_{inv}} \int_{0}^{bulk} z \left| \psi_{j,i}(z) \right|^2 dz] \qquad (4.8)$$

$$V_{fb} = -k_B T \ln(\frac{N_{poly} N_{sub}}{n_i^2}) \qquad (4.9)$$

$$V_{poly} = \frac{\varepsilon_{si} F_s^2}{2qN_{poly}} \qquad (4.10a)$$

$$V_{metal} = 0 \qquad (4.10b)$$

$$V_{ox} = \frac{t_{ox} \varepsilon_{si} F_s}{\varepsilon_{ox}} \qquad (4.11)$$

where $N_{j,i}$ is the 2-D density of carrier at i^{st} subband of j-valley. Eventually, the total gate voltage can be expressed as:

$$V_g = V_{poly/metal} + V_{ox} + V_s + V_{fb} \qquad (4.12)$$

The subband level in two cases calculated by *NEP* and *Schred* [4.7] are put to together in Fig. 4.3. The satisfying result is presented by the *NEP*.

4.3 Electron Mobility Model

4.3.1 Introduction

In this section, mobility calculation is introduced by three components: scattering by phonons (ph), scattering by surface roughness (sr), and scattering by ionized doping impurity (imp). Using the subband energy and the wave-function provided by *NEP*, the mobility is calculated under the momentum relaxation time approximation. The total mobility including phonon-limited and surface-roughness-limited ones are a universal mobility versus with the effective electric field E_{eff} [4.8]-[4.10]:

$$E_{eff} = \frac{\int E(z)n(z)dz}{\int n(z)dz} \tag{4.13a}$$

which can be fortunately simplified to:

$$E_{eff} = \frac{q(\eta N_{inv} + N_{dep})}{\varepsilon_{Si}} \tag{4.13b}$$

where η is taken to 0.5 for electron [4.11]. Fig. 4.4 shows the comparison between Eq. (4.13a) and (4.13b).

4.3.2 Phonon-Limited Mobility

It is well known that the thermal vibrations would deform the crystal potential, perturbing the dipole moment between atoms, and resulting in the degradation of inversion layer mobility. There are two types of phonons (acoustic phonons and optical phonons), and two types of scattering mechanisms, intravalley scattering and intervalley scattering [4.12]-[4.15]. The schematic diagram of each scattering process and its transition path between the valleys is showed in Fig. 4.5.

Intravalley phonon scattering is allowed for acoustic phonons but forbidden for optical phonons by the selection rules for the electron-phonon interaction in bulk Si [4.13], [4.15]. The momentum-relaxation rate from the u^{th} subband to the v^{th} subband,

$\tau_{ac,}{}^{uv}$, is expressed:

$$\frac{1}{\tau^{u,v}_{\mathrm{int}ra(\Delta 2/4)}(E)} = \frac{m_{d,\Delta 2/4} D_{ac}^2 k_B T}{\hbar^3 \rho s_l^2} \frac{1}{W_{u,v(\Delta 2/4)}} \tag{4.14a}$$

$$W_{u,v(\Delta 2/4)} = (\int \psi^2_{(\Delta 2/4),u}(z) \psi^2_{(\Delta 2/4),v}(z) dz)^{-1} \tag{4.14b}$$

where D_{ac} denotes the deformation potential due to acoustic phonons, ρ is the crystal density, s_l is the sound velocity. Considering the possible energy in quantum region, the total scattering rate of an electron with its energy E and occupied in u_{th} subband is determined by summing up $\tau^{u,v}_{\mathrm{int}ra}$ within all the subbands where the electron can jump into [4.13], [4.15]:

$$\frac{1}{\tau^{u}_{\mathrm{int}ra(\Delta 2/4)}(E)} = \sum_{v} \frac{U(E - E_{\Delta 2/4,v})}{\tau^{u,v}_{ac(\Delta 2/4)}(E)} \tag{4.15}$$

where $U(x)$ is a step function.

On the other side, intervalley phonon scattering is allowed for optical phonon but forbidden for acoustic phonon. Four situations of intervalley transference are from 2-fold valley to 2-fold one, from 2-fold valley to 4-fold one, from 4-fold valley to 2-fold one, and from 4-fold valley to 4-fold one. The scattering rate for each situation is [4.13], [4.15]:

$$\begin{aligned} \frac{1}{\tau^{u,v}_{\mathrm{int}er,\Delta 2->2}(E)} &= \sum_{k}^{\{g\}} \frac{m_{d,\Delta 2}}{2\hbar \rho E_k} \frac{1}{W^1_{u,v}} (N_k + \frac{1}{2} \pm \frac{1}{2}) \\ &\times \frac{1 - f(E \mp E_k)}{1 - f(E)} \times U(E \mp E_k - E_{\Delta 2,v}) \end{aligned} \tag{4.16a}$$

$$W^1_{u,v} = (\int \psi^2_{\Delta 2,u}(z) \psi^2_{\Delta 2,v}(z) dz)^{-1} \tag{4.16b}$$

$$\begin{aligned}\frac{1}{\tau^{u,v}_{\text{inter},\Delta 2->4}(E)} &= \sum_{k}^{\{f\}} \frac{4m_{d,\Delta 4}}{2\hbar\rho E_k}\frac{1}{W^{2}_{u,v}}(N_k+\frac{1}{2}\pm\frac{1}{2}) \\ &\quad\times\frac{1-f(E\mp E_k)}{1-f(E)}\times U(E\mp E_k-E_{\Delta 4,v})\end{aligned} \tag{4.17a}$$

$$W^{2}_{u,v}=(\int\psi^{2}_{\Delta 2,u}(z)\psi^{2}_{\Delta 4,v}(z)dz)^{-1} \tag{4.17b}$$

$$\begin{aligned}\frac{1}{\tau^{u,v}_{\text{inter},\Delta 4->2}(E)} &= \sum_{k}^{\{f\}} \frac{2m_{d,\Delta 2}}{2\hbar\rho E_k}\frac{1}{W^{3}_{u,v}}(N_k+\frac{1}{2}\pm\frac{1}{2}) \\ &\quad\times\frac{1-f(E\mp E_k)}{1-f(E)}\times U(E\mp E_k-E_{\Delta 2,v})\end{aligned} \tag{4.18a}$$

$$W^{3}_{u,v}=(\int\psi^{2}_{\Delta 4,u}(z)\psi^{2}_{\Delta 2,v}(z)dz)^{-1} \tag{4.18b}$$

$$\begin{aligned}\frac{1}{\tau^{u,v}_{\text{inter},\Delta 4->4}(E)} &= \sum_{k}^{\{f\}} \frac{2m_{d,\Delta 4}}{2\hbar\rho E_k}\frac{1}{W^{4}_{u,v}}(N_k+\frac{1}{2}\pm\frac{1}{2}) \\ &\qquad\times\frac{1-f(E\mp E_k)}{1-f(E)}\times U(E\mp E_k-E_{\Delta 4,v}) \\ &\quad+\sum_{k}^{\{g\}} \frac{m_{d,\Delta 4}}{2\hbar\rho E_k}\frac{1}{W^{4}_{u,v}}(N_k+\frac{1}{2}\pm\frac{1}{2}) \\ &\qquad\times\frac{1-f(E\mp E_k)}{1-f(E)}\times U(E\mp E_k-E_{\Delta 4,v})\end{aligned} \tag{4.19a}$$

$$W^{4}_{u,v}=(\int\psi^{2}_{\Delta 4,u}(z)\psi^{2}_{\Delta 4,v}(z)dz)^{-1} \tag{4.19b}$$

where E_k and D_k are the deformation energy and potential with respect to the k_{th}

intervalley phonon. Besides, the signs in $\left(N_k + \frac{1}{2} \pm \frac{1}{2}\right)$ indicate that "+" means phonon emission and "—" means phonon absorption, and N_k the occupation number of the k^{th} intervalley phonon:

$$N_k = \frac{1}{[\exp(\frac{E_k}{k_B T}) - 1]} \tag{4.20}$$

4.3.3 Surface-Roughness-Limited Mobility

The roughness scattering at the Si/SiO$_2$ interface dominates as an important role of a MOSFET at high effective field. That results in the mobility degradation in the inversion layer. Two kinds of assumptions to describe the roughness are well known, one of the Gaussian autocovariance function and the other of the exponential autocovariance function. In this work, we prefer to use the Gaussian autocovariance function, because the calculation of surface roughness scattering rate by exponential model needs larger values of the root mean square amplitude Δ to fit experimentally assessed mobility data than the Gaussian model. Besides, we make an important assumption that the single subband approximation is quite accurate. Since surface roughness is anisotropic scattering, we only consider the intrasubband scattering. Under Yamakawa's surface roughness model [4.12], [4.15], the scattering rate for a Gaussian function is given as

$$\frac{1}{\tau_{sr}^{u,v}(E)} = U(E - E_{\Delta 2/4,v}) \frac{m_{d,\Delta 2/4} q^2 {E_{eff,sr}^{u,v}}^2 \Delta^2 \lambda^2}{2\hbar^3} \int_0^{2\pi} e^{-\frac{k^2\lambda^2}{4}} (1 - \cos\theta) d\theta \tag{4.21}$$

where λ is the correlation length of the roughness, *k* is the difference between the momentum before and after scattering, θ is the angle between the momentum before and after scattering. The elastic collisions without energy transition are assumed:

$$k^2 = \frac{4m_{d,\Delta 2/4}(E - E_{\Delta 2/4,v})}{\hbar^2}(1-\cos\theta) \tag{4.22}$$

$E^{u,v}_{eff,sr}$ is defined as [4.12], [4.15]:

$$E^{u,v}_{eff,sr} = \int_0^\infty \psi_{\Delta 2/4,u}(z)\frac{dV(z)}{dz}\psi_{\Delta 2/4,v}(z)dz \tag{4.23}$$

4.3.4 Impurity-Coulomb-Limited Mobility

Carriers are scattered when they encounter the electric field of an ionized impurity atom. The Coulomb scattering due to ionized impurity atoms in the substrate region causes the degradation of mobility at lower effective field. The perturbing potential is the screened Coulomb potential [4.15], [4.16]:

$$U_s = \frac{q^2}{4\pi\varepsilon_{si} r} e^{-\frac{r}{L_D}} \tag{4.24}$$

where r is the distance from the scattering center and L_D is Debye length:

$$L_D = \sqrt{\frac{\varepsilon_{si} k_B T}{q^2 n}} \tag{4.25}$$

where n is the 3-D density of the mobile carrier. Through the *Fermi's Golden Rule*, the scattering rate by ionized impurity is [4.15]:

$$\frac{1}{\tau_{imp}(E)} = \frac{N_I q^4}{16\sqrt{2m}\pi\varepsilon_{si}^2}[\ln(1+\gamma^2) - \frac{\gamma^2}{1+\gamma^2}]E^{-\frac{3}{2}} \tag{4.26a}$$

$$\gamma^2 = \frac{8mEL_D^2}{\hbar^2} \tag{4.26b}$$

where N_I is the 3-D density of the impurity, that is about equal to N_{sub}. However, Eq. (4.26a) is derived with electron free, not the 2-D electron gas inside the MOSFET. The scattering rate of 2-D carriers from u^{th} subband to v^{th} subband can be derived from Eq. (4.26a) [4.17]:

$$\frac{1}{\tau^{u,v}_{imp,\Delta 2/4}(E)} = \frac{N_I q^4}{16\sqrt{2m}\pi\varepsilon_{si}^2}[\ln(1+\gamma^2) - \frac{\gamma^2}{1+\gamma^2}]E^{-\frac{3}{2}}\frac{g_{2D}(E)}{g_{3D}(E)}\int\psi_u^2(z)\psi_v^2(z)dz \tag{4.27}$$

where $g_{2D/3D}$ is the density of states for 2-D/3-D electrons. In Eq. (4.25), we let $n=N_{inv}/Z_{av}$ in Eq. (4.25) for the convenience of simplicity [4.16]. It should be noticed that only the intrasubband scattering is considered in this work.

4.3.5 Total Mobility

For an electron occupying on Δ2 (Δ4) valley with the energy E, that encounters phonon scattering, surface roughness scattering, and impurity scattering, with the different probabilities. Considering all the possible final states, the scattering probability of the electron is expressed:

$$\frac{1}{\tau^u_{\Delta 2}(E)} = \sum_v\left(\frac{1}{\tau^{u,v}_{intra,\Delta 2}(E)} + \frac{1}{\tau^{u,v}_{inter,\Delta 2\to 2}(E)} + \frac{1}{\tau^{u,v}_{inter,\Delta 2\to 4}(E)} + \frac{1}{\tau^{u,v}_{imp,\Delta 2}(E)}\right) \tag{4.28a}$$

$$\frac{1}{\tau^u_{\Delta 4}(E)} = \sum_v\left(\frac{1}{\tau^{u,v}_{intra,\Delta 4}(E)} + \frac{1}{\tau^{u,v}_{inter,\Delta 4\to 2}(E)} + \frac{1}{\tau^{u,v}_{inter,\Delta 4\to 4}(E)} + \frac{1}{\tau^{u,v}_{imp,\Delta 4}(E)}\right) \tag{4.28b}$$

Because the electron is following the Fermi distribution, the average mobility is:

$$\mu_{\Delta 2}^{u} = \frac{q\int_{E_u}^{\infty}(E-E_u)\tau_{\Delta 2}^{u}(-\frac{\partial f}{\partial E})dE}{m_{c,\Delta 2}\int_{E_u}^{\infty}(E-E_u)(-\frac{\partial f}{\partial E})dE} \qquad (4.29a)$$

$$\mu_{\Delta 4}^{u} = \frac{q\int_{E_u}^{\infty}(E-E_u)\tau_{\Delta 4}^{u}(-\frac{\partial f}{\partial E})dE}{m_{c,\Delta 4}\int_{E_u}^{\infty}(E-E_u)(-\frac{\partial f}{\partial E})dE} \qquad (4.29b)$$

where m_c is the electron effective conductivity mass. The total mobility is the averaged through to weighting of occupation on all subbands:

$$\mu_{tot} = \frac{\sum_{u}\mu_{\Delta 2}^{u}N_{\Delta 2,u} + \sum_{u}\mu_{\Delta 4}^{u}N_{\Delta 4,u}}{N_{inv}} \qquad (4.30)$$

Fig. 4.6 shows the simulated mobility and the experimental one [4.11] of (001)/<110> nMOSFET with different N_{sub}. The parameters we used are listed in Table 4.1.

4.3.6 Matthiessen’s Rule and its Accompanied Error

Matthiessen’s rule is a well-known formula usually used for mobility calculation. Considering those scattering mechanisms we just described, the reciprocal of final mobility should be the summation of the reciprocal of the separate mobility components:

$$\mu_{tot,M} = \left(\frac{1}{<\mu_{\mathrm{int}ra}>} + \frac{1}{<\mu_{\mathrm{int}er}>} + \frac{1}{<\mu_{sr}>} + \frac{1}{<\mu_{\mathrm{i}mp}>}\right)^{-1} \qquad (4.31)$$

The error and the validity of Matthiessen’s rule have been discussed for a long time

[4.6], [4.11], [4.18]-[4.22]. It has been pointed out that the errors due to the use of Matthiessen’s rule will be more than 15% for temperatures over 40K [4.18]. The error comes from two origins: (1) the relative strength of individual mobility components [4.18], and (2) the subband population [4.21]. *NEP* provides an error-free version of mobility. It can help us to ensure the applicability of this rule.

In Fig. 4.7, the total mobility μ_{tot} and its components are shown. The total mobility calculated by Matthiessen’s rule $\mu_{tot,M}$ is also shown. Fig. 4.7 shows many interesting results. First, the $\mu_{tot,M}$ is always larger then μ_{tot}, meaning that the mobility extraction by using Matthiessen’s rule will overestimate the actual value [4.22]. The second one is that the maximum relative error occurs near a critical condition where two individual mobility components intercept. It is the first source of error we just mentioned. Third, the error due to impurity part is larger than phonon part that has been mentioned in [4.22]. The last one is the maximum errors due to phonon part are smaller for high doping concentrations than low one. It is related to the second source of error. In Fig. 4.7, the arrow indicates the E_{eff} where phonon and surface roughness limited mobilities have the same value. The inset shows corresponding population of two lowest subbands. Because the separation of subband is strongly with high doping concentration, more inversion layer carriers occupy on the lowest subband. Therefore, the maximum error is reduced. In a sense, care must be taken when apply the Matthiessen’s rule.

4.4 Conclusion

Mobility is a parameter which is sensitive to strain. To address the mobility mechanisms, the 2-D electron mobility including impurity, phonon, and surface roughness scattering can be calculated by a fully self-consistent Schrődinger and Poisson equations solver. With the accurate calculation on scattering rate, we estimated the errors due to the use of Matthiessen’s rule.

References

[4.1] C. Herring and E. Vogt, “Transport and deformation-potential theory for many-valley semiconductors with anisotropic scattering,” *Phys. Rev.*, vol. 101, no. 3, pp. 944–961, Feb. 1956.

[4.2] I. Balslev, “Influence of uniaxial stress on the indirect absorption edge in silicon and germanium,” *Phys. Rev.*, vol. 143, no. 2, pp. 636–647, Mar. 1966.

[4.3] C. G. Van de Walle and R. M. Martin, “Theoretical calculations of heterojunction discontinuities in the Si/Ge system,” *Phys. Rev. B, Condens. Matter*, vol. 34, no. 8, pp. 5621–5634, Oct. 1986.

[4.4] M. V. Fischetti and S. E. Laux, “Band structure, deformation potentials, and carrier mobility in strained Si, Ge, and SiGe alloys,” *J. Appl. Phys.*, vol. 80, no. 4, pp. 2234–2252, Aug. 1996.

[4.5] M. J. Chen, C. C. Lee, and K. H. Cheng, “Hole effective masses as a booster of self-consistent six-band k • p simulation in inversion layers of pMOSFETs,” *IEEE Trans. Electron Devices*, vol. 58, no. 4, pp. 931-937, Apr. 2011.

[4.6] M. J. Chen, S. C. Chang, S. J. Kuang, C. C. Lee, W. H. Lee, K. H. Cheng, and Y. H. Zhan, “Temperature-dependent remote-Coulomb-limited electron mobility in n+-polysilicon ultrathin gate oxide nMOSFETs,” *IEEE Trans. Electron Devices*, vol. 58, no. 4, pp. 1038-1044, Apr. 2011.

[4.7] Schred. [Online]. Available: http://nanohub.org/resources/schred.

[4.8] A. G. Sabnis and J. T. Clemens, “Characterization of the electron mobility in the inverted <100> Si surface,” in *IEDM Tech. Dig.*, 1979, pp. 18-21.

[4.9] F. Gámiz, J. B. Roldán, J. A. López-Villanueva, P. Cartujo-Cassinello, and J. E. Carceller, “Surface roughness at the Si-SiO$_2$ interfaces in fully depleted silicon-on-insulator inversion layers,” *J. Appl. Phys.*, vol. 86, no. 12, pp.

6854–6863, Dec. 1999.

[4.10] F. Gámiz and M. V. Fischetti, “Monte Carlo simulation of double-gate silicon-on-insulator inversion layers: the role of volume inversion,” *J. Appl. Phys.*, vol. 89, no. 10, pp. 5478–5487, May 2001.

[4.11] S. Takagi, A. Toriumi, M. Iwase, and H. Tango, “On the universality of inversion layer mobility in Si MOSFETs: Part I—Effects of substrateimpurity concentration,” *IEEE Trans. Electron Devices*, vol. 41, no. 12, pp. 2357–2362, Dec. 1994.

[4.12] S. Yamakawa, H. Ueno, K. Taniguchi, C. Hamaguchi, K. Miyatsuji, K. Masaki, and U. Ravaioli, “Study of interface roughness dependence of electron mobility in Si inversion layers using the Monte Carlo method,” *J. Appl. Phys.*, vol. 79, no. 2, pp. 911–916, Jan. 1996.

[4.13] S. Takagi, J. L. Hoyt, J. J. Welser, and J. F. Gibbons, “Comparative study of phonon-limited mobility of two-dimensional electrons in strained and unstrained Si metal-oxide-semiconductor field-effect transistors,” *J. Appl. Phys.*, vol. 80, no. 3, pp. 1567, Aug. 1996.

[4.14] K. Uchida, T. Krishnamohan, K. C. Saraswat, and Y. Nishi, “Physical mechanisms of electron mobility enhancement in uniaxial stressed MOSFETs and impact of uniaxial stress engineering in ballistic regime,” in *IEDM Tech. Dig.*, 2005, pp. 129–132.

[4.15] M. Lundstrom, “Fundamentals of carrier transport,” *Cambridge University Press*, 2000.

[4.16] S. Potbhare, N. Goldsman, G. Pennington, A. Lelis, and J. M. McGarrity, “A quasi-two-dimensional depth-dependent mobility model suitable for device simulation for Coulombic scattering due to interface trapped charges,” *J. Appl.*

Phys., vol. 100, no. 4, pp. 044516-1–044516-7, Aug. 2006.

[4.17] K. Hirakawa and H. Sakaki, “Mobility of the two-dimensional electron gas at selectively doped n-type $Al_xGa_{1-x}As$/GaAs heterojunctions with controlled electron concentrations,” *Phys. Rev. B, Condens. Matter*, vol. 33, no. 12, 8291-8303, Jun. 1986.

[4.18] F. Stern, “Calculated temperature dependence of mobility in silicon inversion layers,” *Phys. Rev., Lett*., vol. 44, no. 22, pp. 1469-1472, Jun.1980.

[4.19] J. Li and T. P. Ma, “Scattering of silicon inversion layer electrons by metal/oxide interface roughness,” *J. Appl. Phys.*, vol. 62, no. 10, pp. 4212-4215, Nov. 1987.

[4.20] J. R. Hauser, “Extraction of experimental mobility data for MOS devices,” *IEEE Trans. Electron Devices*, vol. 43, no. 11, pp. 1981-1988, Nov. 1996.

[4.21] M. V. Fischetti, F. Gámiz, and W. Hänsch, “On the enhanced electron mobility in strained-silicon inversion layers,” *J. Appl. Phys.*, vol. 92, no. 12, pp. 7320-7324, Dec. 2002.

[4.22] D. Esseni and F. Driussi, “A quantitative error analysis of the mobility extraction according to the Matthiessen rule in advanced MOS transistors,” *IEEE Trans. Electron Devices*, vol. 58, no. 8, pp. 2415-2422, Aug. 2011.

Table 4.1 The value of parameters that are used in mobility calculation.

D_{ac}	13 eV
D_k	$11.5\text{x}10^{8}$ ev/cm
ρ	$2.329\text{x}10^{3}$ kg/cm^{3}
s_l	$9.037\text{x}10^{5}$ cm/s
E_k of f type scattering	0.059 eV/cm
E_k of g type scattering	0.063 eV/cm
λ	1.49 nm
Δ	0.29 nm

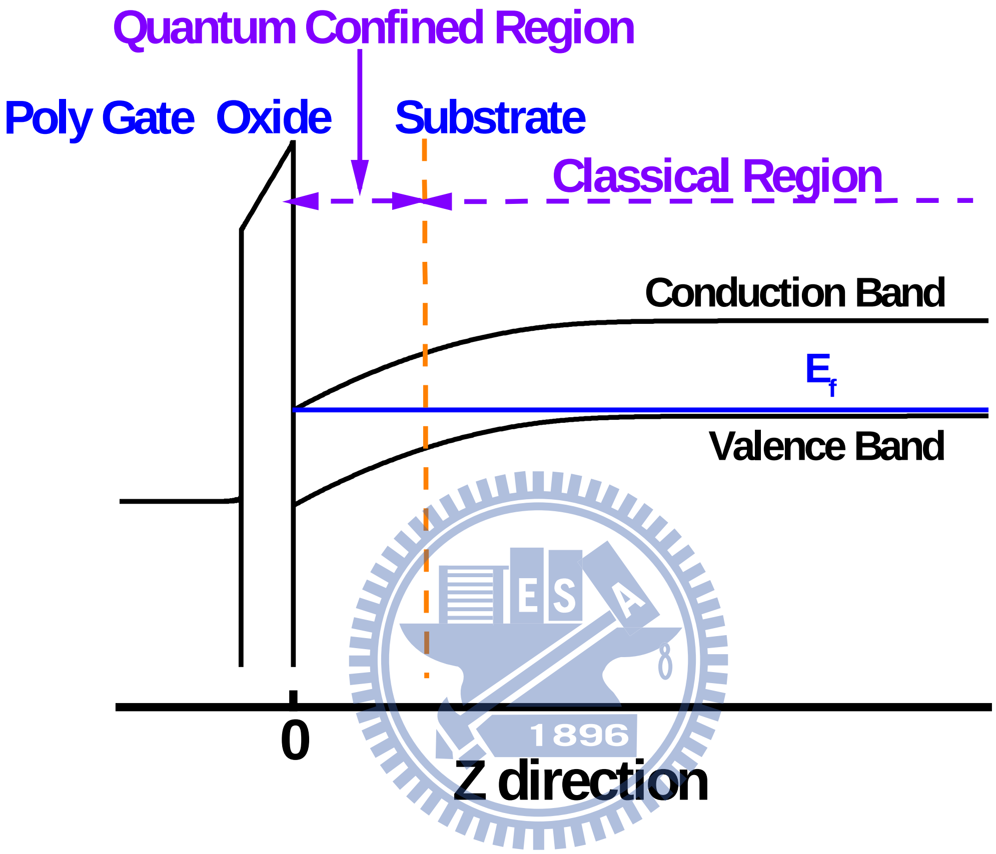

Fig. 4.1 The energy band diagram in a poly gate/SiO_2/p-substrate system.

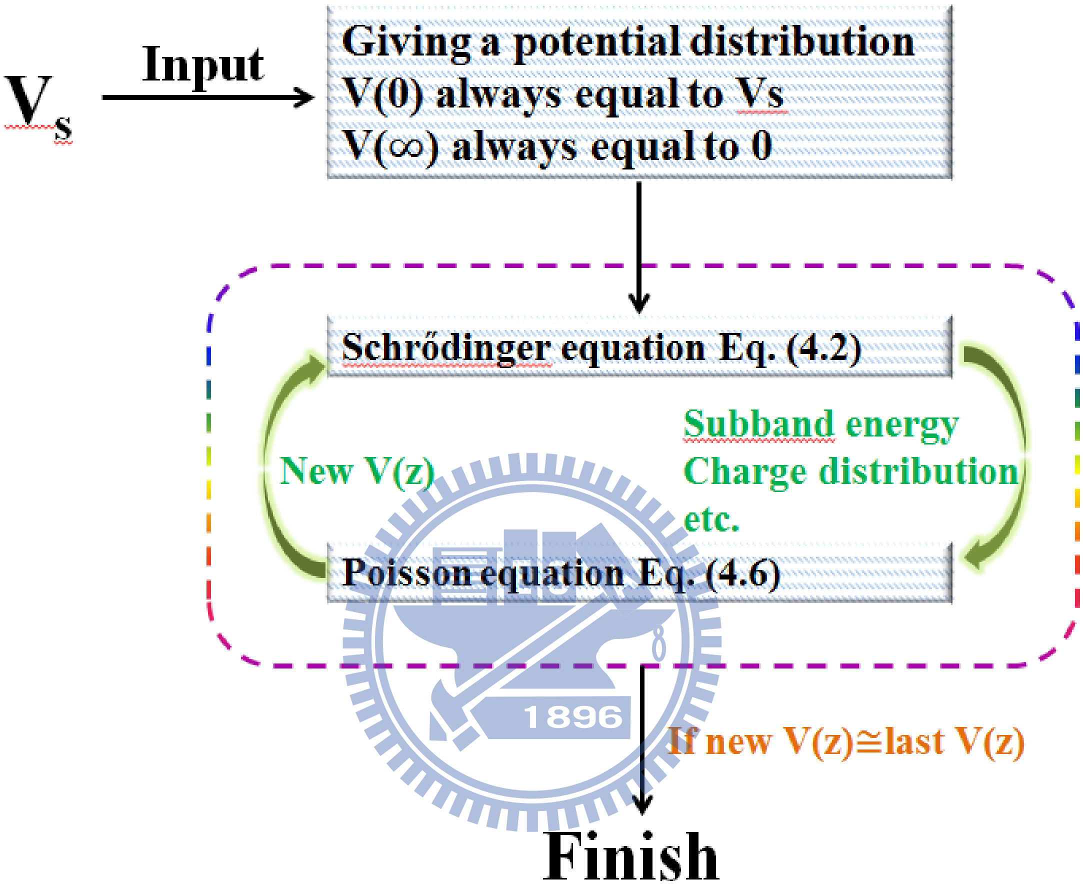

Fig. 4.2 The flow chart of the calculation process in *NEP*.

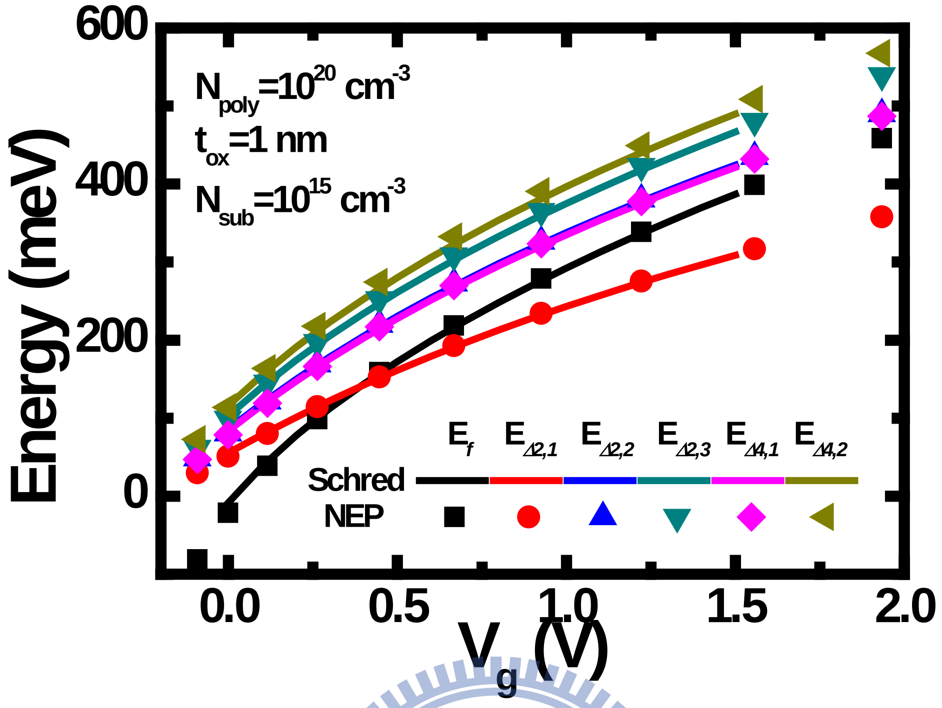

(a)

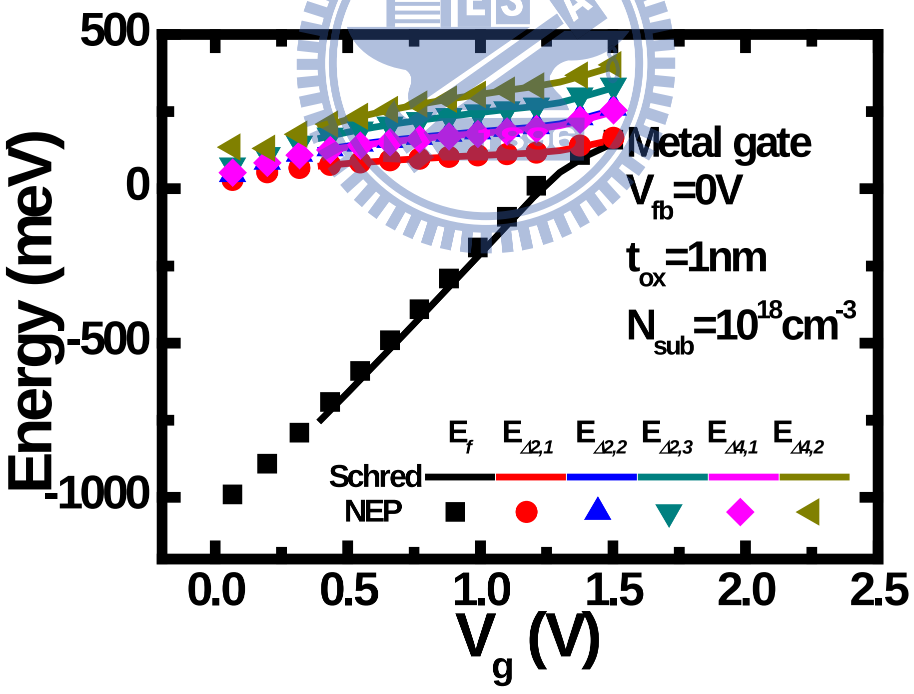

(b)

Fig. 4.3 Subband levels calculated by the *NEP* (solid dots) and by *Schred* (lines) for two cases as Fig. 2.3.

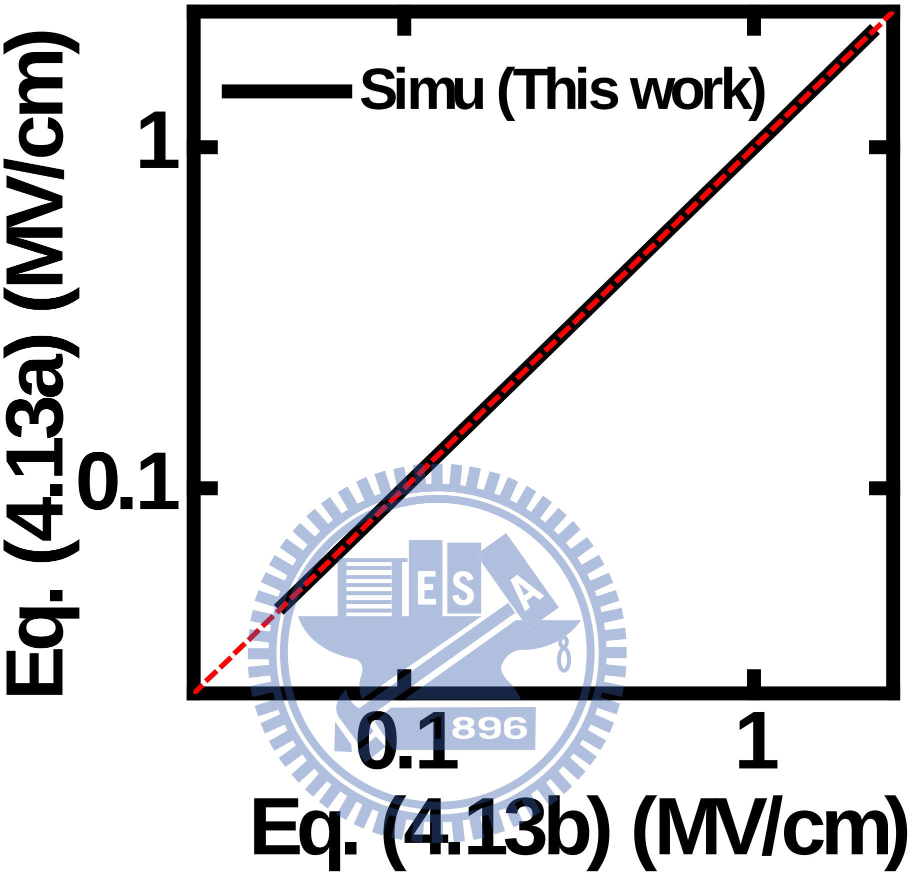

Fig. 4.4 Comparison between Eq. (4.13a) and (4.13b) which by *NEP* (Solid line). The dashed line is the line with a slope of 1 and through the origin.

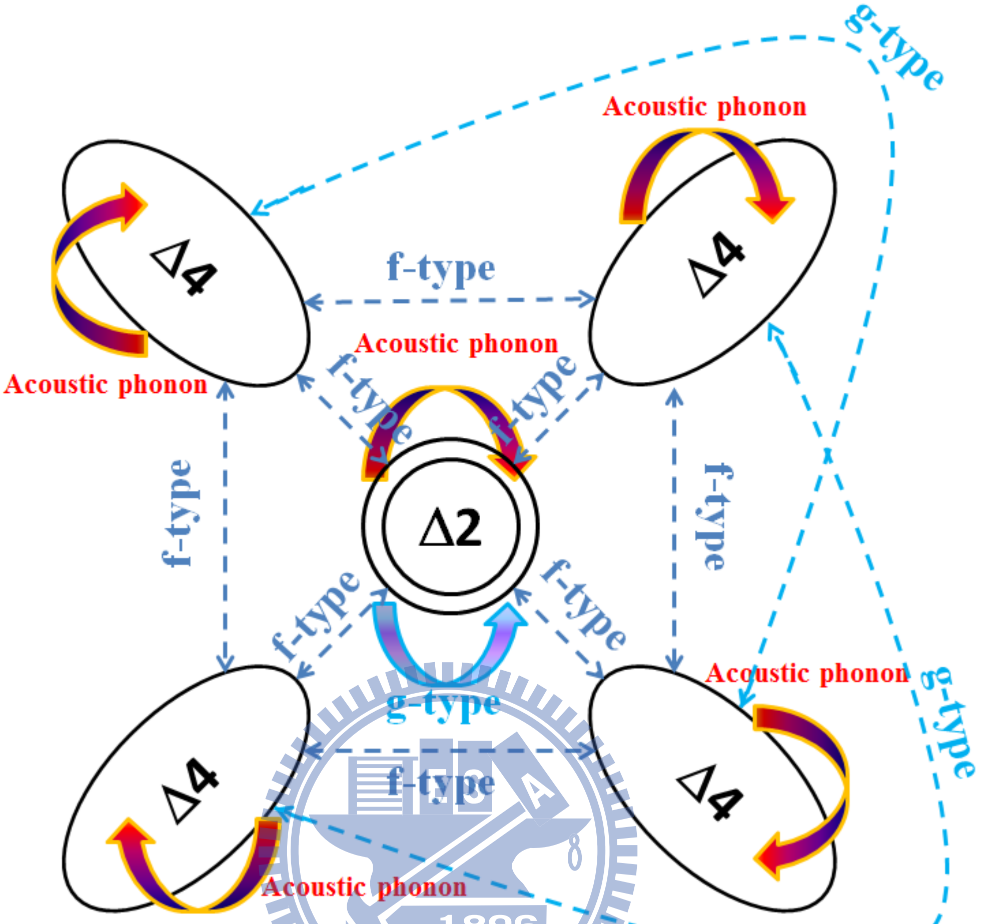

Fig. 4.5 All the phonon scattering mechanisms. Intravalley scattering involves acoustic phonon; and long range intervalley scattering and short range intervalley scattering involve g-type optical phonon and f-type one, respectively.

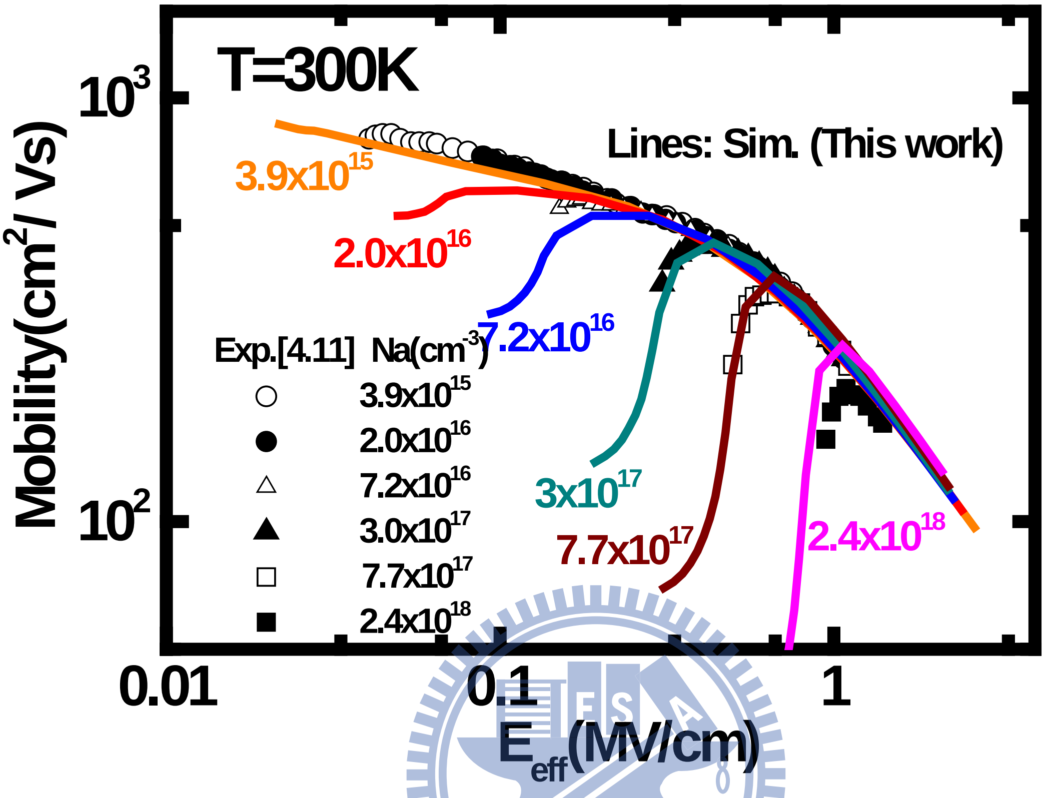

Fig. 4.6 Comparison of the mobility calculated by this work (lines) and the experimental mobility data (dots). The calculated mobility includes impurity scattering, phonon scattering, and surface roughness scattering.

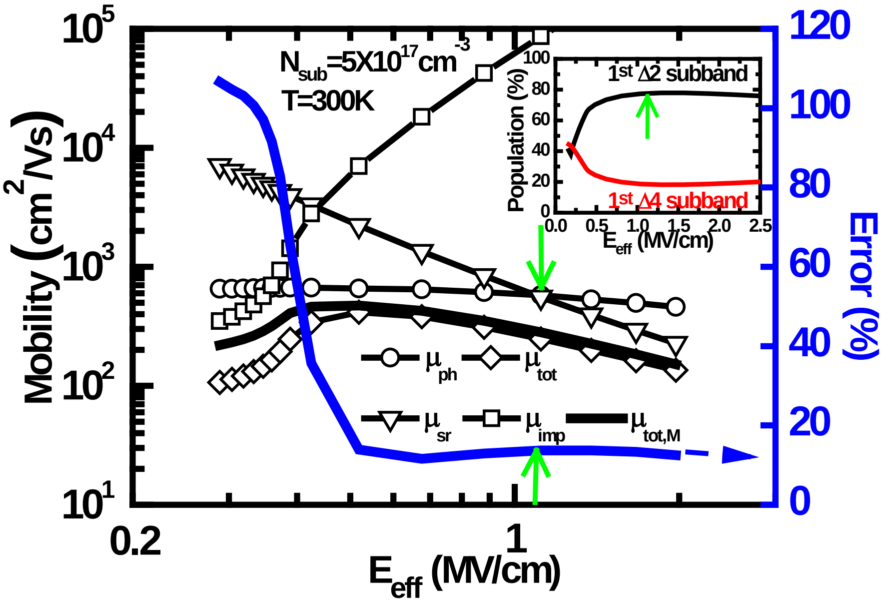

(a)

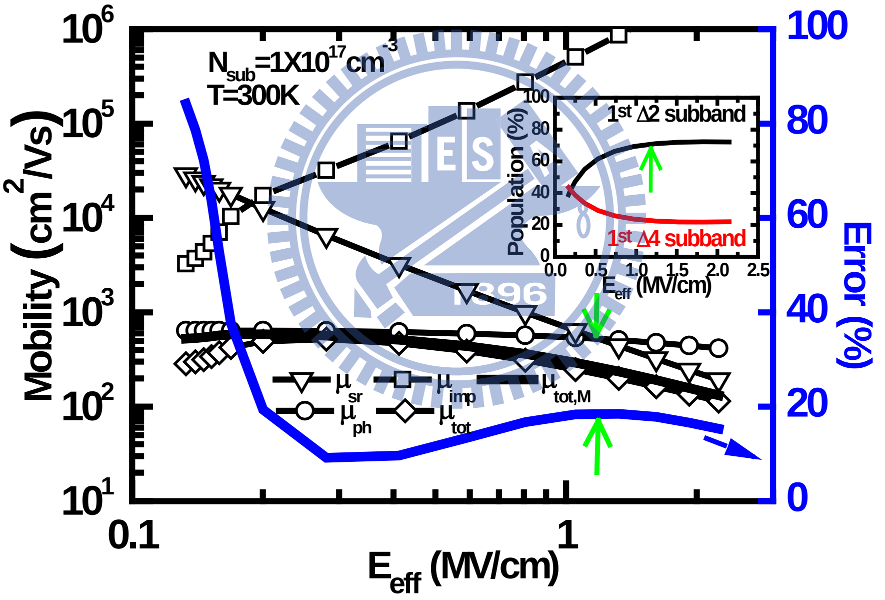

(b)

Fig. 4.7 The total mobility (lines) obtained by Matthiessen's rule, and the simulated total mobility, phonon and surface roughness limited mobilities (lines with symbols) versus E_{eff} for (a) N_{sub} = 5×10^{17} cm^{-3},and (b) N_{sub} = 10^{17} cm^{-3} at 300K. The arrow indicates the critical *Eeff* where phonon and surface roughness limited mobilities have the same value. The inset shows corresponding population of two lowest subbands.

Chapter 5

Strain Altered Mobility

5.1 Introduction

We have already extracted the piezo-effective-mass coefficients of two-dimensional electrons through the gate tunneling current measured from <110> uniaxial compressive strained (001) nMOSFETs. On the other hand, mobility-based assessment of π_m was also performed [5.1]. In these methods [5.1]-[5.5], however, the role of the 4-fold valley Δ_4 out-of-plane π_m was overlooked. This led to an argument that the Δ_4 out-of-plane π_m should not be absent.

In this chapter we provide extra evidence for the existence of the fourfold out-of-plane piezo-effective-mass coefficient. Explicit guidelines are first drawn, followed by use of *NEP* to fit existing data of both the mobility enhancement and gate current suppression in the presence of <110> uniaxial tensile stress. Fitting results point out that the fourfold out-of-plane piezo-effective-mass coefficient is existent in the warping band structure under <110> tensile stress, which can significantly affect the mobility enhancement and gate current suppression. Underlying physical mechanisms are presented.

5.2 Guidelines and Simulators

The aforementioned study [5.6] on 2-D electrons revealed that for twofold Δ_2 valleys, the confinement $\pi_{m,z\Delta2} \approx 0$ and 2-D density-of-states (DOS) $\pi_{m,d\Delta2} \approx -0.017$

to -0.03 m_0/GPa; and for Δ_4 valleys, $\pi_{m,z\Delta 4} \approx 0.03$ to 0.07 m_0/GPa and 2-D DOS $\pi_{m,d\Delta 4} \approx 0$. Apparently, a zero valleys, $\pi_{m,z\Delta 4} \approx 0.03$ to 0.07 m_0/GPa and 2-D DOS $\pi_{m,d\Delta 4} \approx 0$. Apparently, a zero $\pi_{m,d\Delta 4}$ dictates that the longitudinal $\pi_{m,l\Delta 4} = 0$ and transverse $\pi_{m,t\Delta 4} = 0$; and a negative $\pi_{m,d\Delta 2}$ means that at least one of $\pi_{m,t\Delta 2\parallel}$ and $\pi_{m,t\Delta 2\perp}$ is negative and its magnitude is larger than another having a positive value. These coefficients $\pi_{m,t\Delta 2\parallel}$ and $\pi_{m,t\Delta 2\perp}$ correspond to the in-plane longitudinal effective mass $m_{t,\Delta 2\parallel}$ and transverse effective mass $m_{t,\Delta 2\perp}$ of Δ_2, respectively, as shown in Fig. 5.1. Considering the nature of the warping band under <110> uniaxial stress [5.7], [5.8], we have $\pi_{m,t\Delta 2\parallel} < 0$ and $\pi_{m,t\Delta 2\perp} > 0$ but the corresponding magnitudes must be constrained by satisfying the resulting $\pi_{m,d\Delta 2}$ that lies between -0.017 to -0.03 m_0/GPa.

Thus, explicit guidelines can be created as follows: for Δ_4 valleys, $\pi_{m,d\Delta 4} = 0$, $\pi_{m,l\Delta 4} = 0$, $\pi_{m,t\Delta 4} = 0$, and $\pi_{m,z\Delta 4}$ ranges from 0.03 to 0.07 m_0/GPa; and for Δ_2 valleys, $\pi_{m,z\Delta 2} = 0$, $\pi_{m,t\Delta 2\parallel} < 0$, $\pi_{m,t\Delta 2\perp} > 0$, and $\pi_{m,d\Delta 2}$ of -0.017 to -0.03 m_0/GPa. Obviously, only three coefficients, $\pi_{m,z\Delta 4}$, $\pi_{m,t\Delta 2\parallel}$, and $\pi_{m,t\Delta 2\perp}$, are needed in the subsequent simulation, along with other π_m's kept at zero.

To quantify the strain-altered electron mobility and gate tunneling current, the numerical solvers *NEP* is readily available in this work. By combining the gate electron tunneling current simulation which is introduced in Chapter 3, an electron mobility simulator [5.9] which is introduced in Chapter 4, and the strain Hamiltonian [5.10] which is introduced in Chapter 3, we reach a sophisticated self-consistent strain quantum simulator. Note that relative to the triangular potential approach in *TRP*, the presented self-consistent version in this work can provide accurate wave-functions that are needed in the mobility calculation.

5.3 Results and Discussion

Mobility enhancement data [5.2] are plotted in Figure. 5.2 versus vertical effective field. The detailed information [5.2] is that the channel length direction is along <110> direction on (001) nMOSFETs; two in-plane uniaxial tensile stresses, $\sigma_{//}$ and $\sigma_{\perp}$, are externally applied in <110> and <-110> direction, respectively; and phonon-scattering-limited mobility enhancement is simulated with zero π_m, as together plotted. Simulated mobility enhancement in this work with zero π_m is shown for validation. The non-stress effective mass values (i.e., $m(0)$ in Eq. (3.16)) used in simulation were the same as the work in Chapter 3 (see Table 3.2 therein). Good agreement with that of [5.2] is evident, valid for a wide range of substrate doping concentrations. Additional simulation results by varying $\pi_{m,z\Delta4}$ reveal that an increase in $\pi_{m,z\Delta4}$ will degrade mobility.

Interestingly, for the case of $\pi_{m,z\Delta4} = 0$, $\sigma_{||}$ and $\sigma_{\perp}$ mobility data can be fitted well by separately adjusting $\pi_{m,t\Delta2||}$ and $\pi_{m,t\Delta2\perp}$ to -0.02 and 0.02 m_0/GPa, which are close to those of the citation [5.2]. Such a fitting process is again repeated for other values of $\pi_{m,z\Delta4}$. The results are plotted in Fig. 5.3. The corresponding π_m values are given in Fig. 5.1 in terms of four different conditions. Clearly, both $\pi_{m,t\Delta2||}$ and $\pi_{m,t\Delta2\perp}$ are coupled with the $\pi_{m,z\Delta4}$: $\pi_{m,t\Delta2||}$ increases negatively with $\pi_{m,z\Delta4}$, whereas $\pi_{m,t\Delta2\perp}$ exhibits a decreasing trend. The extracted values of π_m are further used to calculate the gate tunneling current change under uniaxial tensile stress. The results are shown in Fig. 5.4, along with the literature data [5.11], [5.12] for comparison. It can be seen that the higher the $\pi_{m,z\Delta4}$, the less the deviation it will produce. Meanwhile, good agreement with mobility data holds, as in Fig. 5.3.

Therefore, the coefficient $\pi_{m,z\Delta4}$ plays a vital role. To highlight this, we show in

Fig. 5.1 that an increase in $\pi_{m,z\Delta 4}$ increases the Δ_4 quantization effective mass under tensile stress, which will in turn render the Δ_4 level lowered. As a result of the valley repopulation, more electrons jump from Δ_2 to Δ_4. This reflects a decrease in the Δ_2 valley occupancy. Thus, there are two effects caused solely by varying $\pi_{m,z\Delta 4}$: The gate tunneling current is increased and the mobility is degraded. The detailed interpretations, as already presented in the opposite case (compressive) in Chapter 3, can be applied to the former. As to the latter, the following formula may be useful:

$$\mu = \frac{q\tau_{\Delta 2}}{m_{c,\Delta 2}}\gamma + \frac{q\tau_{\Delta 4}}{m_{c,\Delta 4}}(1-\gamma) \tag{5.1}$$

where $\tau_{\Delta 2}$ and $\tau_{\Delta 4}$ represent the mean scattering time of Δ_2 and Δ_4 valley, respectively; γ represents the Δ_2 valley occupancy. Here, $m_{c,\Delta 2} = m_{t,\Delta 2\parallel}$ for <110> stress or $\mathrm{m}_{t,\Delta 2\perp}$ for <-110> stress; and $m_{c,\Delta 4} = 2(m_{t,\Delta 4}\, m_{l,\Delta 4})/(m_{t,\Delta 4} + m_{l,\Delta 4})$ [5.13]. A decrease of γ favors the second term of Eq. (5.1) featuring a higher $m_{c,\Delta 4}$, which will in turn degrade the overall mobility.

Further simulation was done at higher tensile stress. The comparison of simulated mobility enhancement with the published ones [5.2] is inserted to Fig. 5.3, plotted versus tensile strain of up to 1.0 %. Fairly good agreement is reached for Condition 1 whose π_m's are close to [5.2] (also see Table 3.3). This validates the presented self-consistent strain quantum simulator. For other conditions, mobility enhancement strongly increases, particularly in the higher tensile strain region. However, there is one of the fundamental limits that must be kept in mind: π_m in Eq. (3.16) essentially works in low stress situations. Indeed, such a low tensile strain region can be located (< 0.2 %), where the simulated mobility enhancement coincides with that of [5.2], regardless of the simulation conditions used. Straightforwardly, we want to stress that the current band structure calculation methods [5.1]-[5.5] did not explicitly address the significance of the Δ_4 out-of-plane π_m. Thus, in the area of band structure calculations a further investigation is needed in this direction.

5.4 Conclusion

Explicit guidelines have been drawn for all the piezo-effective-mass coefficients: 1) for Δ_4 valleys, $\pi_{m,d\Delta4} = 0$, $\pi_{m,l\Delta4} = 0$, $\pi_{m,t\Delta4} = 0$, and $\pi_{m,z\Delta4}$ of 0.03 to 0.07 m_0/GPa; and 2) for Δ_2 valleys, $\pi_{m,z\Delta2} = 0$, $\pi_{m,t\Delta2||} < 0$, $\pi_{m,t\Delta2\perp} > 0$, and $\pi_{m,d\Delta2}$ of -0.017 to -0.03 m_0/GPa. The self-consistent strain quantum simulator has been carried out while fitting both the enhanced mobility and suppressed gate current data under <110> uniaxial tensile stress. The results have corroborated the fourfold-valley out-of-plane $\pi_{m,z\Delta4}$ and have suggested the required re-examination of the current band structure calculations.

References

[5.1] F. Rochette, M. Cassé, M. Mouis, G. Reimbold, D. Blachier, C. Leroux, B. Guillaumot, and F. Boulanger, “Experimental evidence and extraction of the electron mass variation in [110] uniaxially strained MOSFETs,” *Solid-State Electronics*, vol. 51, no. 11-12, pp. 1458-1465, Nov.-Dec. 2007.

[5.2] K. Uchida, T. Krishnamohan, K. C. Saraswat, and Y. Nishi, “Physical mechanisms of electron mobility enhancement in uniaxial stressed MOSFETs and impact of uniaxial stress engineering in ballistic regime,” in *IEDM Tech. Dig.*, 2005, pp. 129–132.

[5.3] S. Dhar, E. Ungersböck, H. Kosina, T. Grasser, and S. Selberherr, “Electron mobility model for <110> stressed silicon including strain-dependent mass,” *IEEE Trans. Nanotechnology*, vol. 6, no. 1, pp. 97-100, Jan. 2007.

[5.4] E. Ungersboeck, S. Dhar, G. Karlowatz, V. Sverdlov, H. Kosina, and S. Selberherr, “The effect of general strain on the band structure and electron mobility of silicon,” *IEEE Trans. Electron Devices*, vol. 54, no. 9, pp. 2183-2190, Sep. 2007.

[5.5] V. Sverdlov, *Strain-Induced Effects in Advanced MOSFETs*, Germany, Springer-Verlag/Wien, 2011.

[5.6] W. H. Lee and M. J. Chen, ”Gate direct tunneling current in uniaxially compressed strained nMOSFETs: a sensitive measure of electron piezo effective mass,” *IEEE Trans. Electron Devices*, vol. 58, no. 1, pp. 39-45, Jan. 2011.

[5.7] Y. Kanda and K. Suzuki, “Origin of the shear piezoresistance coefficient □44 of n-type silicon,” *Phys. Rev. B*, vol. 43, no. 8, pp. 6754-6756, Mar. 1991.

[5.8] K. Uchida, T. Krishnamohan, K. C. Saraswat, and Y. Nishi, “Physical mechanisms of electron mobility enhancement in uniaxial stressed MOSFETs and impact of uniaxial stress engineering in ballistic regime," in *IEDM Tech. Dig.*, 2005, pp. 129–132.

[5.9] M. J. Chen, S. C. Chang, S. J. Kuang, C. C. Lee, W. H. Lee, K. H. Cheng, and Y. H. Zhan, "Temperature-dependent remote-Coulomb-limited electron mobility in n+-polysilicon ultrathin gate oxide nMOSFETs," *IEEE Trans. Electron Devices*, vol. 58, no. 4, pp. 1038-1044, Apr. 2011.

[5.10] N. Yang, W. K. Henson, J. R. Hauser, and J. J. Wortman, "Modeling study of ultrathin gate oxides using direct tunneling current and capacitance-voltage measurements in MOS devices," *IEEE Trans. Electron Devices*, vol. 46, no. 7, pp. 1464–1471, Jul. 1999.

[5.11] X. Yang, Y. Choi, T. Nishida, and S. E. Thompson, "Gate direct tunneling currents in uniaxial stressed MOSFETs," in *IEDST*, 2007, pp. 149-152.

[5.12] W. Zhao, A. Seabaugh, V. Adams, D. Jovanovic, and B. Winstead, "Opposing dependence of the electron and hole gate currents in SOI MOSFETs under uniaxial strain," *IEEE Electron Device Lett.*, vol. 26, no. 6, pp. 410-412, Jun. 2005.

[5.13] F. Stern, "Self-consistent results for n-type Si inversion layers," *Phys. Rev. B*, vol. 5, no.12, pp.4891-4899, Jun. 1972.

[5.14] X. Yang, Y. Choi, T. Nishida, and S. E. Thompson, "Gate direct tunneling currents in uniaxial stressed MOSFETs," in *IEDST*, 2007, pp. 149-152.

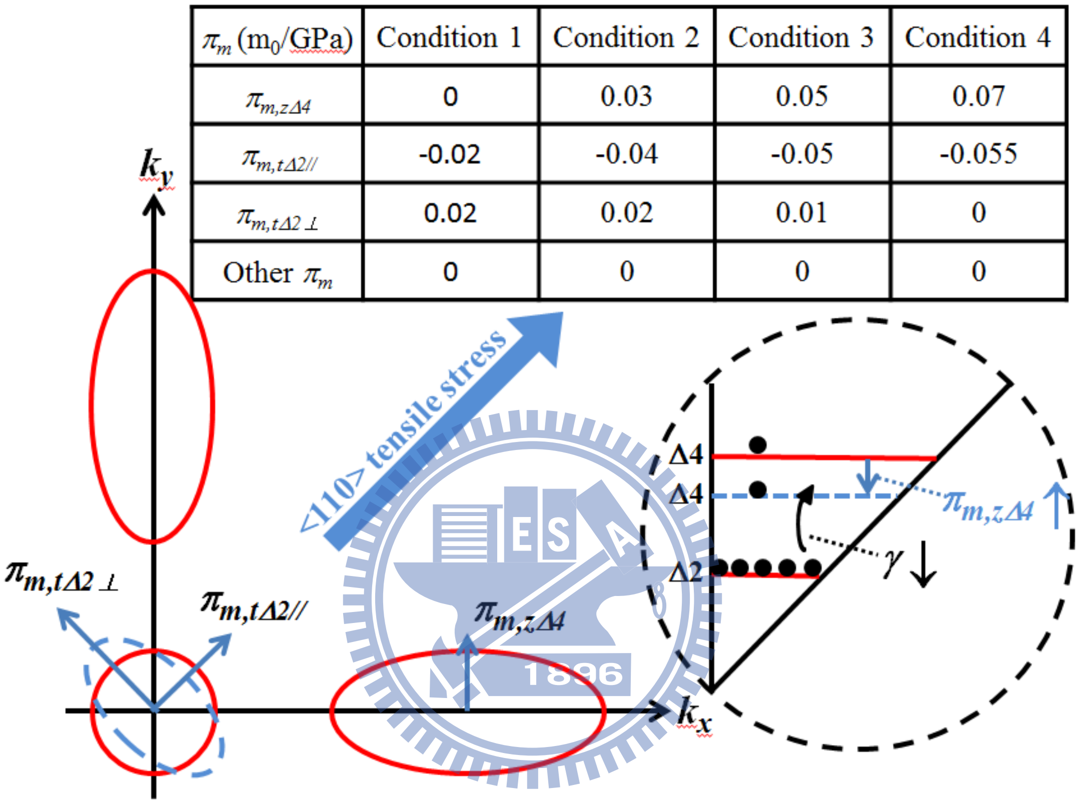

π_m (m$_0$/GPa)	Condition 1	Condition 2	Condition 3	Condition 4
$\pi_{m,z\Delta4}$	0	0.03	0.05	0.07
$\pi_{m,t\Delta2//}$	-0.02	-0.04	-0.05	-0.055
$\pi_{m,t\Delta2\perp}$	0.02	0.02	0.01	0
Other π_m	0	0	0	0

Fig. 5.1 Schematic diagram of one Δ_2 valley and two Δ_4 valleys in k_x-k_y plane. The channel length direction is along <110> uniaxial tensile stress direction on (001) substrate. Dashed line around the Δ_2 valley in terms of the longitudinal and transverse piezo-effective-mass coefficients, as well as the Δ_4 out-of-plane piezo-effective-mass coefficient, shows the effect of stress. The two insets are added: one for the listed values of the piezo-effective-mass coefficients used for simulation in Figs. 5.3 and 5.4; and the other for the effect of Δ_4 out-of-plane piezo-effective-mass coefficient.

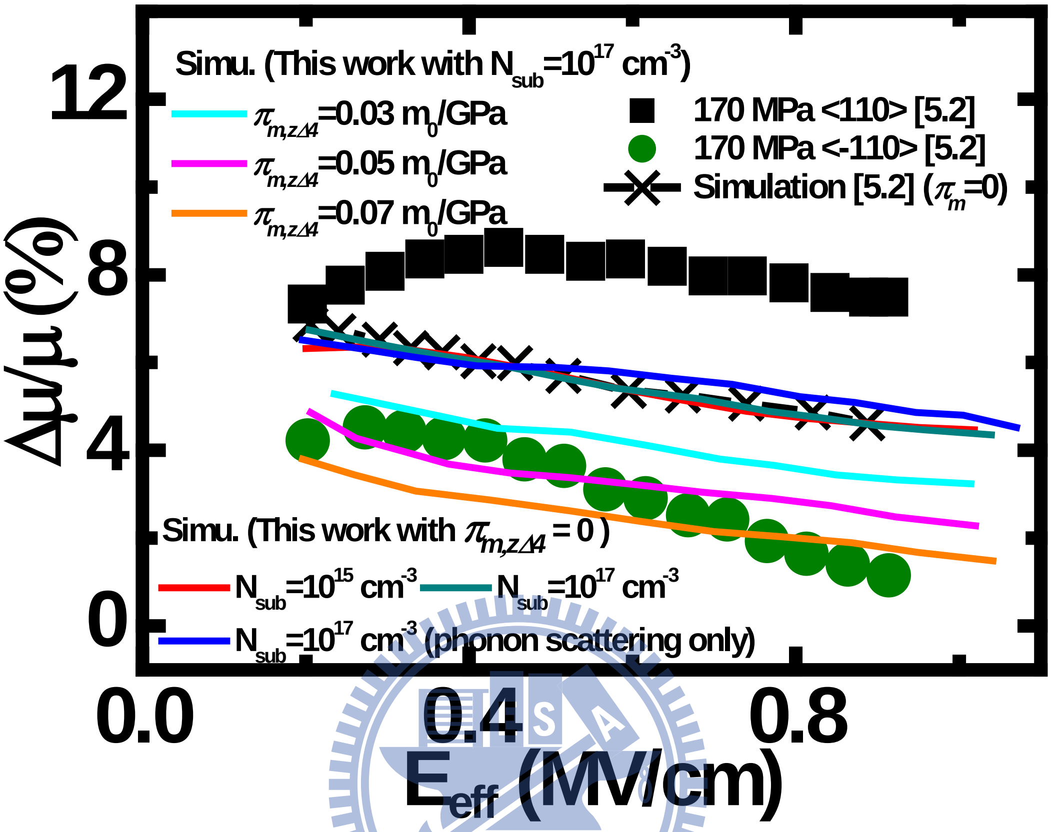

Fig 5.2 Comparison of simulated mobility enhancement (cross symbols) due to <110> 170MPa with all π_m=0 [5.2] and those (lines) obtained in this work under different conditions (substrate doping concentration N_{sub} of 10^{15} and 10^{17} cm^{-3}; and N_{sub} of 10^{17} cm^{-3} without surface roughness scattering). The simulated mobility enhancement values (lines) are comparable of each other, indicating that phonon scattering dominates. Other simulation lines are produced to highlight the impact of the Δ_4 out-of-plane piezo-effective-mass coefficient alone. Experimental data (squares and circles) [5.2] are together plotted for comparison.

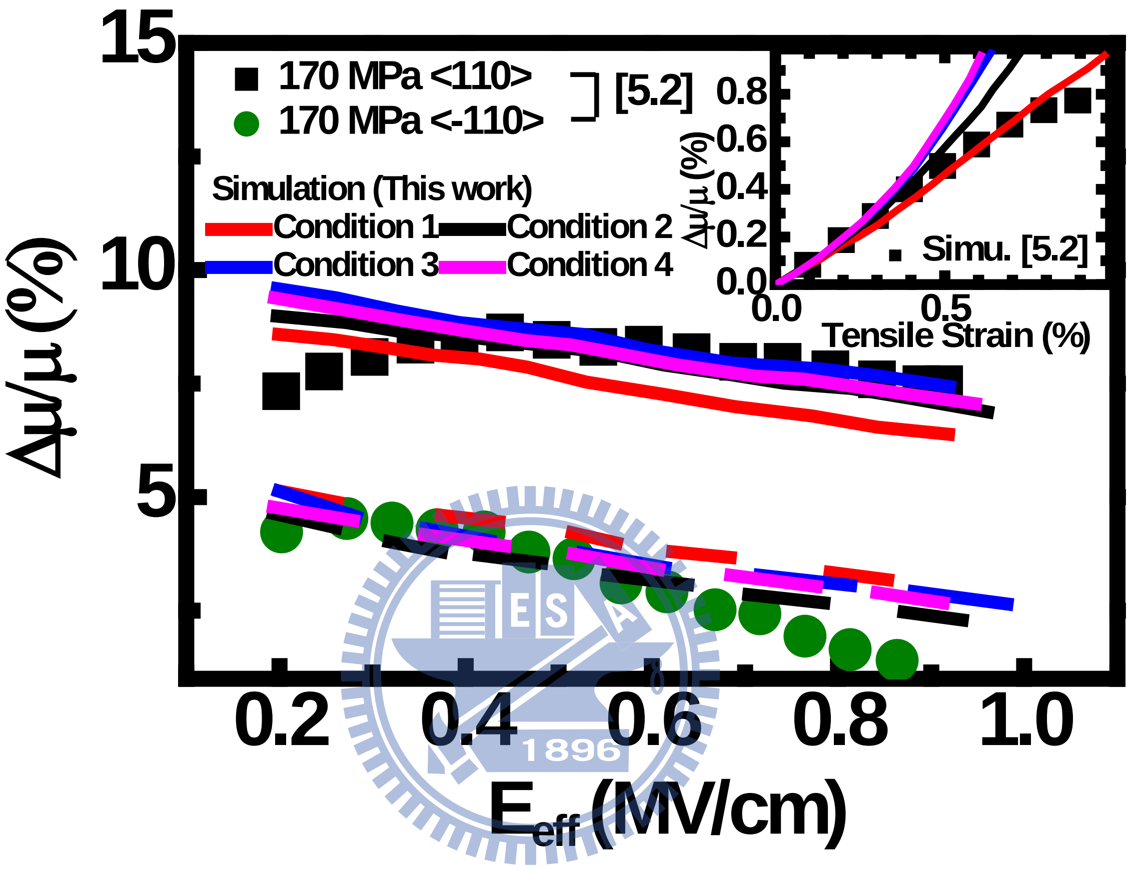

Fig. 5.3 Comparison of mobility enhancement data (symbols) [5.2] under <110> and <-110> 170 MPa tensile stress with the simulated ones (lines) for four different conditions in Fig. 1, plotted versus vertical effective field. The substrate doping concentration of 10^{17} cm^{-3} is used in this work. The inset shows the comparison of simulated mobility enhancement versus tensile strain with the published simulation values [5.2].

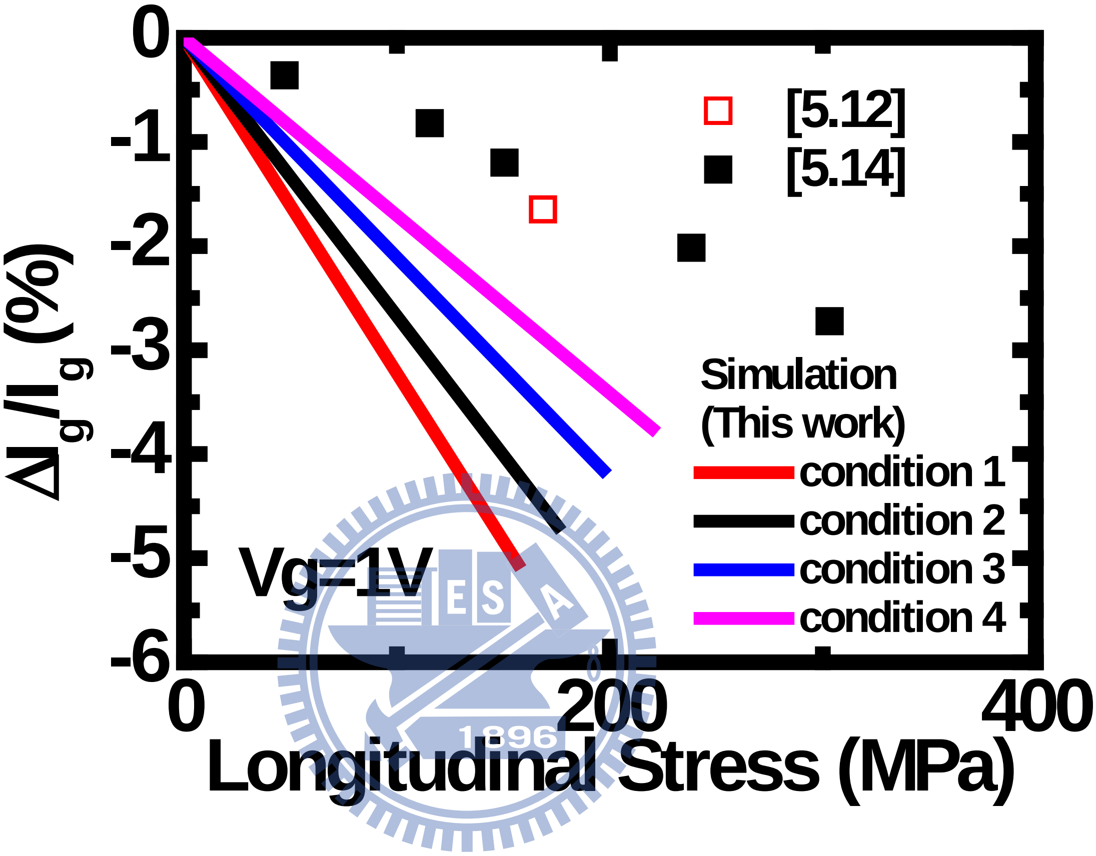

Fig. 5.4 Comparison of gate current change data (symbols) [5.12], [5.14] at Vg = 1 V with those (lines) simulated under four different conditions in Fig. 5.1, plotted versus <110> tensile stress magnitude. The gate oxide thickness and substrate doping concentration used in simulation are 1.3 nm and 5×10^{17} cm^{-3}, as in [5.12].

Chapter 6

3-D Mobility Calculation

6.1 Mobility for Other Surface Orientations

6.1.1 Mobility in (110)/<1-10> and (111)/<1-10> MOSFETs

3-D structure with multi-gates and different surface orientations has been increasing important [6.1]. Fig. 6.1, for example, shows such a structure in terms of FinFET on (001) substrate. The inversion layer carriers not only exist under the top surface, but also near the side wall surface. Although all of them have the same transport direction <1-10>, quantum confinements occur along the different directions: (001) for top surface and (110) for side wall surface. Thus, the total mobility can be seen as the average contribution of those carriers under different orientated surfaces. For that reason, our work is extended from (001) to other orientations.

With the simulation tool, *NEP*, we can calculate the electrical properties of (110) and (111) nMOSFET, as described in Chapter 4. But the effective mass should be different from (001) case. The corresponding nominal values are listed in Table 6.1 [6.2], [6.3]. Generally, the six energy valleys are degenerate under <111> confinement. However, as channel is designed along <1-10>, those six valleys are sorted to $\Delta 2$ and $\Delta 4$ according to their conductivity effective mass. The calculated results are again compared with *Schred* [6.4] as shown in Fig. 6.2 for (111) nMOSFET. In (111) case, the subband levels of 2-fold and 4-fold are the same because their quantization effective masses are equivalent. With these results as inputs, simulated mobility versus effective field is presented in Fig. 6.3. η is equal to 0.5 in using Eq. (4.13b). The same parameters in Table 4.1 are used here except Δ=0.2nm for (111). Fig. 6.3 also shows the experimental data for comparison [6.5].

6.1.2 Stress Applied along Arbitrary Directions

With the aid of *NEP*, we can do more simulation work in any case. In Chapter 5, we discussed the mobility enhancement only in (001) nMOSFET under <110> tensile stress. In reality, stress comes from muilt-directions. Thus, the work in Chapter 5 is quite inadequate. In Table 3.1, we have already discussed some directions along which the stress is applied. Thus, we consider four strain conditions for each orientation: longitudinal, transverse, vertical, and biaxial. The calculation result is show in Fig. 6.4. We let all of π_m equal to zero at this time. In Fig. 5.2 and 5.3, a little difference between the mobility enhancement with and without piezo-effective-mass coefficients is observed. That is the reason the π_m could be neglected here. For (001)/<110> case, the mobility ratios under longitudinal stress and transverse one are the same because of the symmetry of both the directions [6.6]. In the same way, the mobility ratios under longitudinal stress and vertical one are the same for (110)/<1-10> case. Fig. 6.4(a) and (b) also show the simulated result as in [6.7]. We can observe a large ratio when vertical stress is applied on (001)/<110> nMOSFET or the transverse stress is applied on (110)/<1-10> nMOSFET. The applied stress of both cases is coincident along the same direction <100>. From Table 3.1 and Eq. (3.11), we know that the stress along <100> changes subband separation significantly. The mobility changes due to two factors: (a) the charge re-occupation, and (b) the interaction between each subband which is dependent on subband separation. As can be observed in Fig. 6.4, the first factor is stronger factor than another; otherwise, the mobility ratio in both tensile and compressive stress should be positive for (111) case. In the same way, the mobility ratio saturation occurs in Fig. 6.4(a) and (b) because the charge almost centralizes on one subband. In Table 6.2, the occupation ratio on the lowest Δ_2 and Δ_4 subband in (001) nMOSFET under vertical stress are listed. That can explain why the mobility ratio is to saturate over ±1.5GPa.

6.2 *NEP* for Double-Gate MOSFET

It is well known that the scaling of the traditional bulk MOSFETs would encounter several challenging issues like suppressing the short channel effects (SCE). In order to face these challenges, increasing channel doping is one of the methods as has been adopted in conventional planar devices. But high channel doping would induce poor carrier mobility [6.8]. To overcome the problem, new device architectures, such as multiple gate structures have been proposed. Thus, it is needed to improve *NEP* to incorporate a double-gate structure. The double-gate structure is a thin Si body sandwiched between two oxide layers, with a metal or polysilicon film formed on each oxide. So, the control of the gates on the channel in a double-gate structure is stronger than in a traditional bulk MOSFET as the gate voltage is applied to front and back gates. In this work, we develop a simulator *DG-NEP* to investigate physical properties of double-gate structure.

6.2.1 *DG-NEP* Simulator

DG-NEP considers a symmetric structure, as shown in Fig. 6.5, where t_{si} is the film thickness, E_{fp} and E_{fm} are the Fermi energy levels of p-substrate and metal respectively, and ϕ_m is the work function of metal. To solve the electrical property of the device, *DG-NEP* basically uses the same procedure as *NEP*, which has been described in Chapter 4. However, it has been well recognized that quantum mechanical (QM) effects become more important in determining the properties of such small devices. In Chapter 4, the boundary conditions of Schrödinger’s equation are often making the wave-function go to zero at the silicon/gate-oxide interface. That is to say, an infinite potential barrier height at silicon/gate-oxide interface is assumed. Nevertheless, the actual barrier height is finite and is equal to a few electron-volts. Therefore, wave-function actually can penetrate into the gate oxide. To deal with this issue, some changes are needed to do to make a double-gate version of *NEP*: *DG-NEP*. In *NEP*, only the potential of substrate region is calculated, as shown in Fig. 4.1, while the potential of the whole region including oxide is needed to calculate now in *DG-NEP*. Therefore, the permittivity and the effective mass of oxide should be considered while Schrödinger and Poisson's equation. To realize the wave-function penetration, Eq. (4.2) is rewritten as:

$$-\frac{\hbar^2}{2}\nabla\left[\frac{1}{m(z)}\nabla\psi(z)\right]+qV(z)\psi(z)=E\psi(z) \tag{6.1}$$

The simulated results for different substrate thicknesses are shown in Fig. 6.6 and 6.7. In this work, the effective mass in oxide is $0.5m_0$ [6.9], [6.10] and the barrier height is 3.15eV at 300K. It is found that that our DG-NEP simulations without penetration effect match Schred's [6.4] ones. This validates our double-gate structure without considering wave-function penetration. The subband energies with wave-function penetration are lower than without penetration. Besides, for device with thick t_{Si}, each subband can find another one with the same energy level. It is due to the upper and lower inversion layers sufficiently separated as two bulk inversion layers stand back to back. In this situation, each subband is confined by the potential drop of Si film. As t_{Si} decreases, the barrier between two inversion regions becomes lower making the subband energies emerge and split [6.11]. In this case, subband is confined by the space well of oxide. These phenomena can be seen in Fig. 6.8 and 6.9. In Fig. 6.9, we can observe that the subbands with the same energy level become different gradually as t_{Si} decreases. Furthermore, the stress effect is embedded successfully in *DG-NEP*, as shown in Fig. 6.10.

6.2.2 Surface-Roughness-Limited Mobility

The mobility model of double-gate MOSFET is basically equivalent to planar one as described in Chapter 4. However, the double-gate structure has one more SiO_2/Si interface. Therefore, we need to consider the surface roughness scattering affected by both interfaces. In the usual model for surface roughness scattering, an assumption was made that the surface potential could be expanded to first order [6.13], [6.14]:

$$\mathrm{V}(\mathrm{z}+\Delta) \cong \mathrm{V}(\mathrm{z})+\Delta \frac{\partial V(z)}{\partial z} \tag{6.2}$$

where V(z) is the nonperturbed surface potential and Δ the roughness measured from the oxide/silicon interface. The perturbation Hamiltonian is given by:

$$H_{sr}(z)=-\frac{[V(z+\Delta)-V(z)]}{\Delta} \tag{6.3}$$

Combing Eq. (6.3) and Eq. (6.2), the perturbation Hamiltonian can be approximated by:

$$H_{sr}(z) = -\frac{\partial V(z)}{\partial z} = E(z) \tag{6.4}$$

which is used in Eq. (4.23). However, Eq. (6.4) does not work in the device with thin film. In Fig. 6.11, we compare the perturbation Hamiltonian using Eq. (6.3) and (6.4) for 5nm film. The inset of the figure is the surface potential before and after perturbation. As can be observed, significant difference between these two models is evident. In summary, the model of surface roughness scattering in double-gate MOSFET should consider the perturbation comes from both sides, in a sense the approximation used in Eq. (6.4) is over-simplified.

6.2.3 Simulating Results

In Fig. 6.12, the *DG-NEP* simulated mobility ratio (dots) due to stress is shown. The simulation condition is the same as Fig. 6.4. One thing we want to stress is that E_{eff} here is not calculated by Eq. (4.13b) but by

$$E_{eff} = \frac{\int_0^{\frac{t_{Si}}{2}} n(z)E(z)dz}{\int_0^{\frac{t_{Si}}{2}} n(z)dz} \tag{6.5}$$

Fig. 6.13, again, compares the calculation from Eq. (4.13b) and (6.5). Comparing the result in Fig. 6.4 and Fig. 6.12, the mobility ratio is large in double-gate MOSFET than planar one. Besides, the position where the mobility ratio begins to saturate is almost the same. Therefore, the charge redistribution also is the major factor to determine the mobility enhancement. In Table 6.3, to make comparison with planar

MOSFET, the occupation ratio on the lowest Δ_2 and Δ_4 subband in (001) dougle-gate MOSFET under vertical stress are listed. The subband level is not only confined by the potential drop but also space wall of two dielectrics in double-gate structure. Thus, the subband separation is smaller and the charges occupy more at high subbands. That gives rise to different explanations of mobility ratio in double-gate MOSFET.

6.3 Conclusion

The mobility in (001), (110), and (111) nMOSFET is successfully simulated. With this ability, the stress-induced mobility enhancement can be estimated. The change of the mobility is strongly dependent on the charge redistribution. Although the mobility of (110) MOSFET is smaller than (001)'s, the mobility enhancement of (110) MOSFET is higher than (001)'s. However, the merit for (110) MOSFET is valid only for the device is applied stress >1.5GPa or <-1.5GPa. This result may provide a path for the device designer. Moreover, the most efficient way to boost mobility is to apply stress along <100> direction.

The stress engineering is more important in double-gate MOSFET, because the mobility enhancement in double-gate MOSFET is more noticeable than planar one. It is due to the space confinement occurs in double-gate structure. The charge redistribution prevails in strained double-gate MOSFET.

References

[6.1] S. H. Tang, L. Chang, N. Lindert, Y. K. Choi, W. C. Lee, X. Huang, V. Subramanian, J. Bokor, T. J. King, and C. Hu, “FinFET-a quasi-planar double-gate MOSFET,” *IEEE Trans. Electron Device*, vol. 48, no. 5, pp. 880-886, May 2001.

[6.2] F. Stern, “Self-consistent results for n-type Si inversion layers,” *Phys. Rev. B*, vol. 5, no.12, pp.4891-4899, Jun. 1972.

[6.3] A. Rahman, M S. Lundstrom, and A. W. Ghosh, “Generalized effective-mass approach for n-type metal-oxide-semiconductor field-effect transistors on arbritrarily oriented wafers,” *J. Appl. Phys.*, vol. 97, no. 5, pp. 053702-1-053702-12, Feb. 2005.

[6.4] Schred. [Online]. Available: http://nanohub.org/resources/schred.

[6.5] S. Takagi, A. Toriumi, M. Iwase, and H. Tango, “On the universality of inversion layer mobility in Si MOSFET’s: Part II – Effects of surface orientation,” *IEEE Trans. Electron Devices*, vol. 41, no. 12, pp. 2363-2368, Dec. 1994.

[6.6] K. Uchida, T. Krishnamohan, K. C. Saraswat, and Y. Nishi, “Physical mechanisms of electron mobility enhancement in uniaxial stressed MOSFETs and impact of uniaxial stress engineering in ballistic regime,” in *IEDM Tech. Dig.*, 2005, pp. 129–132.

[6.7] P. Packan, S. Cea, H Deshoande, T. Ghani, M. Giles, O. Golonzka, M. Hattendorf, R. Kotlyar, K. Kuhn, A. Murthy, P. Ranade, L. Shifren, C. Weber, and K. Zawadzki, “High performance Hi-K + metal gate strain enhanced transostors on (110) silicon,” in *IEDM Tech. Dig.*, 2008, pp. 1–4.

[6.8]A. DasGupta, “Multiple gate MOSFETs: The road to future,” in *Proceedings of the 2007 International Workshop on the Physics of Semiconductor Devices*

(IWPSD), pp. 96-101, Sep. 2007.

[6.9] Z. A. Weinberg, “On tunneling in metal-oxide-silicon structures,” *J. Appl. Phys.*, vol. 53, no. 7, pp. 5052–5056, Jul. 1982.

[6.10] W. H. Lee and M. J. Chen, “Gate direct tunneling current in uniaxially compressive strained nMOSFETs: a sensitive measure of electron piezo effective mass,” *IEEE Trans. Electron Devices*, vol. 58, no. 1, pp. 39-45, Jan. 2011.

[6.11] M. Shoji and S. Horiguchi, “Electronic structures and phonon limited electron mobility of double-gate silicon-on-insulator Si inversion layers,” *J. Appl. Phys.*, vol. 85, no. 5, pp. 2722–2731, Mar. 1999.

[6.12] N. Barin, C. Fiegna, and E. Sangiorgi, “Analysis of strained silicon on insulator double gate MOS structures,” *2004 Eur. Solid-State Device Research Conf.*, pp. 169-172, 2004.

[6.13] S. Yamakawa, H. Ueno, K. Taniguchi, C. Hamaguchi, K. Miyatsuji, K. Masaki, and U. Ravaioli, “Study of interface roughness dependence of electron mobility in Si inversion layers using the Monte Carlo method,” *J. Appl. Phys.*, vol. 79, no. 2, pp. 911–916, Jan. 1996.

[6.14] F. Gámiz, J. B. Roldán, J. A. López-Villanueva, P. Cartujo-Cassinello, and J. E. Carceller, “Surface roughness at Si-SiO$_2$ interfaces in fully depleted silicon-on-insulator inversion layers,’ *J. Appl. Phys.*, vol. 86, no. 12, pp. 6854-6863, Dec. 1999.

Table 6.1 The nominal values of the electron effective masses in silicon as electron is confined along three different directions.

Effective mass (m_0)	**(001)/<110>**		**(110)/<1-10>**		**(111)/(1-10)**	
Degeneracy	**2**	**4**	**2**	**4**	**2**	**4**
Longitudinal	**0.19**	**0.315**	**0.19**	**0.283**	**0.19**	**0.553**
Transverse	**0.19**	**0.552**	**0.916**	**0.37**	**0.675**	**0.232**
Quantized	**0.916**	**0.19**	**0.19**	**0.315**	**0.258**	**0.258**
Density-of-state	**0.19**	**0.417**	**0.417**	**0.324**	**0.358**	**0.358**

Table 6.2 The occupation ratio of the lowest Δ_2 and Δ_4 subband in (001) nMOSFET under vertical stress. All results are simulated at E_{eff} = 1MV/cm and $N_{sub}=10^{17}\text{cm}^{-3}$.

Occupation (%)	**σ –3GPa**	**σ –1.5GPa**	**σ 0**	**σ 1.5GPa**	**σ 3GPa**
Δ_2	**85**	**85**	**70**	**13**	**~0**
Δ_4	**~0**	**~0**	**23**	**85**	**98**

Table 6.3 The occupation ratio of the lowest Δ_2 and Δ_4 subband in (001) double-gate MOSFET under vertical stress. All results are simulated at E_{eff} = 1MV/cm and $N_{sub}=10^{17}\text{cm}^{-3}$.

Occupation (%)	**σ −3GPa**	**σ −1.5GPa**	**σ 0**	**σ 1.5GPa**	**σ 3GPa**
Δ_2	**52**	**52**	**39**	**4**	**~0**
Δ_4	**~0**	**~0**	**29**	**93**	**99**

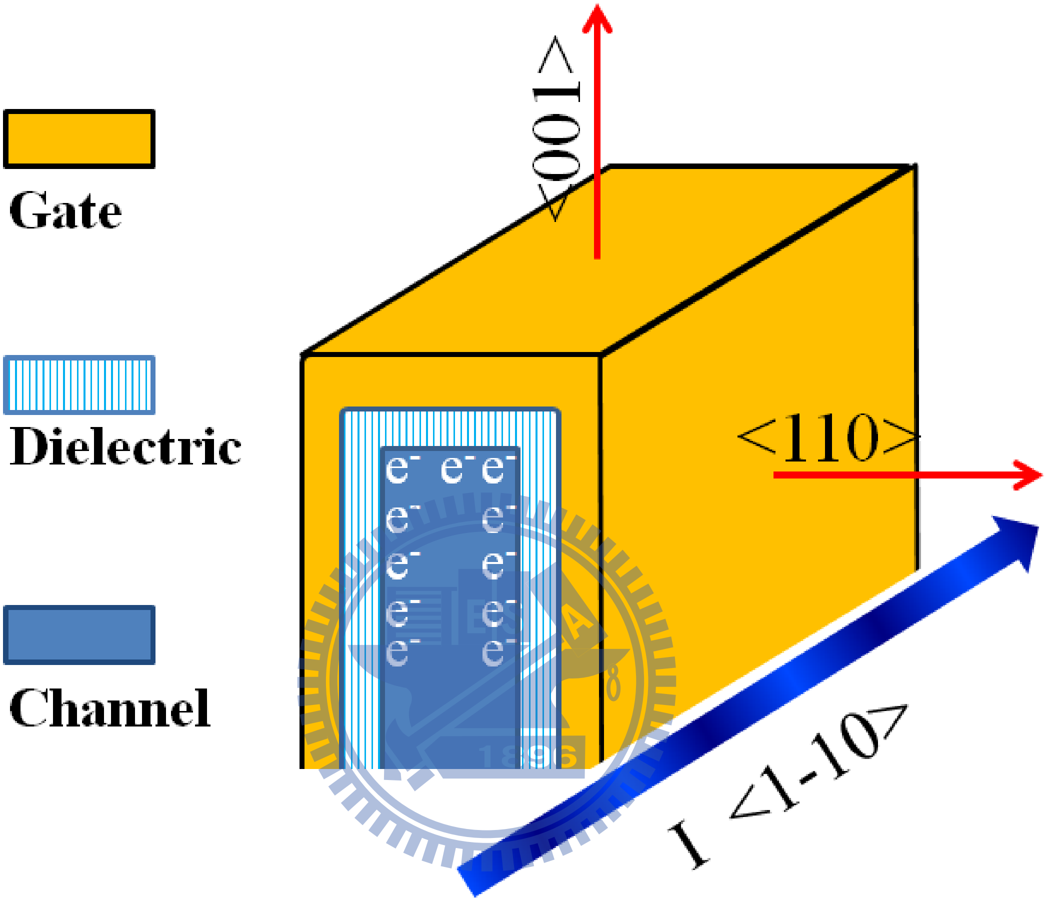

Fig. 6.1 The schematic of the triple-gate FinFET with the different crystal orientations.

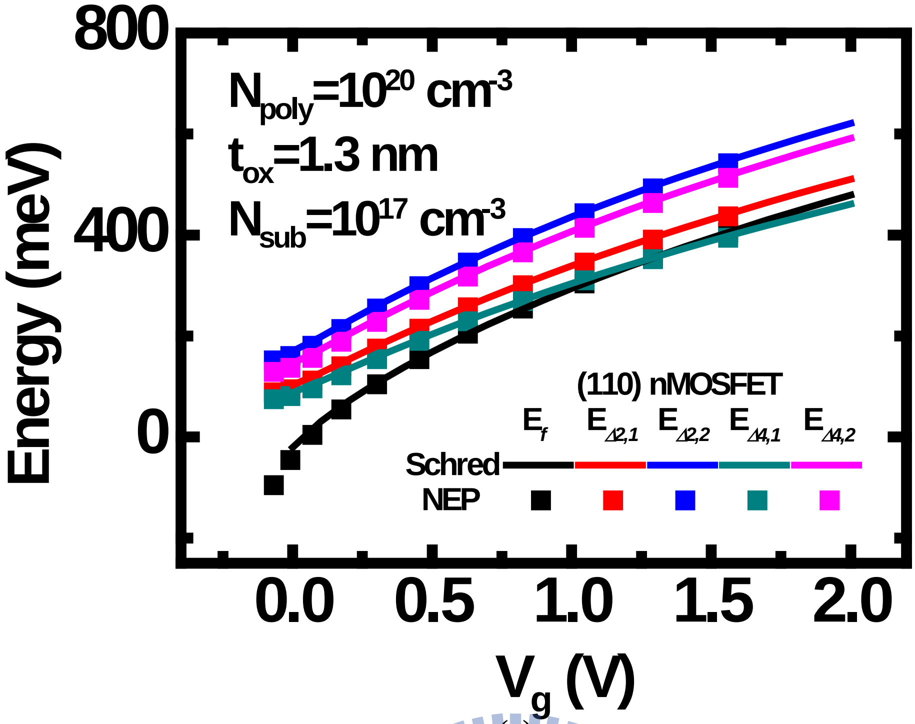

(a)

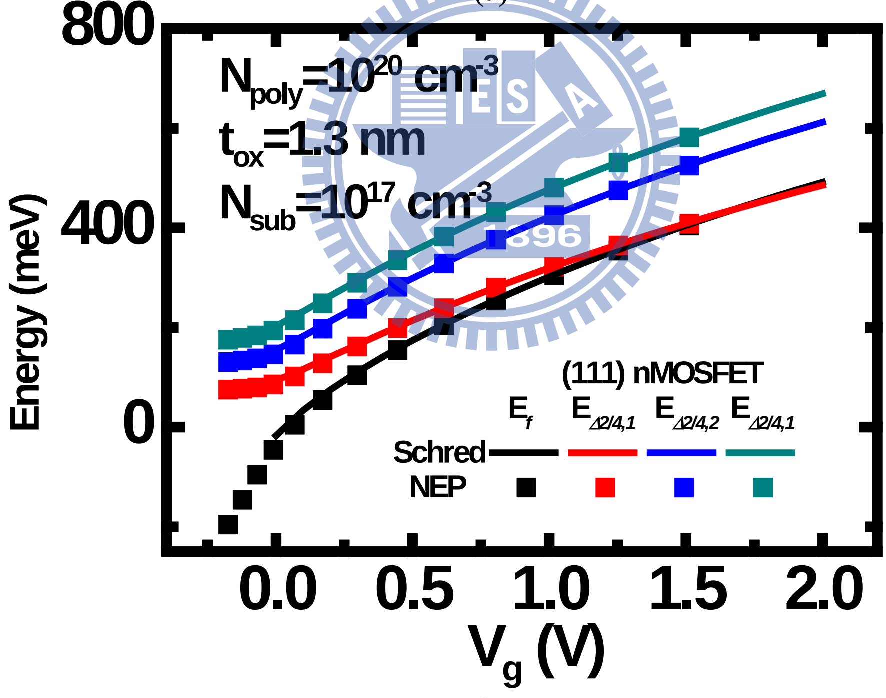

(b)

Fig. 6.2 Subband levels calculated by the *Schred* [6.4] (lines) and by *NEP* (dots) for two cases: (a) (110) nMOSFET; and (b) (111) nMOSFET. Both of them are with the same process parameters.

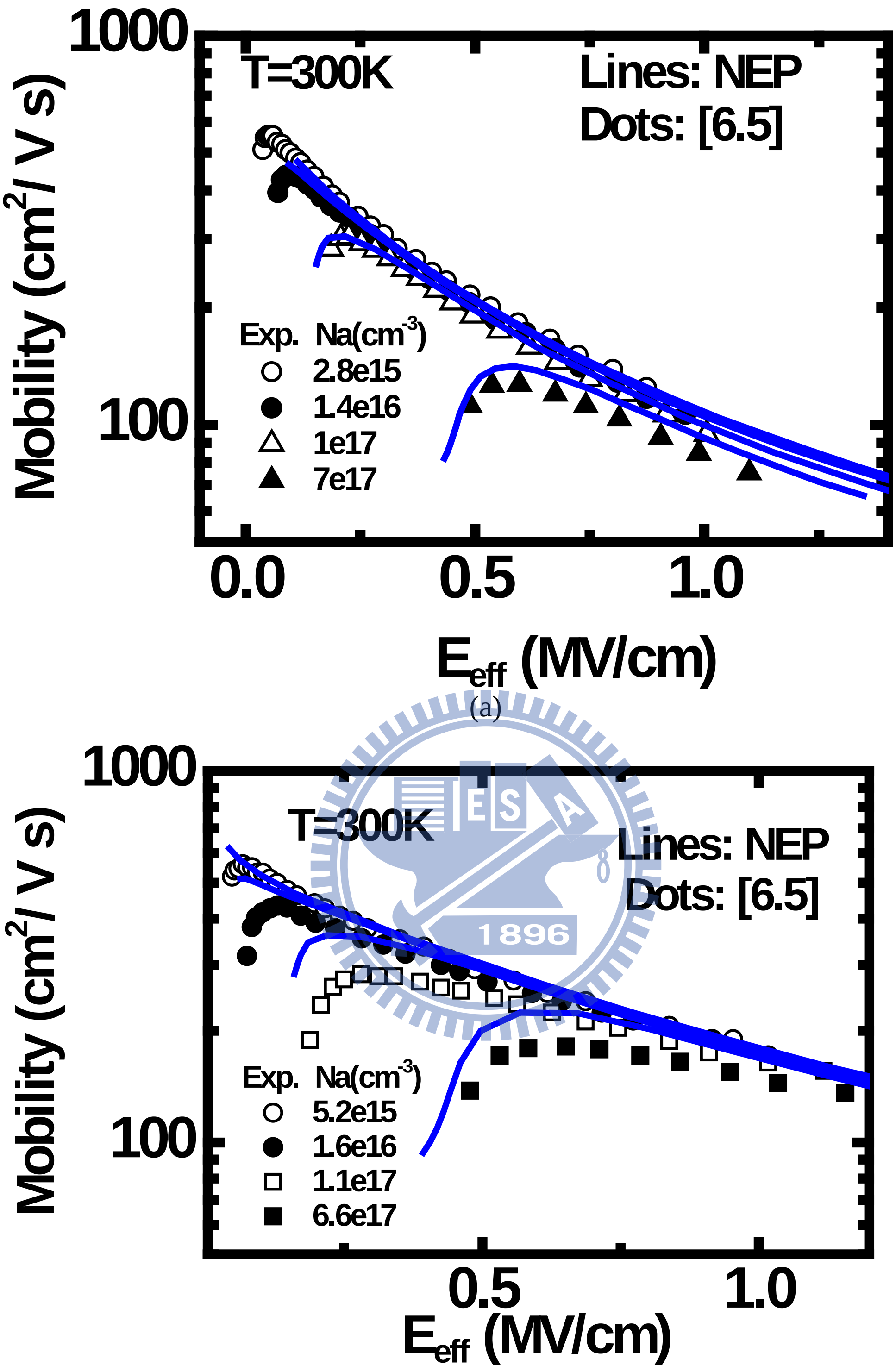

(a)

(b)

Fig. 6.3 Repeating the same work as in Fig. 4.5 on (110) and (111) nMOSFET. The parameters we used are listed in Table 4.1 except Δ = 0.2nm is used in (111) case.

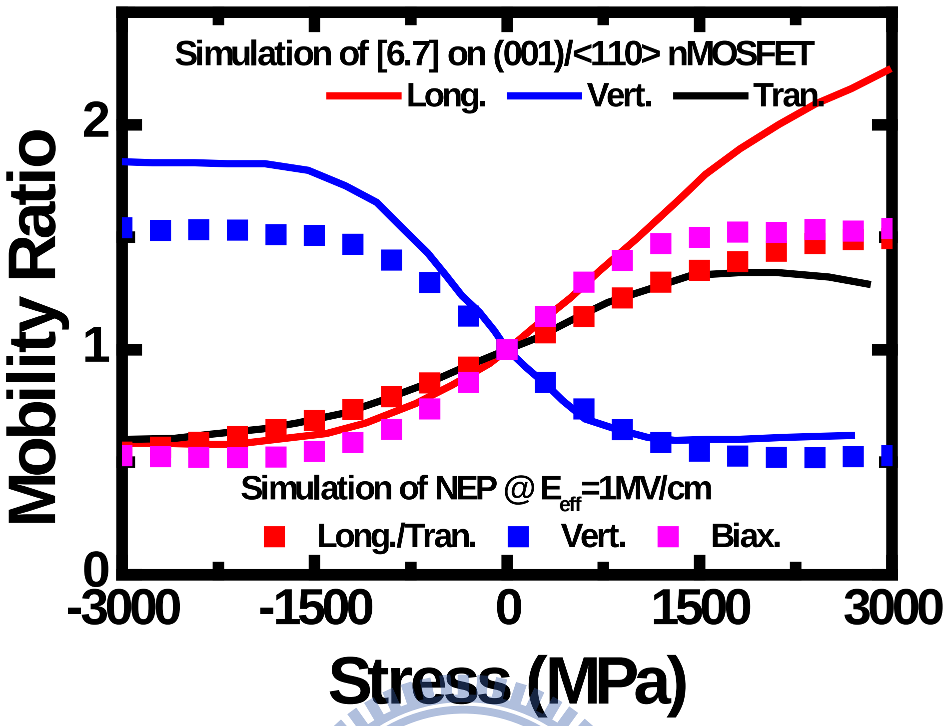
Simulation of [6.7] on (001)/<110> nMOSFET
Long.
Vert.
Tran.
Simulation of NEP @ E_{eff}=1MV/cm
Long./Tran.
Vert.
Biax.
Mobility Ratio
0
1
2
-3000
-1500
0
1500
3000
Stress (MPa)

(a)

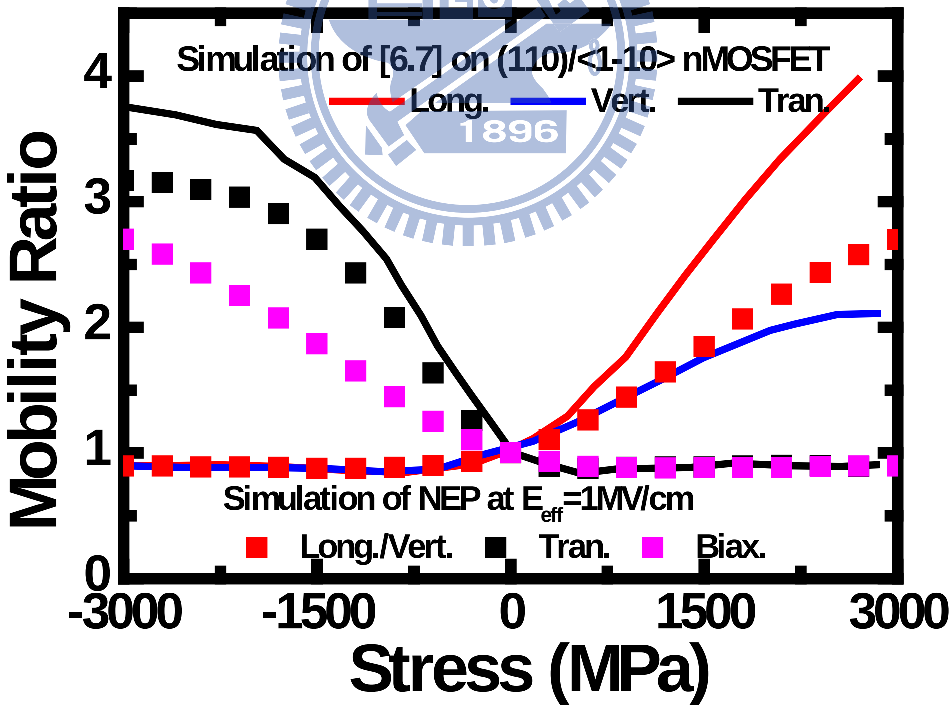
Simulation of [6.7] on (110)/<1-10> nMOSFET
Long.
Vert.
Tran.
Simulation of NEP at E_{eff}=1MV/cm
Long./Vert.
Tran.
Biax.
Mobility Ratio
0
1
2
3
4
-3000
-1500
0
1500
3000
Stress (MPa)

(b)

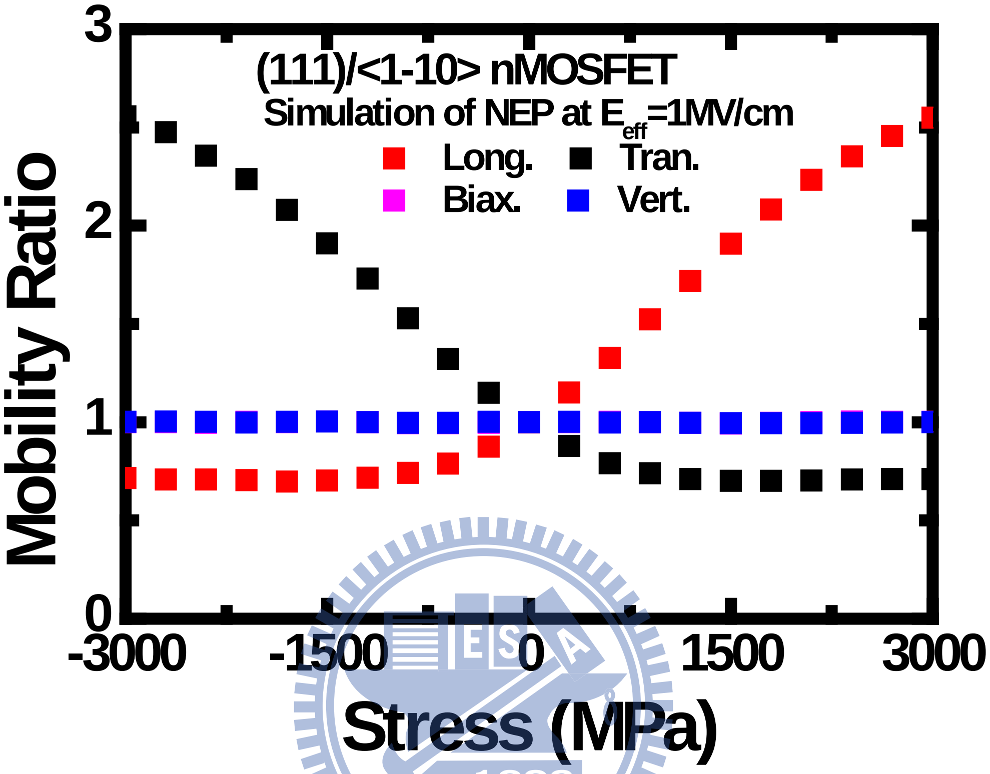

(c)

Fig. 6.4 The *NEP* simulated mobility ratio (dots) due to stress. Three orientations are involved: (a) (001)/<110>, (b) (110)/<1-10>, and (c) (111)/<1-10>. Longitudinal, transverse, vertical, and biaxial stresses are considered for each orientation. All are simulated with N_{sub} = 10^{17}cm^{-3} and E_{eff} = 1MV/cm. In (a) and (b), the simulated work by [6.7] is together shown for comparison.

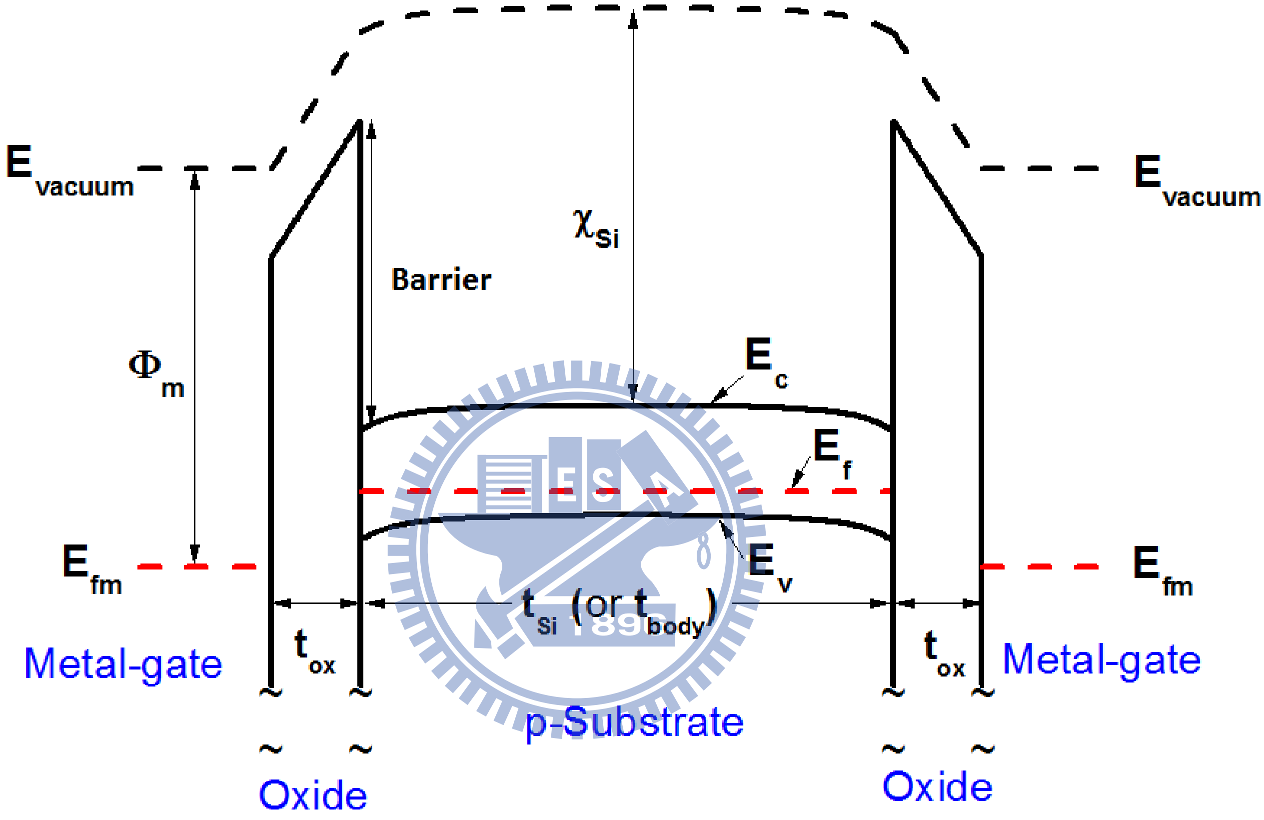

Fig. 6.5 The energy band diagram in a double-gate nMOSFET.

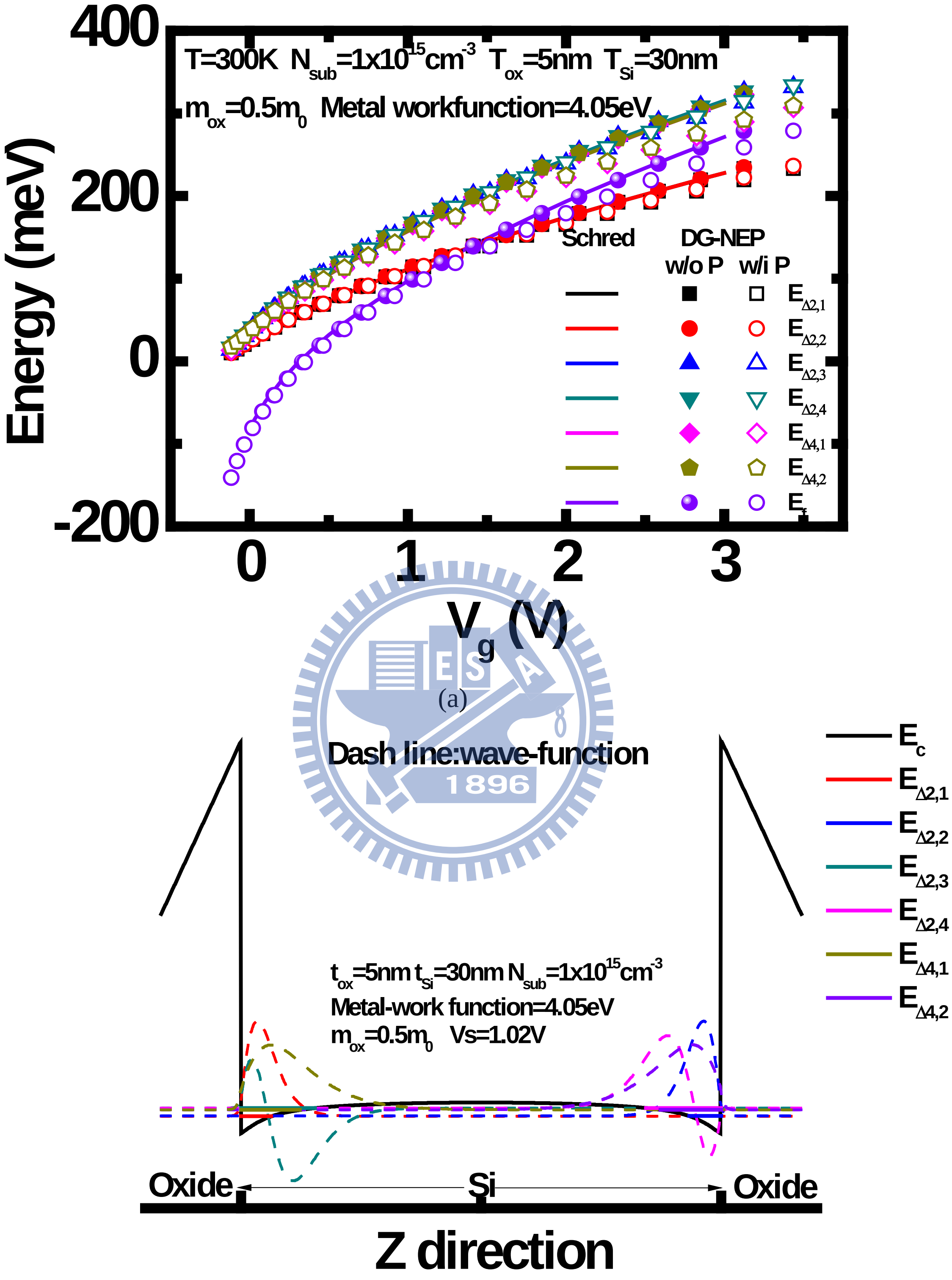

(a)

(b)

Fig. 6.6 (a) Subband energy versus gate voltage and (b) the respective wave-function of double-gate MOSFET with N_{sub}=1x10^{16}cm^{-3}, t_{si}=30nm, and t_{ox}=5nm.

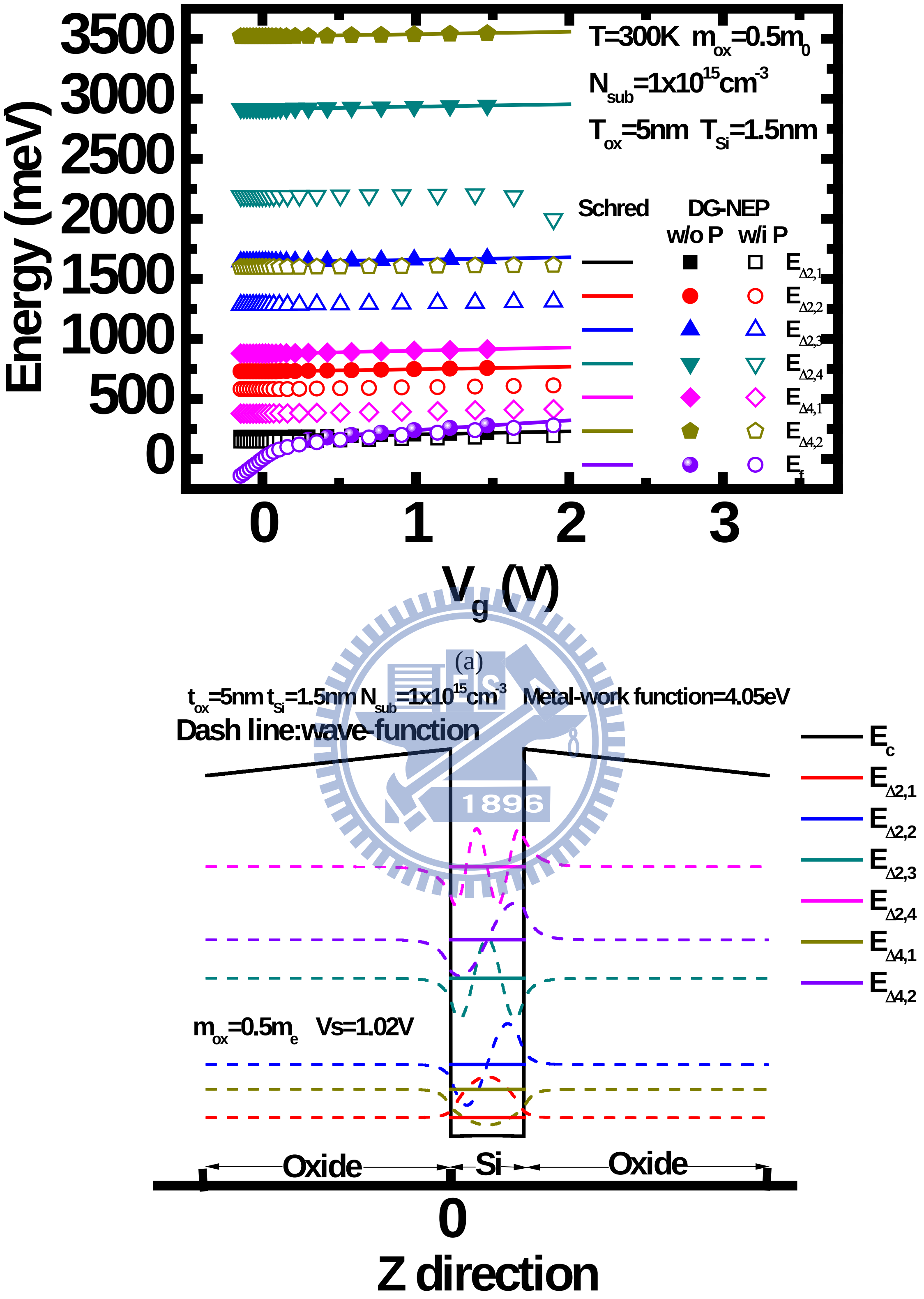

(a)

(b)

Fig. 6.7 (a) Subband energy versus gate voltage and (b) the respective wave-function of double-gate MOSFET with N_{sub}=1x10^{16}cm^{-3}, t_{si}=1.5nm, and t_{ox}=5nm.

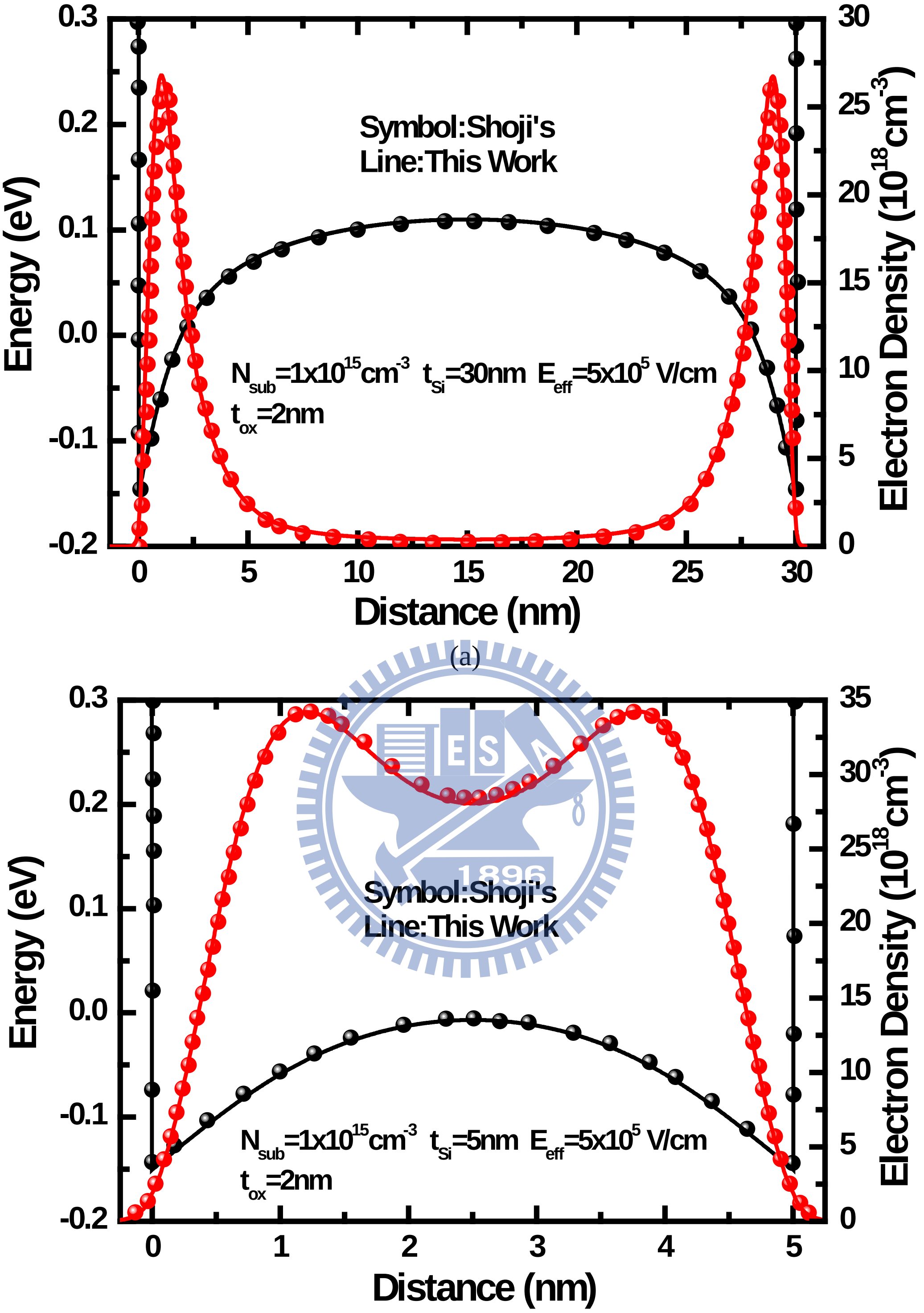

(a)

(b)

Fig. 6.8 The comparison of potentials and electron density distributions structure at $E_{eff} = 5\times10^5$ V/cm in (a) t_{Si}=30nm and (b) t_{Si}=5nm with Shoji's data [6.11].

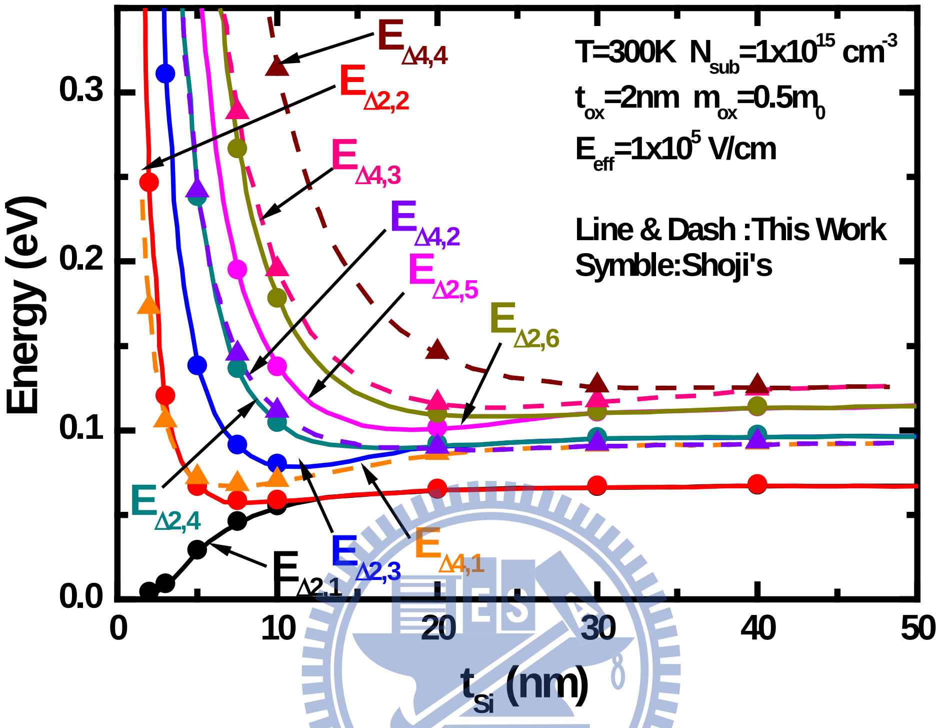

Fig. 6.9 Subband energies as function of Si thickness t_{Si} at $E_{eff} = 1\times10^5\ V/cm$ and the comparison with Shoji's data [6.11].

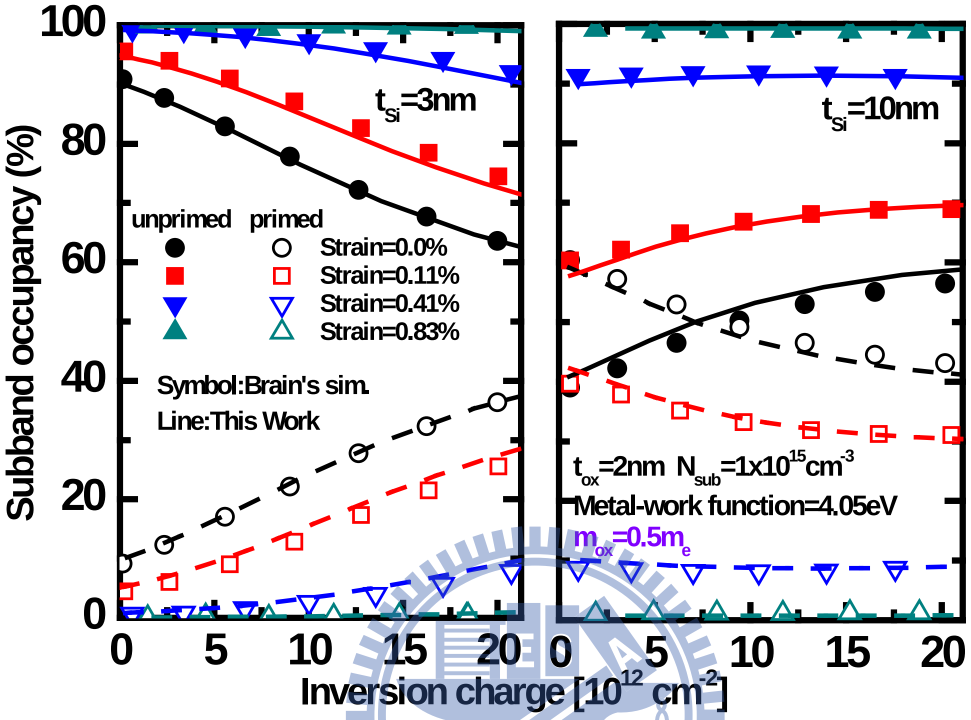

Fig 6.10 Subband occupancy versus inversion charge for different Si strain. Symbols: Brain's results [6.12]; Lines: this work. The effective mass $m^* = 0.5m_0$ is used in S_iO_2 regions, and biaxial tensile strain 1%=1.8GPa [6.6].

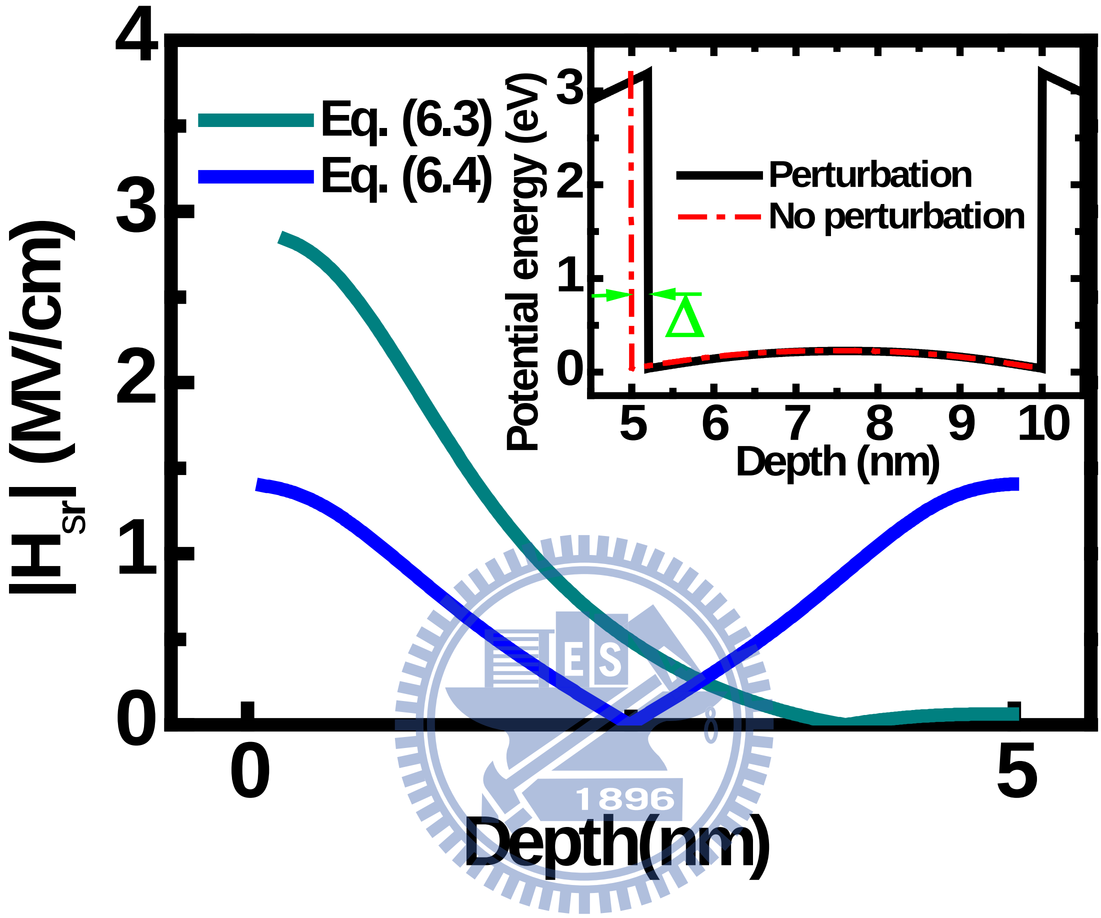

Fig. 6.11 The 0.2nm perturbation of surface roughness assumed in 5nm-film double-gate structure. The Hamiltonians of the perturbation is calculated using (6.3) and (6.4). Significant difference between these two models can be observed.

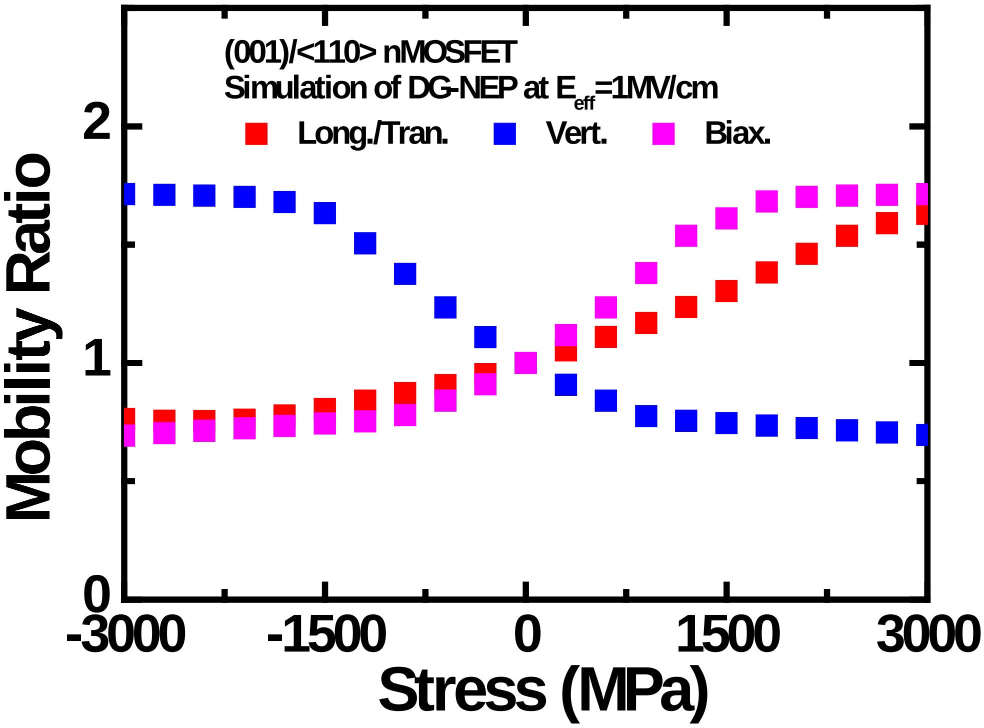
(001)/<110> nMOSFET
Simulation of DG-NEP at E_{eff}=1MV/cm
🟥 Long./Tran.
🟦 Vert.
■ Biax.
Mobility Ratio
0
1
2
-3000
-1500
0
1500
3000
Stress (MPa)

(a)

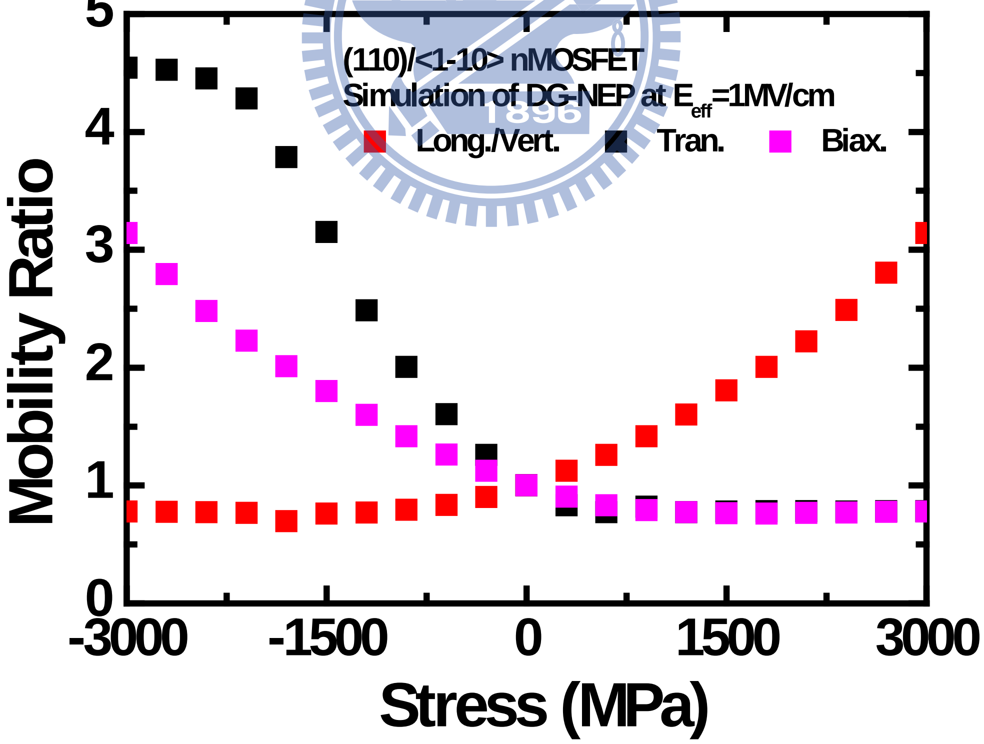
(110)/<1-10> nMOSFET
Simulation of DG-NEP at E_{eff}=1MV/cm
🟥 Long./Vert.
■ Tran.
■ Biax.
Mobility Ratio
0
1
2
3
4
5
-3000
-1500
0
1500
3000
Stress (MPa)

(b)

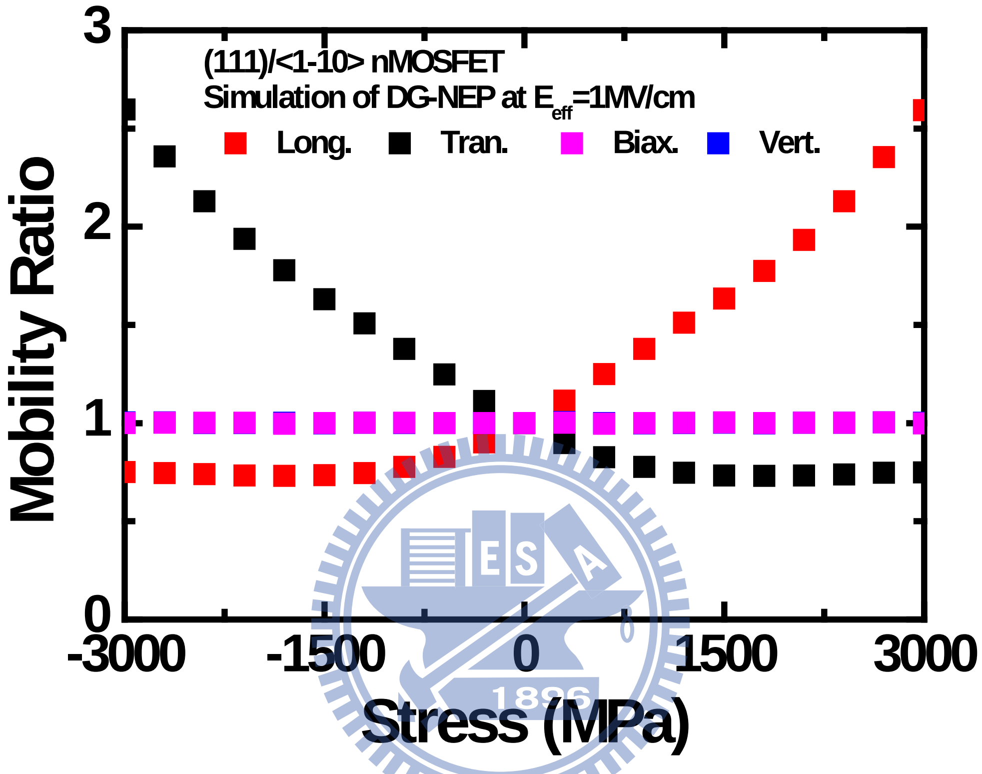

(c)

Fig. 6.12 The *DG-NEP* simulated mobility ratio (dots) due to stress. Three orientations nMOSFET are involved: (a) (001)/<110>, (b) (110)/<1-10>, and (c) (111)/<1-10>. Longitudinal, transverse, vertical, and biaxial stresses are considered for each orientation. All are simulated with N_{sub} = 10^{17}cm^{-3} and E_{eff} = 1MV/cm.

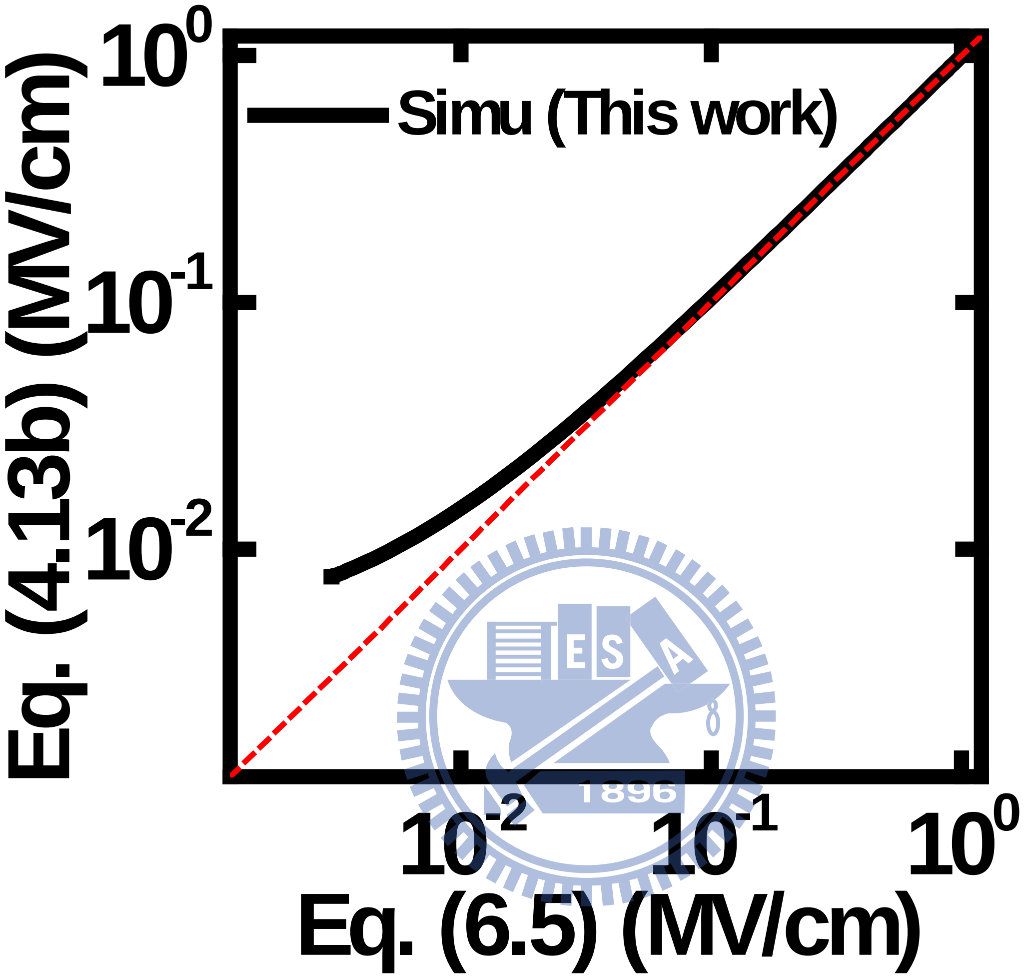

Fig. 6.13 Comparison of calculated electric field (solid line) between Eq. (4.13b) and (6.5) using *DG-NEP*. The dashed line is the line with a slope of 1 and through the origin.

Chapter 7

Conclusions and Suggestions for Future Work

7.1 Conclusions

In Chapter 2, we have proposed a new correction-coefficient η, that has been incorporated into original *TRP*. This improvement can ensure the validity of *TRP* in (001) nMOSFET case. The same procedure can be conducted for (110) and (111) cases. In Chapter 3, we have introduced the definition of stress and strain. The matrix form connecting strain to stress has also been presented. Thus, the energy level shift of each valley can be estimated through the deformation potential. Combining the TRP and strain effect, the strain-induced gate direct tunneling current has been analyzed. Reasonable reproduction of measured gate direct tunneling current has been achieved, leading to the underlying electron piezo-effective-mass coefficients. From the experimental date under external stress and process-induced stress [7.1], [7.2], the silicon dioxide growth rate retarded under the compressive stress has been proved [7.3].

In Chapter 4, a new simulator named *NEP* has been developed for n-channel MOSFETs. The corresponding fully Schrődinger and Poisson equation solver has been successfully established. With the outcomes of the wave-function and subband energy, the total mobility due to phonon scattering, surface roughness scattering, and impurity scattering, has been calculated. In Chapter 5, the piezo-effective-mass coefficients have been extracted from experimental mobility data [7.4]. In these methods, the role of the 4-fold valley Δ_4 out-of-plane π_m has been overlooked. We have provided extra evidence for the existence of the fourfold out-of-plane piezo-effective-mass coefficient. In Chapter 6, we have extended our work to other surface orientations. *NEP* for (110) and (111) nMOSFET has straightly been built. The mobility and its stress-induced mobility for each oriented substrate can be estimated and compared with those in the literatures [7.5], [7.6].

To deal with the 3-D structure, *NEP* has been modified. The resulting double-gate version has successfully predicted 3-D stress depend of mobility, as well as the effect of decreasing the film thickness.

7.2 Future Work

The down scaling of the traditional bulk MOSFETs would encounter several challenging issues. In order to face these issues like short channel effects and mobility degradation, the stress and material aspects should be involved. To keep pace with the technologic generation afterwards, some suggestions are proposed here.

First, the band warp due to stress along <110> on (001) nMOSFET, as quantified by π_m, has been extracted in this work. To confirm this, a systematic experimental task on the mobility and gate direct tunneling under strain applied along the multiples directions are required. It should be more convenient that the advance full-band calculation techniques such as pseudopotential [7.7] and k•p [7.8] methods are supported.

Second, the WKB approximation is used to calculate the tunneling probability of direct tunneling current. However, this approximation is derived under some simplifying assumptions [7.9]: the barrier is very high and/or wide and the effective mass is the same through the gate dielectric. It seems to be inadequate for the next-generation of device whose dielectric is only few nanometers thick. Thus, advance technology like the first-principle calls one of relevance.

Third, to overcome the mobility degradation in the scaling dielectric, the III-V compound and Ge are popular candidates for the channel material due to high mobility. Even the graphite material has been expected recently. Lots of works dedicated to the manufacturing processes of these novel materials [7.10]-[7.12] and the corresponding band calculations has been published [7.13]. A further study on modified *NEP* to be adapted to accommodate of these next-generation materials is needed.

Finally, owing to the mobility degradation in highly scaled devices, additional scattering mechanisms exist. Those extra scatterings can be generalized in terms of Coulomb scattering due to halo implant and the defects near S/D, remote surface roughness, fixed oxide charge, and remote phonons [7.14]-[7.16]. The corresponding physical models should be established and incorporated into *NEP*.

References

[7.1] J. S. Lim, X. Yang, T. Nishida, and S. E. Thompson, “Measurement of conduction band deformation potential constants using gate direct tunneling current in *n*-type metal oxide semiconductor field effect transistors under mechanical stress,” *Appl. Phys. Lett.*, vol. 89, no. 7, pp. 073509-1-073509-3, Aug. 2006.

[7.2] C. Y. Hsieh and M. J. Chen, “Measurement of channel stress using gate direct tunneling current in uniaxially stressed nMOSFETs,” *IEEE Electron Device Lett.*, vol. 28, no. 9, pp. 818-820, Sep. 2007.

[7.3] W. H. Lee and M. J. Chen, “Gate direct tunneling current in uniaxially compressive strained nMOSFETs: a sensitive measure of electron piezo effective mass,” *IEEE Trans. Electron Devices*, vol. 58, no. 1, pp. 39-45, Jan. 2011.

[7.4] K. Uchida, T. Krishnamohan, K. C. Saraswat, and Y. Nishi, “Physical mechanisms of electron mobility enhancement in uniaxial stressed MOSFETs and impact of uniaxial stress engineering in ballistic regime,” in *IEDM Tech. Dig.*, 2005, pp. 129–132.

[7.5] S. Takagi, A. Toriumi, M. Iwase, and H. Tango, “On the universality of inversion layer mobility in Si MOSFET’s: Part II – Effects of surface orientation,” *IEEE Trans. Electron Devices*, vol. 41, no. 12, pp. 2363-2368, Dec. 1994.

[7.6] P. Packan, S. Cea, H Deshoande, T. Ghani, M. Giles, O. Golonzka, M. Hattendorf, R. Kotlyar, K. Kuhn, A. Murthy, P. Ranade, L. Shifren, C. Weber, and K. Zawadzki, “High performance Hi-K + metal gate strain enhanced transostors on (110) silicon,” in *IEDM Tech. Dig.*, 2008, pp. 1–4.

[7.7] J. R. Chelikowsky and M. L. Cohen, “Nonlocal pseudopotential calculations for the electronic structure of eleven diamond and zinc-blende semiconductors," *Phys. Rev. B*, vol. 14, no. 2, Jul. 1976.

[7.8] M. Cardona and F. H. Pollak, "Energy-band structure of germanium and silicon: The k•p method," *Phys. Rev.*, vol. 142, no. 2, Feb. 1966.

[7.9] D. J. Griffiths, Introduction to Quantum Mechanics, *second edition*, Upper Saddle River, NJ 07458.

[7.10] S. Datta, T. Ashley, J. Brask, L. Buckle, M. Doczy, M. Emeny, D. Hayes, K. Hilton, R. Jefferies, T. Martin, T. J. Phillips, D. Wallis, P. Wilding, and R. Chau, "85nm gate length enhancement and depletion mode InSb quantum well transistors for ultra high speed and very low power digital logic applications," in *IEDM Tech. Dig.*, 2005, pp. 763–766.

[7.11] M. K. Hudait, G. Dewey, S. Datta, J. M. Fastenau, J. Kavalieros, W. K. Liu, D. Lubyshev, R. Pillarisetty, W. Rachmady, M. Radosavljevic, T. Rakshit, and Robert Chau, "Heterogeneous integration of enhancement mode $In_{0.7}Ga_{0.3}As$ quantum well transistor on silicon substrate using thin (≦2nm) composite buffer architecture for high-speed and low-voltage (0.5V) logic applications," in *IEDM Tech. Dig.*, 2007, pp. 625–628.

[7.12] D.-H. Kim and J. A. del Alamo, "Logic performance of 40 nm InAs HEMTs," in *IEDM Tech. Dig.*, 2007, pp. 629–632.

[7.13] I. Vurgaftman, J. R. Meyer, and L. R. Ram-Mohan, "Band parameters for III-V compound semiconductors and their alloys," *J. Appl. Phys.*, vol. 89, no. 11, pp. 5815-5875, Jun. 2001.

[7.14] M. V. Fischetti, D. A. Neumayer, and E. A. Cartier, "Effective electron mobility in Si inversion layers in metal-oxide-semiconductor systems with a high-k insulator: The role of remote phonon scattering," *J. Appl. Phys.*, vol. 90, no. 9, pp. 4587-4608, Nov. 2001.

[7.15] Z. Ren, M. V. Fischetti, E. P. Gusev, E. A. Cartier, and M. Chudzik, "Inversion channel mobility in high-k high performance MOSFETs," in *IEDM Tech. Dig.*, 2003, pp. 793–796.

[7.16] M. Cassè, L. Thevenod, B. Guillaumot, L. Tosti, F. Martin, J. Mitard, O. Weber, F. Andrieu, T. Ernst, G. Reimbold, T. Billon, M. Mouis, and F. Boulanger, "Carrier transport in HfO_2/metal gate MOSFETs: Physical insight into critical parameters," *IEEE Trans. Electron Devices*, vol. 53, no. 4, pp. 759-768, Apr. 2006.

Vita

博士候選人資料

姓　　名：李韋漢　　Wei-Han Lee

性　　別：男

出生日期：中華民國 七十二年 七月 二十二日

出 生 地：台北縣

學　　歷：交通大學電子物理系

(民國九十年~民國九十四年)

交通大學電子工程研究所

(民國九十四年~民國九十五年)

交通大學電子工程研究所博士班

(民國九十五年~民國一百零一年)

論文題目：n 型反置層精準量子計算：應變、次能帶、遷移率及三維結構

Sophisticated Quantum Computation on n-type Inversion Layers: Strain, Subband, Mobility, and 3-D Structure

Publication list

[1] C. Y. Hsu, H. G. Chang, S. J. Kuang, **W. H. Lee**, Y. C. Chen, C. C. Lee, and M. J. Chen, "Enhanced hole mobility in non-(001) oriented sidewall corner of Si pMOSFETs formed on (001) substrate," *Silicon Nanoelectronics Workshop*, 2010, pp.67-68.

[2] **W. H. Lee** and M. J. Chen, "Gate direct tunneling current in uniaxially compressive strained nMOSFETs: a sensitive measure of electron piezo effective mass," *IEEE Trans. Electron Devices*, vol. 58, no. 1, pp. 39-45, Jan. 2011.

[3] M. J. Chen, S. C. Chang, S. J. Kuang, C. C. Lee, **W. H. Lee**, K. H. Cheng, and Y. H. Zhan, "Temperature-dependent remote-coulomb-limited electron mobility in n^+-polysilicon ultrathin gate oxide nMOSFETs," *IEEE Trans. Electron Devices*, vol. 58, no. 4, pp. 1038-1044, Apr. 2011.

[4] M. J. Chen and **W. H. Lee**, "Evidence for the fourfold-valley confinement electron piezo-effective-mass coefficient in inversion layers of <110> uniaxial-tensile-strained (001) nMOSFETs," *IEEE Electron Device Lett.*, vol. 33, no. 6, pp. 755-757, Jun. 2012.

[5] M. J. Chen, **W. H. Lee**, and Y. H. Huang, "Error-free Matthiessen's rule in the MOSFET universal mobility region," *IEEE Trans. Electron Devices*, under revision, 2012.